UNIVERSITY OF CALIFORNIA,
IRVINE

Synthesis and Characterization of Infrared-Absorbing Osmium-Polypyridyl Dyes for Use in Dye-Sensitized Solar Cells

DISSERTATION

submitted in partial satisfaction of the requirements
for the degree of

DOCTOR OF PHILOSOPHY

in Chemistry

by

Joseph Michael Cardon

Dissertation Committee:
Associate Professor Shane Ardo, Chair
Associate Professor Matthew D. Law
Professor Alan F. Heyduk

2019

DEDICATION

To whoever reads this,

Good luck, you are going to need it.

How to Hunt Ducks Blindfolded:

1. Attach Blindfold

2. Get Rifle

3. Go Into Wilderness

4. Fire Rifle

How to Hunt Ducks Blindfolded Better:

1. Attach Blindfold

2. Get Shotgun

3. Go into Wilderness

4. Fire Shotgun Until You Hear a “Quack!”

5. Continue Firing in that General Direction

-Joseph M. Cardon, 2019

Table of Contents

List of Symbols

π, pi, 3.14159…. (unitless)

e, Euler's Number, 2.71828… (unitless)

R, Ideal Gas Constant 8.31447 (J mol^{-1} K^{-1})

F, Faraday's Constant 96485 (C mol^{-1})

α, Nernstian Non-Ideality Factor (unitless)

T, Temperature (K)

n, Number of Electrons Passed Per Electrochemical Event (integer)

n, Number of Samples Tested (integer)

η, Solar to Electric Energy Conversion Efficiency (%)

Q, Reaction Quotient (unitless)

E, Electrochemical Potential (V vs Reference)

$E_0^{'}$ or $E^{0'}$, Formal Reduction Potential of a Species (V vs Reference)

$E_0^{'*}$, Excited State Energy Level (V vs Reference)

E^0_{cat}, Formal Reduction Potential of a Catalyst (V vs Reference)

$E_{0\text{-}0}$, Bandgap of a Material or Optical Pseudo-Bandgap of a Dye (eV)

E_{OC}, Open Circuit Potential (V vs Reference)

J_{SC}, Short Circuit Current Density (mA cm^{-2})

i, Current (mA)

i_p, Peak Current of a Cyclic Voltammogram (mA)

$i_{0,peak}$ Peak Current of Cyclic Voltammogram of a Catalyst in the Absence of Substrate (mA)

q, Total Charge Passed (C)

t, Time Passed (s)

v, Scan Rate of a Cyclic Voltammogram of Linear Sweep Voltammogram ($V\ s^{-1}$)

A, Geographic Surface Area of an Electrode (cm^2)

C, Concentration of a Generic Species (M)

$[Cat]_0$, Initial Catalyst Concentration (M)

$[Sub]_0$, Initial Substrate Concentration (M)

d, Film Thickness (μm)

$\bar{d}$, Average Film Thickness (μm)

d_{spec}, Film Thickness at Probe Beam Location (μm)

D, Diffusion Coefficient ($cm^2\ s^{-1}$)

D_{app}, Apparent Diffusion Coefficient of Self-Exchange Electron Transfer ($cm^2\ s^{-1}$)

D_{cat}, Diffusion Coefficient or Apparent Diffusion Coefficient of a Catalyst ($cm^2\ s^{-1}$)

D_{CA}, D_{app} as Measured by Chronoamperometry ($cm^2\ s^{-1}$)

D_{spec}, D_{app} as Measured by Chronoabsorptometry ($cm^2\ s^{-1}$)

D_{CV}, D_{app} as Measured by Cyclic Voltammetry ($cm^2\ s^{-1}$)

k, Second Order Electron Transfer Rate Constant ($M^{-1}\ s^{-1}$)

Abs, Absorbance (unitless)

Abs_{ox}, Absorbance of a Film with all Dyes Oxidized (unitless)

Abs_{red}, Absorbance of a Film with all Dyes Reduced (unitless)

δ, NMR Chemical Shift (ppm variance from fundamental frequency)

y, Generic Dependent Variable (any unit)

x, Generic Independent Variable (any unit)

A_1, Upper y Limit of a Boltzmann Sigmoid Curve (any unit)

A_2, Lower y Limit of a Boltzmann Sigmoid Curve (any unit)

x_0, x Value at which a Boltzmann Sigmoid Curve has a y-Value Equal to $(A_1+A_2)/2$ (any unit)

dx, Stretch Parameter of a Boltzmann Sigmoid Curve (any unit)

σ, Standard Deviation (any unit)

R^2, Coefficient of Determination ($-1<R^2<1$, unitless)

List of Figures

List of Tables

Acknowledgements

If you don't know me, my friends, or my family, you might as well skip this part. It doesn't have much scientific merit, but I felt the need to write it here anyway.

Kelsey Hatch Cardon, my wife, has been the most influential person in my life for the last five years. It takes a lot of patience to wait for a husband who comes home late every day, works Saturdays and most holidays, and still doesn't get paid much (like a LEO but lame). She has really helped me keep my priorities straight by reminding me what matters most.

Kelsey's parents, Book and Cindy, also deserve a shout out. They provided me with almost every shirt that I ever wore as well as forcing me to take every vacation that I ever took and helping with a bunch of other important things like a car, helping us move, and being there when Terra was first born.

I think the people who deserve the most credit for my ultimate decision to go to grad school and for the character to push through it are my parents David and Donna. My dad taught me algebra as a kindergarten student by posing it as a magic puzzle box game that I got to play in church when the speakers were boring. My mom brought me home a fresh stack of library books to read every week and I chewed through thousands of them. I hope that they can be proud of their oldest son.

I have had three chemistry mentors throughout the years. The first was Dr. David Shelton who was independently wealthy and taught chemistry at a high school for fun. The old devil deserves credit for turning me down to the dark side of applied sciences away from the purer virtues of physics and mathematics that my father instilled in me.

I had the fortune of taking Dr. Steven Castle's undergraduate organic chemistry course my freshman year at BYU. It was so interesting that I asked if I could work in his lab and he has been watching out for me ever since. Besides personally teaching me how to be a decent organic chemist, he also landed me paid positions tutoring chemistry and doing research and helped me get my internship after graduating. I'm pretty sure the only reason I got accepted into UCI was because he wrote a good letter of recommendation for me directly aimed at Larry Overman, who was his own advisor once upon a time. At the time of writing, I still have more publications from his group than my graduate career. Suffice it to say, he is a great mentor and I owe him.

No acknowledgment section would be complete without my PhD advisor, Dr. Shane Ardo. I heard a lot of horror stories about graduate school and the irrational intolerance principal investigators have of normal human behavior in their underlings. Shane is actually very nice and understands that sometimes life outside of academics happens and you need to take paternity leave or go home at a reasonable hour because your kids have an early bedtime. Shane attracts so many brilliant, enthusiastic, and socially mature individuals to his group because he demonstrates those qualities himself.

I would also like to thank Obadiah Reed of NREL and Malcom Forbes at Bowling Green State University for taking some time away from their own research to explain to me the principals of transient conductivity measurements. Dima Fishman at UCI's own Laser Spectroscopy Laboratory was helpful in designing our nanosecond transient absorption spectrometer.

A lot of other lab members worked on this research project and sometimes it is hard to disentangle their contributions from mine. Kevin Tkaczibson designed, built, and programed the first working version of the nsTA system and TrMC systems, is a good DM, and is a great friend. Simon Luo was key in designing, building, and troubleshooting all the laser detection systems. David Fabian first got the ball rolling on the TrMC. Dr. Hsiang-Yun Chen was the original owner of the dye sensitized solar cell project and passed it down to me. Gregory Krueper and Jaqueline Angsono did a lot of work on the hole-hopping project and created the first draft of that paper. Nazila Farhang made a host of good solar cells varying redox shuttle potential. Cassidy Feltenberger is my scion and will hopefully be able to take all of this stuff and turn it into something useful in the future. All of these people are good friends and it has been a pleasure to work beside them.

I would like to thank my thesis committee members, Shane Ardo, Matt Law, and Alan Heyduk for providing help along the way and maybe even reading this.

This work was supported by the School of Physical Sciences and the Department of Chemistry at the University of California Irvine and the National Science Foundation under CHE – 1566160. The author acknowledge the NMR Facility for NMR measurements, The Laboratory for Electron and X-ray Instrumentation (LEXI) for scanning electron microscopy measurements and the Mass Spectrometry Facility for MALDI-MS measurements. Profilometry was conducted using the facilities in the University of California, Irvine's Integrated Nanosystems Research Facility (INRF). The author thanks Professor Peter de Lijser for his generous donation of a nanosecond transient absorption spectroscopy system that was modified for these studies. J.M.C. weas supported by a National Science Foundation Graduate Research Fellowship under grant no. DGE-1321846. J.M.C. was also supported by a generous donation by the Joan Rowland

Foundation. He would also like to thank Fusion Conferences for a generous travel grant to attend the Frontiers in Photochemistry 2018 conference.

Curriculum Vitae

Joseph Michael Cardon

2011-13 Undergraduate Research Assistant in Dr. Castle's Lab, Brigham Young University, Provo, UT.

2013 BS Chemistry, Brigham Young University, Provo, UT

2014 Polymer Chemist, Turner Innovations, Orem, UT

2014-2019 Graduate Research Assistant in Shane Ardo's Research Group, University of California, Irvine, Irvine, CA

2019 PhD Chemistry , University of California, Irvine, Irvine, CA

FIELD OF STUDY

Chemistry

PUBLICATIONS

Joseph Cardon, James Coombs, Daniel Ess, Steven Castle, Insights into Base-Free OsO_4-catalyzed Aminohydroxylations Employing Chiral Ligands, *Tetrahedron*, 2019.

Zhiwei Ma, Jintao Jiang, Shi Luo, Yu Cai, **Joseph M. Cardon**, Benjamin M. Kay, Daniel H. Ess, Steven L. Castle, Selective Access to E- and Z-ΔIle-Containing Peptides via a Stereospecific E2 Dehydration and an O → N Acyl Transfer *Org. Lett.*, 2014, *16* (15), 4044–4047.

Shane Ardo, William White, Christopher Douglass Sanborn, **Joseph M. Cardon**, Ronald Reiter, Eric Schwartz, Light-Driven Ion-Pumping Membrane Systems, Patent, University of California Irvine 2018, 15/698,324 (Provisional patent (2016) 62/384,503); Publication number US20180065095.

Shane Ardo, Eric Schwartz, J. Liu, **Joseph Cardon**, William White, Kevin Tkacz, Lawrence A. Renna, M. Modestino, D. Blanco, Devices for Integrated Solar Photodialysis of Salt Water, Provisional Patent Application, University of California Irvine (2018) 2018-525-1, UCI 18.06 PROV.

Joseph M. Cardon, Tom Youd, D. Clark Turner, Radiation Shielding and Processes for Producing and Using the Same, Patent, Turner Innovations, August 25, 2014, 14/148011; Publication number US10,026,513.

ABSTRACT OF THE DISSERTATION

Synthesis and Characterization of Infrared-Absorbing Osmium-Polypyridyl Dyes for Use in Dye-Sensitized Solar Cells

By

Joseph Michael Cardon

Doctor of Philosophy in Chemistry

University of California, Irvine, 2019

Associate Professor Shane Ardo, Chair

Dye-sensitized solar cells (DSSCs) are a potentially low-cost alternative to silicon solar cells, however DSSCs have not been largely commercialized due to their poor solar to electric energy conversion efficiency, ~14%, compared to silicon, ~25%. One reason for their poor efficiency is that current record holding DSSCs employ dyes that absorb a less-than-ideal portion of the solar spectrum as dictated by the Shockley-Queisser Limit. To remedy this, infrared-absorbing osmium polypyridyl dyes were synthesized and their basic parameters characterized by ultraviolet-visible absorption spectroscopy, stepwise potential step spectroelectrochemistry, and cyclic voltammetry. The dyes appeared to have close-to-ideal optical pseudo-bandgaps and excited state energy levels, however, their performance in DSSCs employing the commonly used iodide-triodide redox shuttle was very poor. To better understand the behavior of these dyes in a working environment apparent diffusion coefficients of later self-exchange electron transfer between oxidized and reduced dyes bound to mesoporous titanium dioxide films was studied

using several different techniques which produced different results. The different techniques were able to be harmonized by correct use of mathematical assumptions and measurement of non-ideal Nernstian behavior of bound dyes. Foot-of-the-wave analysis was modified for use on dyes bound to mesoporous films with substrate in solution. This revealed that several infrared absorbing osmium polypyridyl dyes performed very slow electron transfer from iodide with maximum second order electron transfer rate constants of 78 M^{-1} s^{-1}, which could explain their poor performance in DSSCs using the iodide triiodide redox shuttle. Rates with 1,1'-dimethyl ferrocene were much faster, with rate constants as high as 74,000 $M^{-1}s^{-1}$. Nanosecond transient absorption spectroscopy and nanosecond transient microwave conductivity measurements were performed on DSSCs containing working benchmark dye N3 and infrared-absorbing osmium polypyridyl dyes. Osmium polypyidyl dyes were observed to successfully inject electrons into the TiO_2 film with electron in TiO_2 to oxidized dye recombination rates comparable to N3. Oxidized N3 rapidly regenerated in the presence of iodide, resulting in charge separated states that lasted for almost a second, but the infrared-absorbing osmium dyed did not. Several catalysts were fabricated to speed up iodide oxidation, but none worked in a solar cell.

Introduction to Dye Sensitized Solar Cells

Summary

Dye-sensitized solar cells (DSSCs) are a third-generation Schottky-junction-like solar cell technology that utilize dyes as the light absorption layer, a wide bandgap semiconductor as the semiconductor, and a molecular or polymeric redox couple as the metallic contact. The abundance of dyes, redox couples, and semiconductor morphologies and modifications available create an enormous phase space for use and scientific exploration. DSSCs have been made which are mechanically flexible,[1] semi-transparent,[2] multi-colored,[3] efficient under indoor low-light conditions,[4,5] n-type,[6] p-type,[7] are made using natural plant dyes,[8] use inexpensive materials,[3] and contain multiple absorbing layers.[9] Unfortunately, DSSCs are not currently as efficient as silicon solar cells which is a major barrier to commercialization. The reason for the poor efficiency of DSSCs is that, currently, all successful DSSC dyes do not absorb enough of the solar spectrum to efficiently harvest sunlight.

This dissertation will discuss in greater depth the need for infrared-absorbing DSSC dyes as well as the synthesis and characterization of several promising infrared absorbing dyes. DSSCs made using these dyes did not perform as hoped and so photoelectrochemical techniques, foot-of-the-wave analysis (FoTW), nanosecond transient absorption spectroscopy (nsTA), and nanosecond transient microwave conductivity (TrMC) were employed to determine the cause of failure was poor dye regeneration kinetics by the redox shuttle. Several potential charge transfer catalysts were synthesized, characterized, and incorporated into DSSCs without success.

Alternative solutions are proposed, and the broader utility of newly developed techniques is discussed.

What is a DSSC?

DSSCs are devices which convert light energy to electrical energy with the light absorber being a dye which is bound to a hard, inorganic, wide-bandgap semiconductor. They are distinct from semiconductor solar cells, which utilize a narrow-bandgap semiconductor as the light absorber, and organic photovoltaics, which use dyes bound to soft, organic semiconductors.[10] DSSCs can be n-type, where an excited dye transfers an electron to the semiconductor conduction band, or p-type, where an excited dye accepts an electron from the semiconductor valence band. The majority of DSSCs, including all the DSSCs discussed in this dissertation, are n-type. For the sake of simplicity, all discussion from this point on will consider only n-type DSSCs.

DSSCs are composed of five layers which are illustrated with their relative energy levels in **Figure 1**.

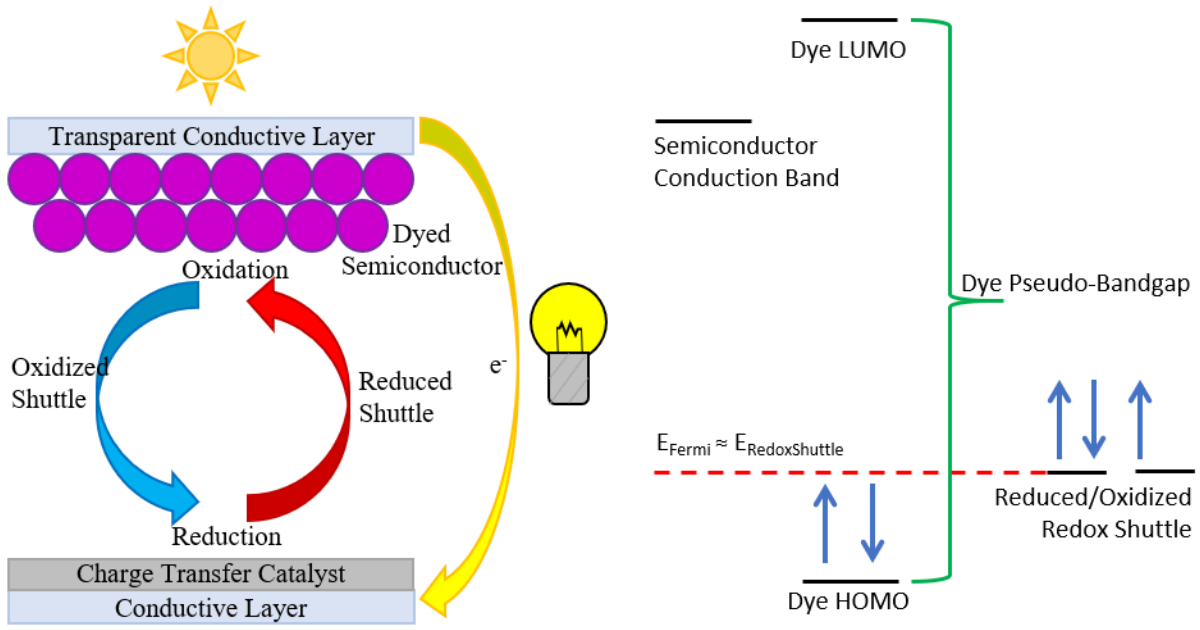

Figure 1: Left: A cartoon diagram of an n-type DSSC. Right: A generalized simple energy diagram for an n-type DSSC.

1. Transparent Conductive Layer

The purpose of the transparent conductive layer is to provide a solid, electronically conductive scaffold for the semiconductor. The transparent conductive layer contacts the anode of the external circuit where the electrical energy produced by the DCCS is used. The transparent conductive layer must be transparent so that light can penetrate into the interior of the DSSC and reach the dyes. It is metallic in nature and in intimate contact with the semiconductor so its Fermi level equilibrates with the Fermi level of the semiconductor. The most commonly used transparent conductive layers materials are fluorine doped tin oxide (FTO) and indium doped tin oxide.

2. Wide-Bandgap Semiconductor

One purpose of the semiconductor is to form a high-surface area scaffold for the dyes to occupy. The higher the surface area, the greater the concentration of dyes and the thinner the final device can be, which helps reduce resistance. The other purpose is to act as an electron

transport material that carries the excited electrons produced by the attached dyes to the anode. The mobile excited electrons occupy the otherwise empty conduction band of the metal oxide semiconductor. In the dark, the Fermi level of the semiconductor is determined by the potential of the redox electrolyte. The most commonly used wide bandgap semiconductor is titanium (IV) oxide (TiO_2).

3. Dye

The dye is the powerhouse of the DSSC, absorbing light and producing excited electrons. It is important that the excited state energy level of the dye exceeds the energy level, or potential, of the bottom of the metal oxide conduction band. This allows the dye to inject an excited electron into the conduction band of the metal oxide. The energy difference between the dye ground state and excited state energies is called the pseudo-bandgap of the dye and determines the maximum wavelength of light can be effectively absorbed by the dye. The dye can be considered to be a mid-bandgap dopant of the semiconductor. The total number of dyes is small compared to the total amount of redox shuttle and so the redox shuttle potential determines the ratio of oxidized and reduced dyes in the absence of light.

4. Redox Electrolyte

The redox electrolyte mediates positive charge transfer between the dyes and the counter electrode. After a dye injects an excited electron into the metal oxide semiconductor, it is in its oxidized form. The redox electrolyte donates an electron to the oxidized dye, regenerating it so it can be excited by light once again. The now oxidized redox electrolyte diffuses to the counter electrode where it accepts an electron and returns to its original form. The redox electrolyte is composed of a mixture of oxidized and reduced redox shuttle, generating a partially filled band

of oxidation states so it can be considered to be a metallic material. The redox electrolyte determines the Fermi energy of the entire system.

4. Metallic Cathode

The metallic cathode donates electrons to the oxidized redox electrolyte, reducing it back to its original form. The cathode must have a surface capable of catalyzing the reduction so a catalyst is often added. The cathode is metallic in nature so its Fermi energy equilibrates with the potential of the surrounding redox electrolyte. The most commonly used cathode is platinum nanoparticles deposited on FTO.

DSSCs in the Light

The sequence of events that occurs in a working DSSC when it is illuminated by light are shown in **Figure 2**. A photon strikes the dye and excites and electron. This electron injects into the metal oxide conduction band. The redox electrolyte regenerates the ground state of the dye. The cathode electrode then regenerates the redox electrolyte. The metallic cathode receives its electron from the injected electron in the valence band of the metal oxide after the electron passes through an external circuit

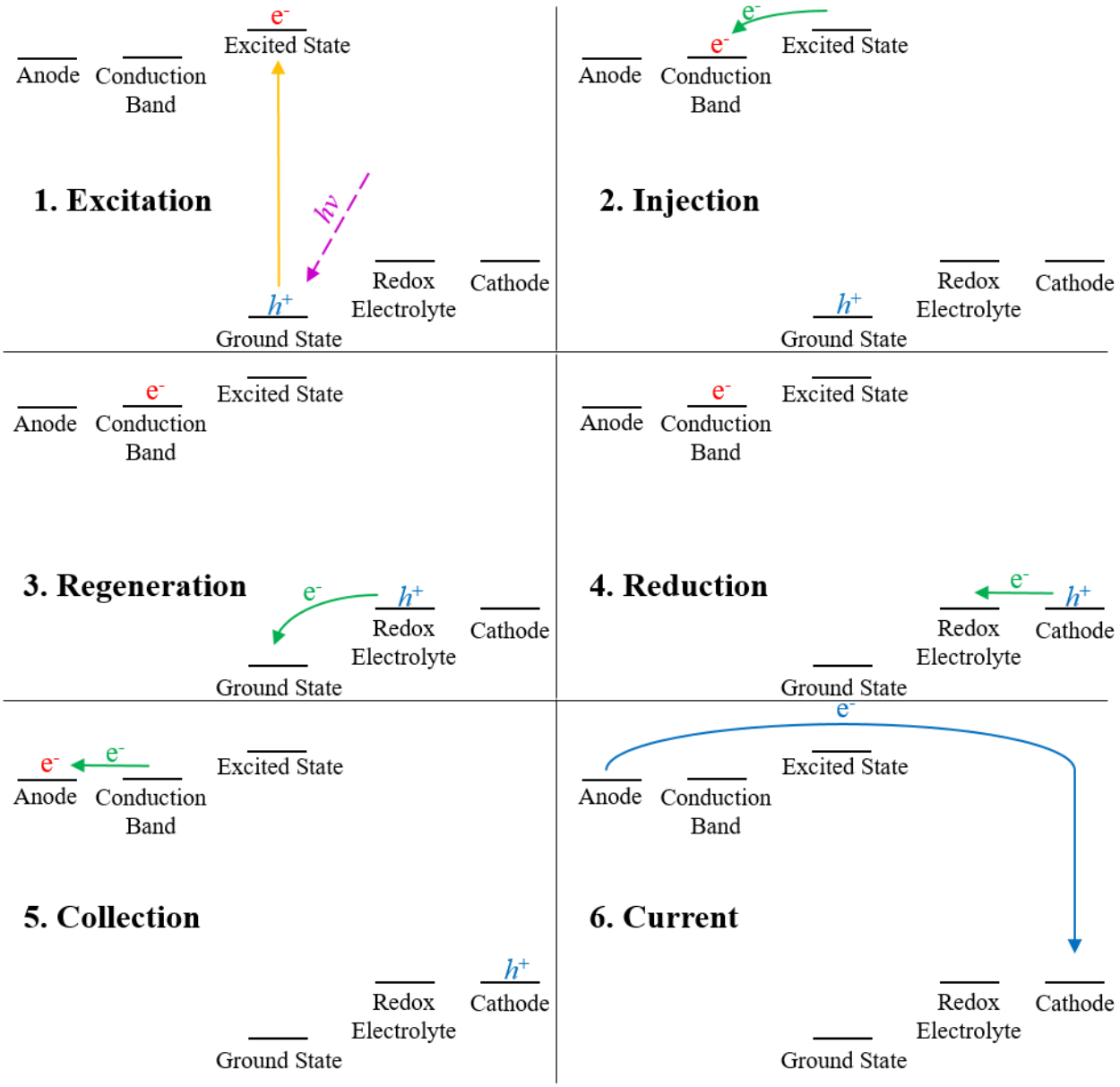

Figure 2: Energy level diagrams of a simple DSSC with arrows depicting fundamental electron transfer events.

This sequence of events creates a non-equilibrium excess of electrons in the semiconductor conduction band and a deficit of electrons in the redox electrolyte. The electrochemical potential of the semiconductor is largely affected, creating a quasi-Fermi level that just positive of the bottom of the conduction band. The potential of the redox electrolyte becomes more positive, but less drastically. The difference in potential between the conduction

band and the redox electrolyte determines the maximum voltage output of the cell as illustrated in **Figure 3**. Notice that the maximum voltage output is less than the dye pseudo-bandgap. The maximum voltage output can only match the dye pseudo-bandgap if the charge separated state lifetime is close to infinite, which is not realistically achievable. Also notice that the voltage output of the cell is most heavily determined, not by the dye pseudo-bandgap, but by the energy level of the semiconductor conduction band and the potential of the redox shuttle.

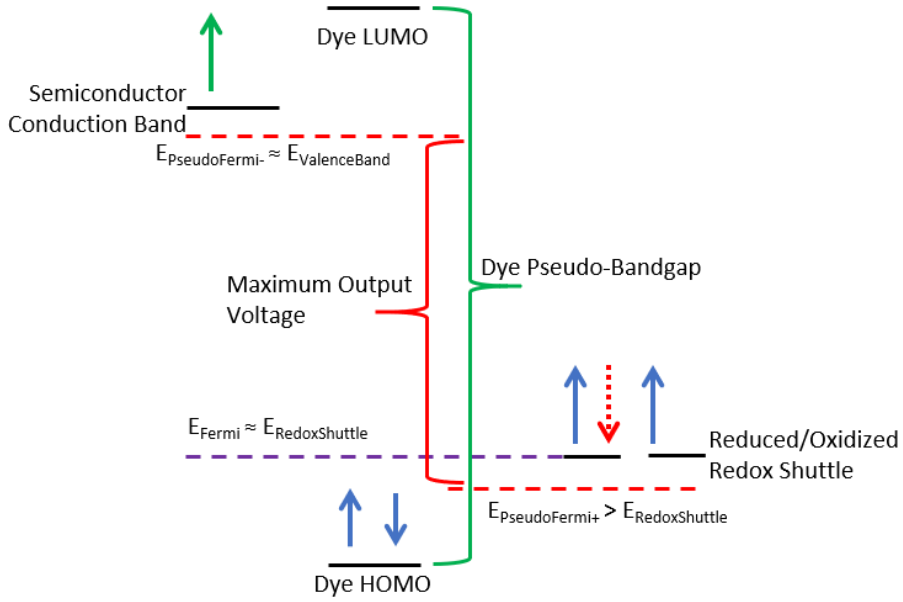

Figure 3: A labeled energy level diagram of a simple DSSC under illumination.

Recombination Pathways

There are a number of unproductive pathways which consume excited electrons. Unproductive reversible pathways are called recombination pathways, recombination modes, or shunts. They do not damage the cell but do cause it to be less effective. These pathways are illustrated in **Figure 4**. Irreversible pathways cause cell degradation and will not be discussed here.

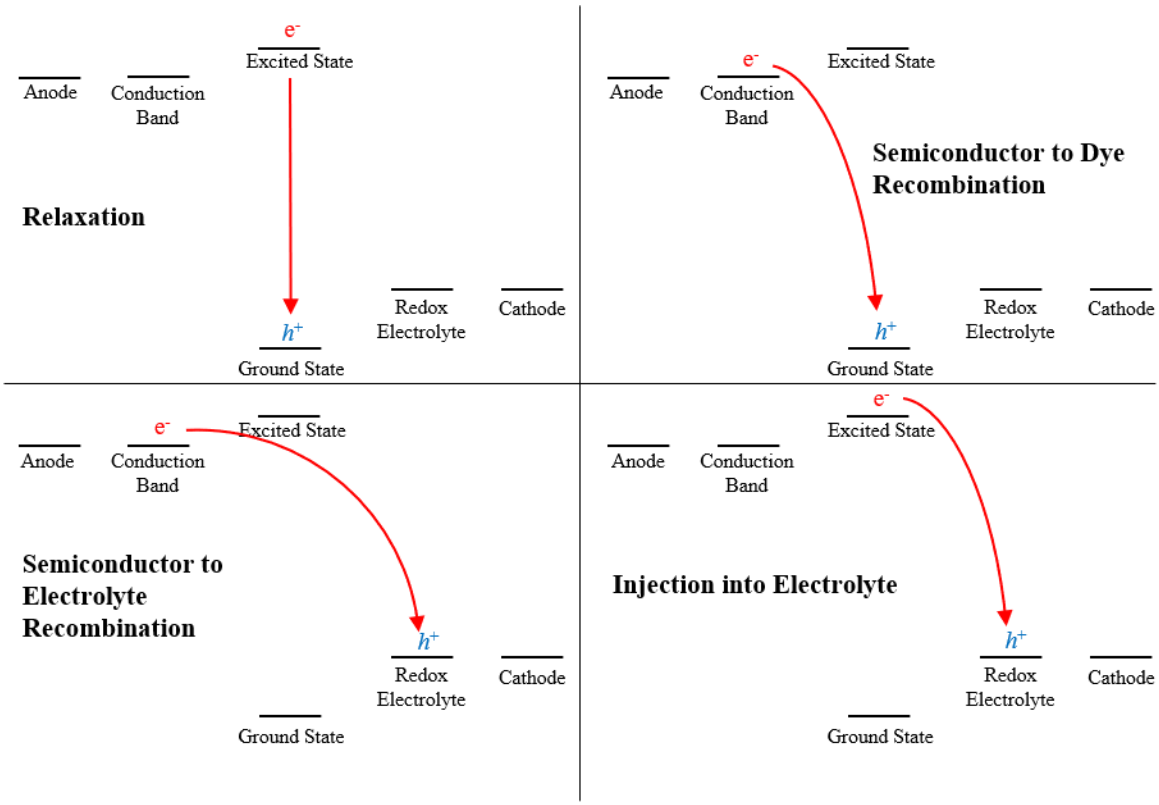

Figure 4: Energy level diagrams of a simple DSSC with arrows depicting recombination events.

Excitation Relaxation Recombination, Failure to Inject

If an excited dye fails to inject an excited electron into the metal oxide conduction band eventually the dye will relax back to its ground state through either radiative or non-radiative mechanisms. This results in a loss of current. In order to encourage rapid injection relative to relaxation, efficient dyes are designed to have high electron density near the metal oxide surface in their excited state using a donor-acceptor motif.[11,12] The donor-acceptor motif also extends the dye excited state lifetime by separating and stabilizing charge density in the excited state.[13] Another method to prevent injection failure is to design dyes that have excited state energy levels significantly higher in energy than the metal oxide conduction band. This difference in energies provides a thermodynamic driving force for injection. However, the it also introduces a loss of potential which decreases the cell efficiency.

In state of the art DSSCs, relaxation occurs on a timescale of 10 to 50 nanoseconds and injection occurs on a timescale of one picosecond.[14] Because injection is four orders of magnitude faster than relaxation, relaxation recombination does not account for significant current loss. An exception exists when the dye excited state does not have sufficient energy to inject into the metal oxide conduction band. If injection is not thermodynamically favored, then relaxation recombination is the primary mechanism of current loss.

Semiconductor-to-Dye Recombination, Failure to Regenerate

If an oxidized dye is not regenerated by the redox electrolyte, eventually the injected electron in the semiconductor conduction band will recombine with the dye. This recombination results in loss of current. To encourage rapid regeneration relative to semiconductor-to-dye recombination high concentrations of redox electrolyte are usually employed. It is also important that the redox electrolyte have a rapid diffusion coefficient so it can quickly reach the oxidized dyes. Another method that is commonly employed is to use a redox electrolyte with potential significantly higher than the ground state energy of the dye. This overpotential provides a thermodynamic driving force for regeneration but also introduces a loss of cell potential and efficiency.

In state of the art DSSCs regeneration occurs on a timescale of hundreds of nanoseconds to tens of microseconds depending on electrolyte concentration, counter ions, and other factors, and metal oxide-dye recombination occurs on a timescale of milliseconds with no applied bias to microseconds at high applied bias.[14] Because regeneration is much faster than recombination, metal oxide-dye recombination does not account for most of the current lost, at least at low applied bias.

Metal Oxide-Redox Electrolyte Recombination: Failure to Separate

If the semiconductor surface is exposed, it may come in contact with oxidized redox electrolyte. When this occurs, electrons injected into the metal oxide conduction band may recombine with the oxidized dye and reduce it back to its original state. This recombination results in loss of current. In order to prevent metal oxide-redox electrolyte recombination, blocking layers are added to the metal oxide surface to prevent collision between the metal oxide and redox electrolyte.

The prevailing opinion is semiconductor-redox electrolyte recombination is the primary recombination pathway. This theory is supported by studies showing that blocking layers increase DSSC efficiency by preventing this mode of recombination[12,15,16] However, some studies claim that depletion of the redox electrolyte inside the pores of the dyed mesoporous semiconductor leads to slow regeneration of the dye relative to semiconductor-dye recombination.[17] Other studies claim that the high electronic bias present under operating conditions leads to faster semiconductor-dye recombination than theoretical studies expect.[14,18]

Injection into Electrolyte: Failure to Select

If the excited dye comes into contact with oxidized redox electrolyte, it may inject an electron into the electrolyte, reducing it, instead of injecting into the semiconductor conduction band. This recombination results in loss of current. In order to encourage rapid injection into the semiconductor relative to injection into electrolyte, efficient dyes are designed to have high electron density near the metal oxide surface and low electron density at the electrolyte interface in their excited state using a donor-acceptor motif.[11,12] Also, the minimum required concentration of oxidized electrolyte species is maintained to allow fast electrolyte reduction at the cathode. Also, many redox electrolytes undergo irreversible chemical changes after electron transfer so

that electron transfer from electrolyte to dye is easier than electron transfer from dye to electrolyte. This will be discussed for two couples, the I^-/I_3^- redox shuttle and cobalt(II/III) complexes below.

Extra Interesting DSSCs

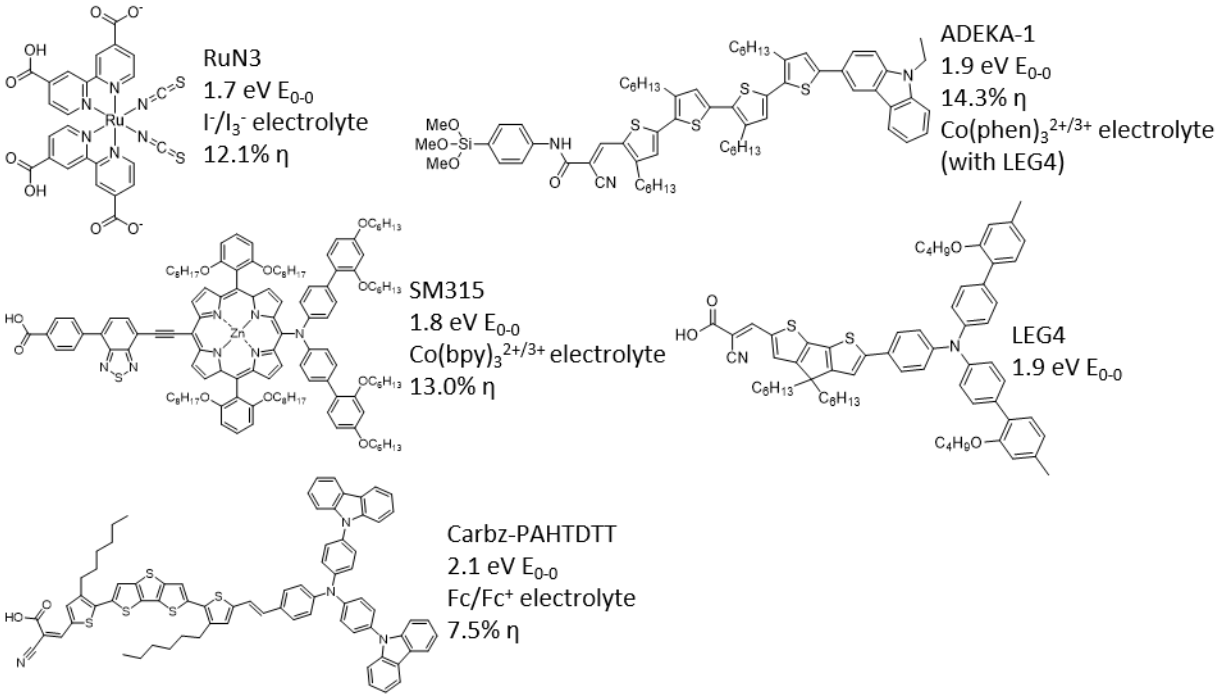

Figure 5: Structures of dyes of interesting DSSCs with dye name, pseudo-bandgap, redox electrolyte active species, and efficiency to the right of each dye structure.

N719 Ruthenium Polypyridyl Dye

The ruthenium dye N719 (**Figure 5**) set the record for DSSC solar to electric energy efficiency at 12.3% from 1993,[19] when it was first discovered. Even now, N719 and its fully protonated analogue N3 remain benchmarks dyes in DSSC research. An N719 dyed cell uses rutile-anatase titanium dioxide, TiO_2, as the semiconductor and a platinum counter electrode. It also uses the iodide-triiodide (I^-/I_3^-) redox shuttle in acetonitrile solution.[20] This redox shuttle exhibits unique chemistry compared with other redox shuttles which provides both advantages and disadvantages.

After an excited dye injects an electron it oxidizes two I^- to diiodide (I_2^-) via a single-electron process. Two I_2^- quickly disproportionate in solution to form I_3^- and I^-. I_3^- exhibits extremely slow recombination with TiO_2 and oxidized N719.[21] This slow recombination is due to three main reasons. The first is the donor-acceptor nature of the dyes, with the electron rich isothiocyanate dyes and ruthenium(II) core as the donor and the carboxylate groups as acceptor. The second is that the N719 dye is net negatively charged. This charge prevents negative ions, which includes I^-, $I_2^{\cdot-}$, and I_3^-, from reaching the TiO_2 surface via Donnan exclusion.[22] The third is that there is a reduced driving force and kinetic penalty to undergo two-electron transfer to I_3^- compared to one-electron transfer to $I_2^{\cdot-}$. Slow recombination is the primary advantage of the I^-/I_3^- redox shuttle. Unfortunately, the I^-/I_3^- redox couple has a higher redox potential than the I^-/I_2^- redox couple and determines the solution potential because it comprises the major species in solution. The dye must have a ground state energy low enough to rapidly oxidize I^- to I_2^-, a reaction with a high activation energy, but the potential of the counter electrode matches the potential of I_3^-. This translates to a potential loss of up to 500 mV and is the major shortcoming of the I^-/I_3^- redox shuttle.

SM315 Zinc Porphyrin Dye

The zinc porphyrin dye SM315 (**Figure 5**) held the record for DSSC solar to electric energy efficiency at 13.0% from 2014[12] until 2015.[23] The DSSC used TiO_2 as the semiconductor, a graphene nanoplatelets on FTO counter electrode, and $Co(bpy)_3^{2+/3+}$ (where bpy is 2,2'-bipyridine) redox electrolyte. This redox shuttle also exhitis unique chemistry which provides similar advantages and disadvantages to I^-/I_3^- but to a lesser extent. $Co(bpy)_2^{2+}$ is naturally high spin, with three unpaired electrons, however $Co(bpy)_2^{3+}$ is naturally low spin, with no unpaired electrons. When $Co(bpy)_2^{2+}$ is first oxidized, it generates high spin $Co(bpy)_3^{3+}$ which undergoes a

spin flip to a low spin state. Low spin $Co(bpy)_2^{2+}$ exhibits slow recombination with both TiO_2 and oxidized dye. This slow recombination is due to four reasons. The first is that donor acceptor nature of the dye with the zinc porphyrin as the donor and the carboxylate group as the acceptor. The second is that SM315 has bulky 6 and 8 carbon alkane chain side groups that physically block large molecules like $Co(bpy)_3^{3+}$ from reaching the TiO_2 surface. The third is that SM315 has a 1+ or 2+ charge depending on the protonation state of the carboxylate group and so the layer of SM315 dyes on TiO_2 surface inhibits positively charged ions via Donnan exclusion. The fourth is that there is a reduced driving force and kinetic penalty to transfer an electron to low spin versus high spin $Co(bpy)_3^{2+}$. This fourth reason slows dye injection into electrolyte but also introduces an additional 200 mV overpotential required between dye and redox electrolyte to overcome the spin flip energy and regenerate dye quickly enough to avoid semiconductor-to-dye recombination. This 200 mV potential loss allows for more efficient cells than those that use the I^-/I_3^- redox shuttle, especially since the electrolyte potential can be tuned by changing the ligands on cobalt,[24,25] but is still a major shortcoming of the $Co(bpy)_2^{2+/3+}$ redox electrolyte.

ADEKA-1 and LEG4 Organic Dyes

A DSSC co-sensitized with both ADEKA-1 polythiophene silyl-anchor dye and LEG4 triarlyamine carboxylate-anchor dye (**Figure 5**) held the record for DSSC solar to electric energy efficiency at 14.3% from 2015 onwards.[23] It is possible that it may have been beaten, but I haven't seen the paper, as of July 2019. This DSSC use TiO_2 as the semiconductor, a gold-plated FTO with gold nanoparticle counter electrode, and $Co(phen)^{2+/3+}$ (where phen is phenanthroline) redox shuttle. Both dyes exhibit the donor acceptor motif individually, but together they form an intermolecular donor-acceptor complex. When either LEG4 or ADEKA-1 is excited, electron transfer can occur from ADEKA-1 to LEG4 followed by injection into TiO_2 by LEG4. This

results in oxidized ADEKA-1 and reduced LEG4. ADEKA-1 is in better electrical contact with the redox electrolyte and poorer electrical contact with TiO_2 than LEG4, which promotes regeneration and inhibits TiO_2 to dye recombination relative to a singly-sensitized system. $Co(phen)^{2+/3+}$ has all the same characteristics as $Co(bpy)^{2+/3+}$ in the SM315 cell, except that ADEKA1 and LEG4 are not positively charged and do not cause Donnan exclusion. Instead, a blocking layer composed of five different silyl-alkanes and an alkyl-phosphonate was deposited to sterically prevent redox shuttle from reaching the TiO_2 surface.

Carbz-PAHTDTT Organic Dye with Ferrocene Redox Shuttle

This DSSC is interesting, not because it is highly efficient, only 7.5%, but because its redox couple, ferrocene/ferrocenium (Fc/Fc^+) is reversible. The DSSC used Carbz-PAHTDTT triarylamine organic dye (**Figure 5**), TiO_2 as the semiconductor, and a platinized FTO counter electrode. To prevent recombination the dye had a donor-acceptor motif and bulky alkyl side chains to protect the TiO_2 surface. An additional blocking layer of chenodeoxycholic acid also prevented ferrocenium from reaching the surface. In comparison, a DSSC using I^-/I_3^- with the same dye produced the same current as the Fc/Fc^+ cell at a decreased voltage.

The Shockley-Queisser Limit: Why DSSCs Aren't Efficient

In 1961, William Shockley and Hans-Joachim Queisser outlined the fundamental physical efficiency limit of a single-junction PN-type solar cell of a given bandgap and light source. Approximating the sun as a blackbody light source, they calculated a maximum solar to electric energy efficiency of 30% for a solar cell with 1.1 eV bandgap.[26] More recent calculations using the same method but using the standard AM1.5 solar spectrum calculate a maximum efficiency of 33.7% at for a solar cell with a 1.34 eV bandgap.[27] Most of the assumptions for the

Shockley-Queisser limit also apply to DSSCs, specifically that photons above the dye bandgap are not absorbed and so their energy is not collected, that photons with energy greater than the bandgap are absorbed, but excess energy is lost through rapid thermalization to the lowest energy excited state, and that a single photon generates a single electron-hole pair. One assumptions are not so good. DSSCs rarely recombine via radiative processes, which introduces inefficiency not accounted for in the Shockley-Queisser limit. In spite of this dissimilarity, the Shockley-Queisser limit can be used as a good first order approximation of whether a dye, with its associated pseudo-bandgap, could ever produce a highly efficient solar cell.

N719, SM315, ADEKA-1, LEG4, and Carbz-PAHTDTT have pseudo-bandgaps of 1.7, 1.8, 1.9, 1.9, and 2.1 eV respectively which translates to maximum possible efficiencies of 29, 27, 25, 25, and 21% respectively. Interestingly, with the exception of Carbz-PAHTDTT, decreasing maximum theoretical efficiency is concurrent with increasing actual efficiency. Also interesting, is that ADEKA-1 and LEG4, the current DSSC record holders, even if they were perfected, would only be as efficient as a real, not-perfected, monocrystalline silicon solar cell.[28] It is surprising that dyes with more ideal pseudo-bandgaps, in the range of 1.0 to 1.6 eV, capable of exceeding 30% efficiency, are not used given the synthetically flexible nature of dyes.

Implications of Narrower Pseudo-Bandgap DSSCs

One implication of using narrower pseudo-bandgap DSSCs is that the dyes will absorb longer wavelengths of light. Dyes with pseudo-bandgaps of 1.6, 1.34, and 1.0 eV will absorb out to approximately 775, 925, and 1240 nm respectively. The total amount of light absorbed, and the resulting short current density will also increase to approximately 26, 36, and 48 mA cm^{-2} respectively illustrated in **Figure 6**. This is a large increase from short circuit currents of ~20 mA

cm^{-2} in record setting dyes. Resistive losses and mass transport issues would be likely to arise if the cells could not be made thin enough and the redox electrolyte concentrated enough to handle the larger currents.

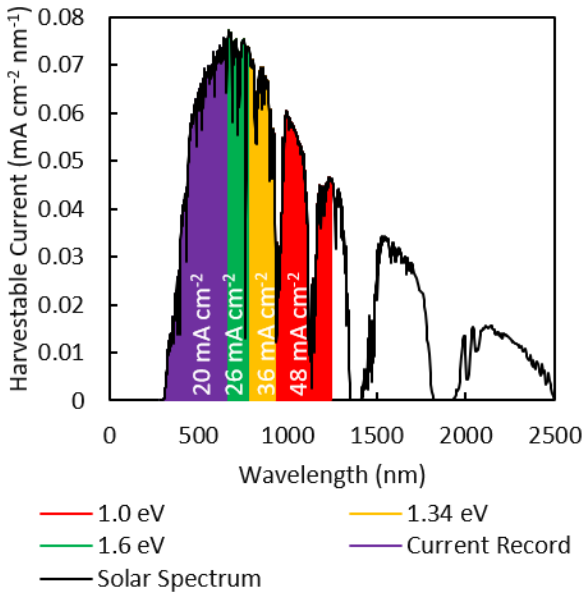

Figure 6: AM 1.5G solar spectrum showing total harvestable current in mA cm^{-2} nm^{-1} as a function of wavelength assuming one excited electron generated per photon (black), current record efficiency DSSC light harvest (purple), and additional light harvested for DSSCs with bandgaps of 1.6 eV (green), 1.34 eV (orange), and 1.0 eV (red) with total harvested current labeled in white text.

A second implication is that the choice of redox electrolyte might have to change. Assuming the use of TiO_2 as the wide bandgap semiconductor, the conduction band acceptor state energy levels will be at -0.8 V vs Saturated Calomel Reference Electrode (SCE).[14,29–31] In order to inject without wasting energy, the excited state of the dyes will need to be ~0.1 V negative of the conduction band, or ~-0.9 V vs SCE.[14,32] This is a standard excited state energy level for both organic and metal coordination complex dyes with carboxyl anchoring groups.[6] Assuming an ideal bandgap of 1.34 eV, the ground state formal redox potential of the dye must be ~ +0.4 V vs SCE. In order for the dye to be mostly in the reduced form in the dark and to provide sufficient driving force for regeneration, the redox shuttle potential must be at least 0.2

V negative of the dye potential, ~ +0.2 V vs SCE. Redox shuttles usually work best within a ~0.1 V range of their formal reduction potential so the redox shuttle potential must fall be regative of +0.3 V vs SCE. Several couples that have this characteristic are I^-/I_3^-, $Co(dmbpy)_3^{2+/3+}$ (where dmbpy is 4,4'-dimethyl-2,2'-bipyridine), $Co(dmobpy)_3^{2+/3+}$ (where dmobpy is 4,4'-dimethoxy-2,2'-bipyridine), and $dmFc^{0/1+}$ (where dmFc is 1,1'-dimethylferrocene) with redox potentials of 0.11, 0.19, 0.13, and 0.27 V vs SCE respectively.[15,17,25]

Conclusions

Dye-sensitized solar cells are a promising alternative to silicon solar cells but lack the efficiency necessary to compete. One source of this inefficiency is the larger than necessary bandgaps of currently used dyes. Using dyes with narrower bandgaps would likely introduce new challenges to cell efficiency which would require modification of the redox electrolyte. The remainder of this thesis will discuss several promising narrow bandgap dyes and the methods used to characterize their interactions with the redox electrolyte.

Good DSSC Review Papers

I have found the following review papers to be so helpful that they deserve their own special section.

"Dye-sensitized solar cells: A brief overview"[33] by Nazeeruddin, Baranoff, and Gratzel. This is a good, simple introduction which is great for beginners.

"Dye-Sensitized Solar Cells"[1] by Hagfeldt, Boschloo, Sun, Kloo, and Pettersson This is a very in-depth review of all aspects of DSSCs.

"Iodide Chemistry in Dye-Sensitized Solar Cells: Making and Breaking I-I Bonds for Solar Energy Conversion"[17] by Rowley, Farnum, Ardo, and Meyer. This review examines the I^-/I_3^- redox shuttle in a well laid out way.

"Near-infrared Sensitization in Dye-sensitized Solar Cells"[34] by Park, Viscardi, Barolo, and Barbero. This review lists most of the near infrared absorbers used in DSSCs before 2013. My dyes absorb even more infrared than theirs do, but all infrared dyes suffer the same challenge of slow regeneration.

"Metal Coordination Complexes as Redox Mediators in Regenerative Dye-Sensitized Solar Cells"[25] by Saygili, Stojanovic, Flores-Diaz, Zakeeruddin, Vlachopoulos, Gratzel, and Hagfeldt. This review contains a comprehensive list of all metal containing redox shuttles used in DSSCs.

Photoelectrochemical Characterization of Infrared-Absorbing Osmium Polypyridyl Dyes

Introduction

I purchased or synthesized five dyes which will be referenced and characterized extensively throughout the remainder of this thesis. The structures of these dyes are found in **Figure 7**.

***cis*-Ru(dcbpy)$_2$(NCS)$_2$** (dcbpy is an abbreviation for 4,4'-dicarboxy-2,2'-bipyridine), abbreviated RuN3, is a commercially available benchmark DSSC dye invented by Michael Gratzel's group known to make solar cells with solar to electric energy conversion efficiencies over 10%.[35,36] RuN3 has an optical pseudo-bandgap of 1.69 eV which prevents it from achieving the highest solar to electric energy conversion efficiencies dictated by the Shockley-Queissar Limit which peaks around 33% for bandgaps of 1.2 and 1.4 eV.[26] RuN3 is used in this thesis as a positive control for necessary solar cell processes such as excitation, injection, regeneration, and lack of recombination. It was chosen for its abundant use in existing literature and its structural similarity to the four infrared-absorbing osmium polypyridyl dyes with narrow pseudo-bandgaps.

***cis*-Os(dcbpy)$_2$(NCS)$_2$**, abbreviated OsN3, is the osmium analogue of RuN3. It was first used by Nate Lewis's group but provided poor performance compared to RuN3 when used in DSSCs with an I^-/I_3^- redox shuttle.[37] OsN3 has a narrower optical bandgap. 1.30 eV, than RuN3

and absorbs well into the near-infrared region. OsN3 is the most extensively characterized dye in this thesis.

[Os(dcbpy)$_2$ppy](PF$_6$) (ppy is an abbreviation for a cyclometalated 2-phenylpyridine ligand attached through the 1-N and 2'-C positions), abbreviated Osppy, has an optical pseudo-bandgap of 1.25 eV. It was first used by Ardo Group Postdoc Hsiang-Yun Chen based on work done by Berlinguette'g group.[38,39] Osppy was originally used as a narrower pseudo-bandgap dye than OsN3 but was later replaced by $OsCl_2$ which had an even narrower pseudo-bandgap, easier synthesis, simpler spectra, greater stability, and greater structural similarity to other dyes.

***cis*-Os(dcpby)$_2$I$_2$**, abbreviated OsI_2, was originally synthesized by me based on its ruthenium analogue which was synthesized by the Gratzel group[40] and has an optical pseudo bandgap of 1.14 eV. This dye was expected to be very stable in the presence of I^-/I_3^- redox shuttle.

***cis*-Os(dcbpy)$_2$Cl$_2$** abbreviated $OsCl_2$, was originally synthesized by the Nate Lewis group as a precursor to OsN3,[37,41] however, to the best of my knowledge, they never used $OsCl_2$ as a DSSC dye. I chose to use it based on its ruthenium analogue synthesized by Michael Gratzel's group.[36,40] $OsCl_2$ was originally expected to be less stable and have a wider pseudo bandgap than OsI_2. These were not observed to be the case as $OsCl_2$ has an optical bandgap of 1.06 eV.

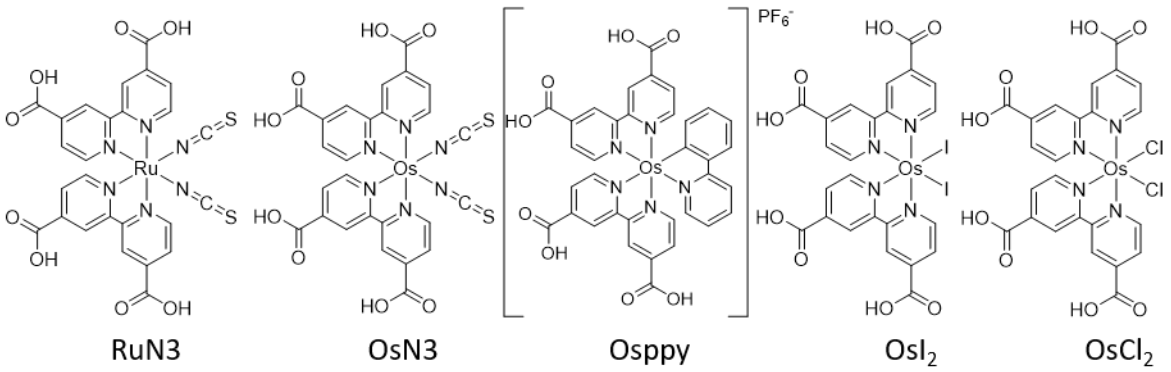

Figure 7: Chemical structures of the five dyes used in this thesis with abbreviations listed under each structure.

Results and Discussion

One of the most important properties of a dye is its absorption spectrum. The absorption spectrum determines the amount of sunlight that a dye can harvest, defines amount of dye necessary in a solar cell device, and can be used to extract an optical pseudo-bandgap of the material. We observed that our dyes were solvochramatic with absorption peaks shifting based on the solvent, the supporting electrolyte, and the surface that the dyes were bound to. To obtain spectra that accurately represented dyes in a working environment, absorption spectra were taken of dyes bound to TiO_2 films immersed in 100 mM $LiClO_4$ in acetonitrile. Baselined, normalized dye spectra are shown in **Figure 8**.

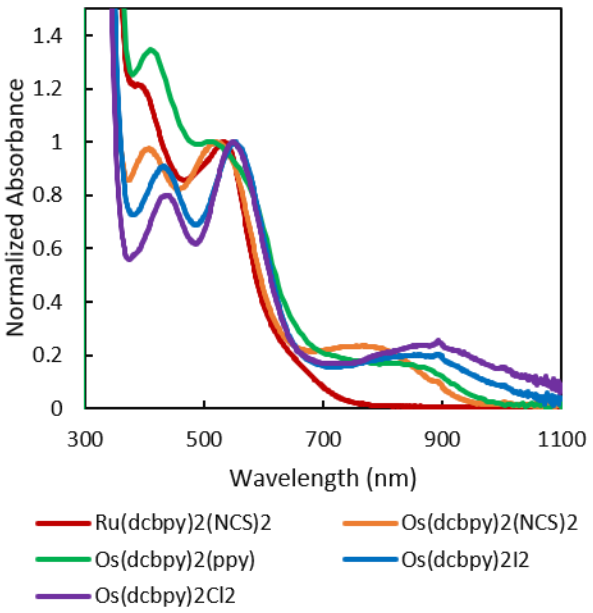

Figure 8: UV-vis electronic absorption spectra of dyes. Maroon: RuN3. Orange: OsN3. Green: Osppy. Blue: OsI_2. Purple: $OsCl_2$.

All dyes show two strong broad absorption peaks with the first peak at 350-450 nm and the second peak at 450-600 nm characteristic of singlet metal to ligand charge transfer.[42] Osmium dyes also show a weaker broad absorption peak at 700-1100 nm characteristic of triplet metal to ligand charge transfer.[43] Typically direct triplet excitation a is spin forbidden process, however, osmium has very large atomic nucleus (Z = 76) and many electrons so the process is significantly allowed. RuN3 also shows a tiny, but non-zero absorption in this region which may be a less favored triplet excitation, due to ruthenium smaller atomic number (Z = 44), or direct metal to TiO_2 excitation. In either case, the absorption feature is small enough to be considered not part of RuN3's absorption spectra for calculation purposes. All five dyes absorb strongly over the entire visible region and all osmium dyes absorb into the near infrared region.

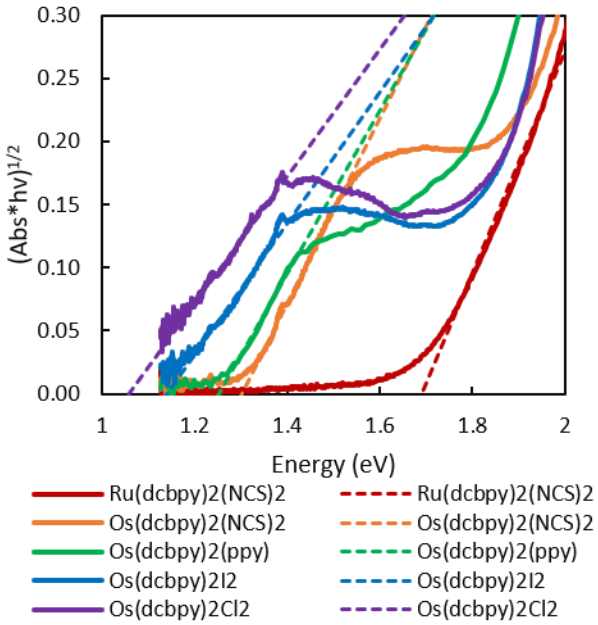

Figure 9: Tauc style plot of the square root of dye absorbance times the photon energy as a function of photon energy. Solid lines are dye Tauc spectra and dashed lines are linear fits of the absorption edge used to determine the optical pseudo-bandgap. Maroon: RuN3. Orange: OsN3. Green: Osppy. Blue: OsI_2. Purple: $OsCl_2$.

Figure 9 shows a Tauc style plot of the square root of the absorbance times the photon energy as a function of photon energy.[44] This analysis models dyes as semiconductors with direct allowed bandgap transitions.[45] While the validity of this method is debated, the results are more precise than merely measuring the optical bandgap by eye. The optical pseudo-bandgap can be determined by fitting the linear portion of the low energy absorption edge to a line and finding where the line intercepts the energy axis. From these measurements the optical pseudo-bangaps of RuN3, OsN3, Osppy, OsI_2, and $OsCl_2$ were determined to be 1.69, 1.30, 1.25, 1.14, and 1.06 eV respectively.

Another important set of parameters are the dye ground state and excited state energy levels. The ground state energy level can be estimated to be the ground state formal reduction potential and the excited state energy level can then be estimated by adding the optical pseudo-bandgap to the ground state energy level.[37]

The ground state formal reduction potential can be determined by cyclic voltammetry by finding the potentials of the forward and reverse peaks and averaging them.[46] It is possible to directly perform this measurement on dyes bound to films because charges transfer from dye to dye via a "hole hopping" mechanism discussed in more detail later. Ideally the peak-to-peak separation would be $2.22\frac{RT}{nF} \approx 57\,mV$ for a one-electron process like our dyes have. Dyes bound to mesoporous TiO_2 films exhibited much larger peak-to-peak separation than would be expected for reasons discussed in detail later. An example cyclic voltammogram of Osppy is shown in **Figure 10**. The greater than expected peak-to-peak separation originates largely from non-ideal Nernstian behavior and can be remedied by addition of a non-ideality factor such peak to peak separation is $2.22\frac{\alpha RT}{nF}$. Another source of peak to peak separation is non-zero electrochemical cell resistance.

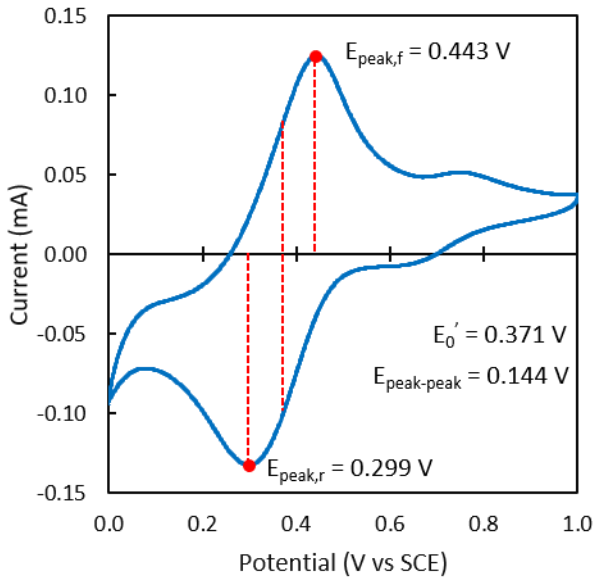

Figure 10: Cyclic voltammogram of Osppy bound to mesoporous TiO_2 on an FTO electrode in 100 mM $LiClO_4$ solution in acetonitrile. Forward and reverse peak potentials, peak-to-peak separation, and formal potential are labeled.

A more precise method of measuring potential is by stepwise chronoamperometry while probing UV-vis absorption. It is possible for the ratio of oxidized to reduced dye on films to fully equilibrate within a few minutes after each potential step because films are thin, ~ 5 um thick. The ratio of oxidized to reduced dye can then be determined by UV-vis spectroscopy. This technique is steady state and avoids non-ideal behavior due transient phenomena such as IR drop and capacitive charging. I performed stepwise chronoamperometry on mesoporous TiO_2 films dyed with OsN3, OsI_2, and $OsCl_2$ on FTO glass slides in 100 mM $LiClO_4$ solution in acetonitrile while probing in the UV, visible, and near-IR regions. After each potential step, kinetics at the peak triplet metal-to-ligand charge transfer absorption band were observed until there was no significant change, indicating that the film had reached equilibrium at the applied potential. The absorbance over the range of 200 to 1100 nm was measured and the next step started. Example results of these experiments are shown in **Figure 11**.

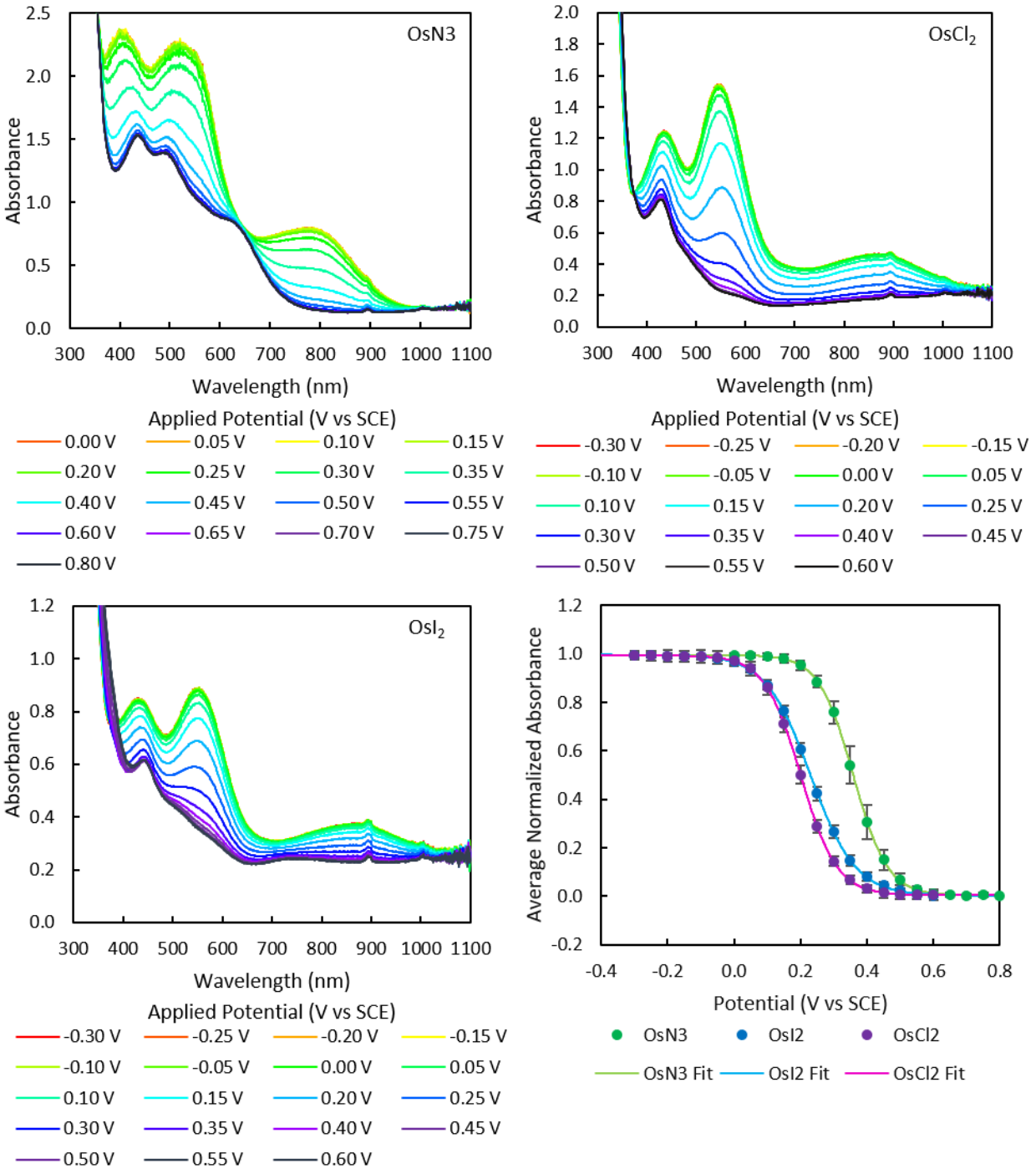

Figure 11: Upper left, upper right, lower left: UV-vis spectra of OsN3, $OsCl_2$, and OsI_2 dyes on mesoporous TiO2 on an FTO glass electrode in LiClO4 100 mM acetonitrile solution at various applied potentials versus SCE. Lower right: Average normalized absorbance of OsN3, OsI_2, and $OsCl_2$ spectra as a function of potential. Colored points are data and lines are Boltzmann sigmoid equation fits. Error bars indicate one standard deviation.

The potential step experimental results shown in **Figure 11** track the UV-vis absorption spectrum of each dyed film as a function of potential. The absorption changes are typical of a transition from a film where the dyes are in the reduced Os^{II} state to a film where the dyes are in the oxidized Os^{III} state. The metal to ligand charge transfer absorption bands of the oxidized dyes are reduced in intensity and often blue shifted relative to the corresponding bands in the reduced dyes.

The absorption at each wavelength at a given potential can be normalized to the maximum and minimum absorption at that wavelength over all measured potentials. By averaging all normalized wavelengths measured at each potential step, a sigmoid form emerges that fits the modified normalized Nernst-Beers-Boltzmann sigmoid equation (**Equation 1**) which has the functional form of the Boltzmann sigmoid equation (**Equation 2**) discussed in greater detail later. Fitting the observed sigmoid data with these equations yields the formal reduction potential, E_0', and the Nernst non-ideality factor, α for that dye. Dye formal potentials, non-ideality factors, optical pseudo-bandgaps, estimated excited state energy levels, and absorption edges are compiled in

Table 1. Values for TiO_2 are included for comparison.

Equation 1: Modified Normalized Nernst-Beers-Boltzmann Sigmoid Equation

$$\frac{Abs - Abs_{ox}}{Abs_{red} - Abs_{ox}} = \frac{1}{1 + e^{\frac{nF}{\alpha RT}(E - E_0')}}$$

Equation 2: Boltzmann Sigmoid Equation

$$y = A_2 + \frac{A_1 - A_2}{1 - e^{\frac{x - x_0}{dx}}}$$

Table 1: Basic electrochemical and optical parameters of dyes and TiO_2

	E_0' (V vs SCE)	α	$E_{0\text{-}0}$ (eV)	E_o'* (V vs SCE)	Absorption Edge (nm)
TiO_2	2.4[a]		3.2[a]	-0.8[a]	390[a]
RuN3	0.7-0.8[b]		1.69	-0.9[a]	740
OsN3	0.325	2.22	1.30	-0.97	960
Osppy	0.37[c]	2.53[c]	1.25	-0.88	990
OsI_2	0.23	2.67	1.14	-0.91	1130
$OsCl_2$	0.20	2.15	1.06	-0.86	1240

[a] literature value reported by Gratzel's[35] group. [b] literature value commonly reported.[47] [c] value determined by cyclic voltammetry.

One general trend in dye parameters was that decreasing formal reduction potential was concurrent with decreasing optical pseudo-bandgap so even though ground state potentials varied by 0.6 V, excited state energy levels varied by only ~0.1 V. All dyes had excited state potentials that were sufficiently negative to inject into the conduction band of TiO_2, a necessary feature for use in DSSCs with a TiO_2 support. The overpotential for injection was < 0.2 V for all dyes which is sufficient to inject, but not wasteful of energy.

DSSCs composed of RuN3, OsN3, Osppy, OsI_2, or $OsCl_2$ dyes bound to mesoporous TiO_2 films on FTO glass as the anode, platinized FTO as the cathode, and Nate Lewis style I^-/I_3^- redox containing 0.46 M LiI, 0.04 M LiI_3, 0.02 M trifluoroacetic acid, and 0.07 M 4-*tert*-butylpyridine in 85:15 v/v acetonitrile:valeronitrile solution were fabricated and tested for performance. The results of which are compiled in **Table 2**.

Table 2: DSSC performance parameters of cells using the I^-/I_3^- redox shuttle

	n	E_{OC} (V)	J_{SC} (mA cm^{-2})	Fill Factor	η (%)
TiO_2	3	0.38	0.051	0.41	0.008
RuN3	3	0.58	15	0.57	4.9
OsN3	1	0.21	0.63	0.43	0.057
Osppy	2	0.23	0.58	0.41	0.072
OsI_2	3	0.07	0.18	0.32	0.004
$OsCl_2$	3	0.20	0.087	0.57	0.010

The positive control cell using RuN3 dye showed good performance with a total energy conversion efficiency of 4.9%. This is less than the reported literature performance due simplified construction methods which did not minimizing cell resistance, use a light scattering layer, include a protective compact TiO_2 layer on the anode, nor use a reflective back contact. Cells using OsN3 and Osppy dyes performed significantly better than undyed cells, but significantly worse than RuN3 despite absorbing a greater portion of the visible spectrum. Cells using $OsCl_2$ barely outperformed undyed cells and cells dyed OsI_2 underperformed undyed cells. This was disappointing, but not entirely unexpected given the performance of previously synthesized infrared absorbing dyes.[34,48,49]

Conclusion

I purchased, obtained, or synthesized five metal polypyridyl dyes for use in dye sensitized solar cells. One, RuN3, is well known and will be used a positive control but does not significantly absorb infrared light. The other four dyes, OsN3, Osppy, OsI_2, and $OsCl_2$, absorb substantial amounts of near-infrared light. These dyes were characterized by UV-vis absorption spectroscopy, spectroelectrochemistry, and cyclic voltammetry. The ground state formal reduction potential of the dyes vary from 0.8 to 0.2 V vs SCE with optical pseudo-bandgaps that vary from 1.06 to 1.69 eV and excited state energy levels that vary from -0.86 to -0.97 V vs SCE.

All ground state standard reduction potentials are thermodynamically sufficient to oxidize I^- to I_3^- and all excited state energy levels are optimally aligned for injection into TiO_2.

Procedures

List of Reagents

For the synthesis of TiO_2 nanoparticles, the following reagents were used: ethyl cellulose (7 – 15 mPa·s, 6% in toluene/ethanol 80:20 (25 °C), 48.0 – 49.5%, w/w ethyloxyl basis, Sigma), ethyl cellulose (30 – 70 mPa·s, 5% in toluene/ethanol 80:20 (25 °C), 48.0 – 49.5%, w/w ethyloxyl basis, Sigma), ethanol (200 proof, Rossville Gold Shield USP), glacial acetic acid (GR* ACS 99.7%, EMD), titanium (IV) isopropoxide (98%+, Acros Organics), nitric acid (AR* ACS 68.0 – 70.0%, Macron Fine Chemicals), and terpineol (mixture of isomers, anhydrous, Aldrich).

For the synthesis of dyes, the following reagents were used: sodium hexachloroosmate dihydrate (99.9%, Alfa Aesar), 4,4'-dicarboxy-2,2'-bipyridine (DyeSol), sodium thiocyanate (ACS reagent ≥ 98.0%, Sigma Aldrich), sodium hydroxide (pellet AR* ACS, Macron), sodium hydrosulfite (technical grade, Sigma Aldrich), sodium iodide (99+%, Alpha Aesar), hydroiodic acid (ACS, 55-58%, Alfa Aesar), 1,3-cyclohexadiene (96%, stabilized with 0.1% BHT, Alfa Aesar), tetrabutylammonium hexafluorophosphate (TCI), 2-phenylpyridine (98%, Alfa Aesar), methylene chloride (certified ACS, stabilized, Fisher), and silica gel (230-400 mesh, Grade 60, Fisher).

Synthesis of cis-Os(dcbpy)$_2$Cl$_2$.[37]

A mixture of sodium hexachloroosmate dihydrate (0.4042 g, 0.833 mmol), 2,2'-bipyridine-4,4'-dicarboxylic acid (dcbpy, 0.3961 g, 1.622 mmol), and ethylene glycol (10 ml) were added round bottom flask fitted with a reflux condenser. The osmium compound, which is initially a red solid, dissolves to form a green solution. The flask was evacuated, and the atmosphere replaced with nitrogen three times while stirring. The first evacuation was held until yellow-green bubbles were no longer observed. Under a blanket of nitrogen, the mixture was refluxed for 2 h. The solution changes color to a deep purple. After cooling to room temperature, sodium hydrosulfite (0.2 g) dissolved in water (90 ml) were added to reduce osmium to Os^{II} and precipitate the product as a deep purple black solid which was collected by filtration, rinsed with cold water and ether, and dried under vacuum. Yield: 0.5621 g (0.7499 mmol, 90% yield). ^{1}H NMR (500 MHz, NaOD/D_2O) δ 9.56 (d, *J* = 6.0 Hz, 2H), 8.82 (d, *J* = 1.8 Hz, 2H), 8.60 (d, *J* = 1.8 Hz, 2H), 7.91 (dd, *J* = 6.1, 1.8 Hz, 2H), 7.58 (d, *J* = 6.2 Hz, 2H), 7.11 (dd, *J* = 6.2, 1.8 Hz, 2H); D_2O peak was used as the internal standard at 4.79 ppm.

Synthesis of cis-Os(dcbpy)$_2$(NCS)$_2$.

The synthesis followed the published procedures with some modifications to improve product purity.[36,37] mixture of *cis*-Os(dcbpy)$_2$Cl$_2$ (158 mg, 0.211 mmol), sodium thiocyanate (1.00 g, 12.3 mmol), and an aqueous solution of sodium hydroxide (62 mM, 10 ml) was sparged with nitrogen. Under a blanket of nitrogen, the solution was refluxed for 5 h and cooled to room temperature. At this stage, NMR indicates that the crude product contains a mixture of sulfur- and nitrogen-coordinated NCS^- ligands with a ratio of 55:45.[37] To improve the purity, *N*,*N*-dimethylformamide (10 ml) was added to the reaction, sparged with nitrogen and refluxed for 11 h.[36] After cooling to room temperature, the reaction mixture was added to an aqueous solution of

hydrochloric acid (10% v/v, 50 ml) and stored in a freezer for 1 h to allow precipitation. The mixture was filtered through Celite. The filtrate was discarded and the solid was rinsed with an aqueous solution of hydrochloric acid (~1%), water, and diethyl ether, and was collected by dissolving in methanol. The methanol solution was concentrated with a rotary evaporator and the remaining solvent was removed by extracting with diethyl ether and hexanes. The remaining powder was evacuated overnight. ^{1}H NMR (499 MHz, NaOD/D_2O) δ 9.36 (d, *J* = 6.0 Hz, 2H), 8.84 (d, *J* = 1.8 Hz, 2H), 8.66 (d, *J* = 1.8 Hz, 2H), 8.00 (dd, *J* = 5.9, 1.8 Hz, 2H), 7.64 (d, *J* = 6.0 Hz, 2H), 7.28 (dd, *J* = 6.1, 1.8 Hz, 2H); D_2O peak was used as the internal standard at 4.79 ppm.

Synthesis of cis-Os(dcbpy)$_2$I$_2$

cis-Os(dcbpy)$_2$Cl$_2$ (167 mg, 0.223 mmol), NaI (738 mg, 4.93 mmol), and ethylene glycol (5 ml) were added to a flask equipped with a water condenser. The flask was evacuated, and the atmosphere replaced with nitrogen three times while stirring. Under a blanket of nitrogen, the mixture was refluxed for 2 h and allowed to cool to room temperature. Water (25 ml) and HI (0.5 ml) was added to precipitate the product as a purple black solid which was collected by filtration and dried under vacuum. Yield: 0.1461 g (0.167 mmol, 70.5% yield). ^{1}H NMR (499 MHz CD_3OD) δ 10.38 (d, *J* = 45.7 Hz, 2H), 9.10 (dd, *J* = 40.8, 24.4 Hz, 2H), 8.96 (d, *J* = 22.9 Hz, 2H), 7.97 (d, *J* = 25.5 Hz, 2H), 7.43 (m, 4H). Splitting may be exaggerated by the presence of oxidized species.

Synthesis of [Os(dcbpy)$_2$(ppy)](PF$_6$).

Sodium hexachloroosmate dihydrate (218 mg, 0.448 mmol), 1,3-cyclohexadiene (0.6 ml, 0.505 g, 6.30 mmol), and ethanol (2 ml) were refluxed under nitrogen for 3 days. Additional ethanol was added periodically to maintain a total volume of 2.6 ml. While refluxing the mixture went from deep green to light green. The mixture was cooled overnight in a freezer to precipitate

the product which was collected by vacuum filtration, washed twice with ice-cold ethanol (0.5 ml each) and once with diethyl ether (0.5 ml), and dried under vacuum. The product, $[OsCl_2(C_6H_6)]_2$ was a pale green solid which was used immediately in the next step without further purification. The solid was expected to be yellow, but was most likely contaminated with some of the green starting material.[39]

$[OsCl_2(C_6H_6)]_2$, NaOH (17.6 mg, 0.44 mmol), tetra-n-butylammonium hexafluorophosphate (345 mg, 0.891 mmol), 2-phenylpyridine (72.1 mg, 0.465 mmol), and acetonitrile (22.8 ml) were stirred at 40 °C under nitrogen for 48 hours. Over the course of the reaction, the mixture went from a pea-soup green to clear yellow mixture blue precipitate. The solvent was evaporated under vacuum. The product was dissolved in dichloromethane (30 ml) and loaded onto a column of alumina (20 ml). The product was then eluted with dichloromethane (20 ml) followed by 1:9 acetonitrile:dichloromethane (50 ml) and collected in 10 fraction of 10 ml. The first five fractions contained a red impurity which was discarded. The final three fractions contained the yellow product $[Os(C_6H_6)(ppy)(CH_3CN)](PF_6)$ which was isolated by removal of solvent under vacuum. Yield:124 mg (0.204 mmol, 55% yield over two steps).

$[Os(C_6H_6)(ppy)(CH_3CN)](PF_6)$ (124 mg, 0.204 mmol), 4,4’-dicarboxy-2,2’-bipyridine (101 mg, 0.412 mmol), and methanol (13 ml) were refluxed under nitrogen for 48 hours. The initially yellow solution slowly turned a deep purple black color during the course of the reaction. The reaction was cooled and the solvent removed by vacuum. The resulting solid was purified using a column of silica gel (16 ml) and 1:99 trifluoroacetic acid:dichloromethane eluent (100 ml). An initial green band containing impurity eluted first followed by a broad purple band containing pure $[Os(dcbpy)_2(ppy)](PF_6)$. Solvent was removed by vacuum. Yield: 60.7 mg (0.062 mmol, 30% yield).

Synthesis and Preparation of TiO_2 Nanocrystallite Paste

TiO_2 paste was prepared according to a modified literature procedure.[35] Ethyl cellulose 7 – 15 mPa·s (0.45 g), ethyl cellulose 30 – 70 mPa·s (0.35 g), and ethanol (7.2 g) were added to a flask and were set aside to stir for at least 12 h. Glacial acetic acid (1.2 g, 20.0 mmol) was added to stirring titanium(IV) isopropoxide (5.86 g, 20.6 mmol) with release of heat. The mixture was stirred for 15 minutes and allowed to cool to room temperature. The mixture was poured into rapidly stirring water (29 ml) and stirred for another 60 minutes. A translucent white slurry formed, which broke up during the stirring period. Concentrated nitric acid (0.4 ml, 8.5 mmol) was added and the temperature slowly raised to 80 °C where it was held for 75 minutes while stirring. The mixture was allowed to cool to room temperature, transferred to a Teflon liner, and water was added until the total volume equaled 37 ml. The Teflon liner and its contents were placed in a steel pressure vessel, which was placed in a box/muffle furnace. The furnace was heated at a rate of 8 °C per minutes to a final temperature of 220 °C where it was held for 12 h and then allowed to cool to room temperature. The white TiO_2 nanoparticle pellet was homogenized with the surrounding aqueous solution using an ultrasonic horn. The solution was then removed by rotary evaporator until the remaining mass equaled 12.7 g. It was then centrifuged, the supernatant removed and replaced by ethanol, and the mixture homogenized by sonication. This step was repeated three times. On the third time, ethanol was added such that the final solution weighed 4.1 g. Terpineol (6.49 g) and the previously prepared ethyl cellulose solution were added. The mixture was alternately stirred and sonicated with the ultrasonic horn until homogenized. The mixture was placed on a rotary evaporator and 17.6 g of liquid removed, mostly ethanol, to make a thick paste which was used to prepare TiO_2 thin films. Particles were expected to be anatase TiO_2 with ~15 nm diameter, as reported previously.[50]

DSSC fabrication

Two 2 cm × 3 cm fluorine-doped tin oxide (FTO) glass slides (TEC15, 2.2 mm thickness, GreatCell Solar Limited) were cut. To one slide, the counter electrode or cathode, two holes were drilled using a 1 mm round diamond grinding drill bit and a drill press. Both glass slides were sonicated in 5-10% wt aqueous Alconox solution (powdered precision cleaner, Alconox, Inc.) with the conductive side facing upwards for 15 minutes, rinsed with water and ethanol (200 proof Rossvillle Gold Shield USP), sonicated conductive side face up in ethanol for 15 minutes, and rinsed with ethanol. The slides were allowed to dry in air and then heated on an aluminum foil covered hotplate set to 550 °C (but probably not actually 550 °C) for 1 hour. The slides were allowed to cool on the inactive hotplate for 1 hour until they reached room temperature. TiO_2 paste was applied to a ~7 mm wide area of the working electrode, or anode, using the doctor blade method with Scotch Magic Tape spacer. 5 drops of 2 mM hexachloroplatinic acid hydrate (99.9% trace metals basis, Aldrich) were applied to the conductive side of the counter electrode, allowing each drop to dry before the next was applied. Both slides were placed in a box muffle furnace. The temperature was raised at a rate of 3 °C per minutes to 90 °C, held at 90 °C for 1 h, raised at a rate of 3 °C per minutes to 500 °C, held at 500 °C for 1 h, and then allowed to cool to room temperature without disturbing the furnace door. TiO_2 was removed from both sides of the working electrode to make a 7 mm square using a Teflon-coated razor blade. The working electrode was immersed in 0.04 M titanium (IV) chloride solution (prepared from adding titanium (IV) chloride (99%, Strem Chemicals, Inc.) dropwise to water at 0 °C with rapid stirring) in a covered glass petri dish and heated at 70 °C on a hot plate (set to 120 °C, but the temperature setting isn't accurate) for 40 minutes and allowed to cool to room temperature. The

working electrode was rinsed with water and allowed to dry in air at room temperature. It is re-sintered using the same temperature cycle as before. The thin film was then base-pretreated for 15 minutes in a pH 11 LiOH aqueous solution and then placed in acetonitrile for 15 minutes to remove excess water. It is then placed in a 2 mM dye solution in 1:1 v/v acetonitrile:methanol solution for at least 24 hours. Dyed slides were soaked twice for 15 minutes each in acetonitrile to remove weakly bound dyes and then allowed to dry. A rectangular Surlyn window gasket (20 mm × 20 mm outer dimensions, 10 mm × 10 mm inner dimensions, Dysol 30 μm Surlyn Thermoplasic Sealant) was placed on the dyed slide around the dyed area so that only exposed FTO was covered. The counter electrode was placed with its conductive side facing inwards, the holes were on opposite corners of the TiO_2 film, and both slides have an overhanging edge. all components were secured by a pair of 0.5” binder clips. The assembly was placed into a preheated muffle furnace at 120 °C for 10 minutes to allow the Surlyn gasket to melt and seal the cell. The cells were allowed to cool for 10 minutes before removing the binder clips. Electrolyte solution was introduced via glass pipette into one of the two drilled holes. The two holes were plugged with parafilm, cleaned with a kimwipe, painted with a thin layer of UV-curable clear gel nail polish (Lina UV topcoat), and capped with microscope glass coverslips (3 mm × 3 mm, Fisherbrand Microscope Cover Glass #1). The nail polish was cured under UV light (HWAWTS Ultrafire) for thirty seconds. Electrochemical measurements were performed the same day with the exception of SPEIS measurements which were performed the next day.

Preparation of Slides for UV-vis, Staircase Potential Step Spectroelectrochemistry, and Cyclic Voltammetry

Preparation of these slides was performed similarly to the dyed electrodes in DSSCs except the FTO glass slide dimensions were 7.0 cm × 0.7 cm, the FTO was applied only to the lower portion of the slide in a 0.7 cm × 0.7 cm square, and films were immediately base pretreated and dyed after the first sintering process without treatment with $TiCl_4$ solution.

Spectroelectrochemical Setup

Three-electrode electrochemical measurements were performed using a Bio-Logic VSP-300 potentiostat in grounded mode using a dyed TiO_2 working electrode, an aqueous KCl-saturated calomel electrode reference electrode, and a platinum mesh counter electrode. The three electrodes, a magnetic stir bar, and 14 ml of supporting electrolyte were assembled into a 1 cm × 1 cm custom borosilicate glass spectroelectrochemical cuvette with a 20 ml solvent bulb and 24/40 female joint capped with a rubber septum with holes drilled in it for wire leads that was placed in an Agilent Cary 60 Electronic Absorption Spectrophotometer. The cell was sealed and purged with argon gas for 30 minutes prior to measurement. Stirring and argon bubbling continued during all electrochemical experiments.

UV-vis

Before doing spectroscopy, the instrument was set to *zero/baseline correction* and a dark measurement was collected by blocking the sample beam as close to the source as possible. A blank measurement was collected through air. The slide was aligned so that the dyed TiO_2 film was facing the measurement beam and the beam fully passed through the solar cell. An

absorption spectrum from 1100 to 200 nm wavelength was taken with a scan rate of 600 nm min^{-1}.

Cyclic Voltammetry

The working electrode was places as close as possible, ~3 mm, to the reference electrode frit. An initial open-circuit potential measurement was performed for 30 sec to ensure that the cell was set-up correctly. This was followed by cyclic voltammetry measurements with the scan limits displayed and a scan rate of 0.1 V/s, performing three scans at each scan rate.

Staircase Potential Step Spectroelectrochemistry

Potential steps were applied over the displayed voltage range in increments of 0.05 V. After each potential step is applied, the absorbance at the peak absorption value for the direct triplet excitation mlCT band was observed until no additional change could be seen, usually 3 to 10 minutes after the potential step was applied. A full spectrum scan was then taken from 200 nm to 1100 nm before the next potential step was applied.

NMR

NMR experiments were performed on a Bruker DRX500 spectrometer with a BBO probe.

MALDI

MALDI experiments were performed using an AB SCIEX TOF/TOF 5800 System. MALDI samples were prepared by using 0.03 ml of a 5 mM methanol solution of the osmium complex (if solubility allows), 12.5 mg 2,5-dihydroxybenzoic acid, and 0.25 ml acetonitrile of

which 1 pl was spotted onto the MALDI target. Mass spectra were obtained in positive reflector mode.

Reconciliation of Differences in Measured Self-Exchange Electron-Transfer Rate Constants between Dye Molecules Anchored to Mesoporous Titanium Dioxide Thin Films

Introduction

Wide bandgap semiconductors with surface-anchored dyes are used in solar cells to produce electricity from light absorption,[1,33,34] in solar fuels constructs to store energy from light as chemical energy,[51] and in photoelectrochromic devices to alter light transmittance.[52] In order to most effectively absorb light while maintaining a thin device thickness, large concentrations of dyes are used, necessitating that the semiconductor substrate consist of a high-surface-area porous film. This often results in a volumetric concentration of ~1 M dyes, which throughout typical micron-thick films, forms a bulk chemical pseudocapacitor that can store and release fixed amounts of charge. Molecules bound to these mesoporous semiconducting surfaces exist in a very different environment than molecules dissolved in solution. This impacts the thermodynamic and kinetic properties of the molecules and often makes standard electrochemical analyses inaccurate. For example, when neighboring molecules interact, are bound to a distribution of binding sites, and/or exist within the double layer of an electrode, assumptions used to derive fundamental electrochemical equations, such as the Nernst equation, are less valid than for molecules dissolved in solution.[53–58] In addition, the mechanism of electron transfer between the vast majority of molecules is different. For solution species, individual molecules are physically transported to the electrode surface by diffusion migration,

convection, etc., undergo electron transfer, and then physically transport away from the electrode. For species bound to a porous wide-bandgap or insulating scaffold in intimate contact with the electrode, molecules do not diffuse and only a few molecules are close enough to the electrode surface to undergo interfacial electron transfer. Notwithstanding, net redox reactions with species far from the electrode interface can occur via a series of self-exchange electron-transfer "hopping" transport reactions that originate at molecules close to the electrode surface. This requires that molecules are adequately concentrated so that the distance of self-exchange electron transfer is small and a percolation network of dyes exists, typically > 50% of maximum surface coverage.[59–61]

This interfacial self-exchange electron-transfer process can be either beneficial or detrimental depending on the application. Some benefits include the ability to increase charge collection efficiency in solid-state dye-sensitized solar cells,[62] accumulate charge on electrocatalysts to allow effective multiple-electron-transfer reactions,[50,63–66] and rapid electrochromic behavior upon application of a sufficient bias potential and without additional electroactive components.[67] However, faster interfacial self-exchange electron transfer has also been shown to directly correlate with faster recombination rates in liquid-electrolyte dye-sensitized solar cells.[68–70]

Rates of interfacial self-exchange electron transfer between dyes anchored to mesoporous thin films have been measured using a variety of techniques including chronoamperometry,[61,71] chronoabsorptometry,[59,60,69,72–75] cyclic voltammetry,[62,76,77] impedance spectroscopy,[76] and transient absorption anisotropy measurements.[65] Of these methods, chronoamperometry, chronoabsorptometry, and cyclic voltammetry are most commonly used because the instrumentation needed, a potentiostat or source-meter and an ultraviolet–visible

spectrophotometer, are widely available and data interpretation is relatively simple. Each of these three methods yields an apparent diffusion coefficient, D_{app}, that is related to the self-exchange rate constant and ideally the same value is obtained regardless of the method used; however, this is not often observed in the literature. This is because analysis of data obtained by each method requires different assumptions and so care must be taken when calculating D_{app} values so that they are accurate, independent of the method used to measure them.

Herein, self-exchange electron-transfer rate constants recast as D_{app} values are determined using three common electrochemical techniques: chronoamperometry, chronoabsorptometry, and cyclic voltammetry. Initial differences in results are corrected based on assumptions and supporting measurements to unify protocols for measuring D_{app}. In these studies, we utilize the Os(II) version[37] of the well-known N3 dye[36] for two main reasons: (*i*) to use a dye that is extremely stable in its 3+ oxidation state on the timescale of hours so that accurate spectroelectrochemical characterization and analyses can be performed. (In comparison, the Ru(III) state of N3/N719 is only stable on the sub-seconds timescale.[78]) And (*ii*) to use a near-infrared-absorbing dye that is appropriate as a sensitizer in next-generation highly efficient dye-sensitized solar cells. Because its HOMO–LUMO energy gap is 1.1 – 1.4 eV, which is optimal based on the detailed-balance Shockley–Queisser power conversion efficiency limit under terrestrial solar illumination,[26,79] incorporation of this dye into iodine-based dye-sensitized solar cells can result in sunlight-to-electricity power-conversion efficiencies that exceed 20%. We used a mesoporous titanium dioxide thin film as the wide bandgap semiconductor substrate due to its ubiquitous use in dye-sensitized solar cells.

Results and Discussion

Steady-State Spectroelectrochemistry of Dyed Films

Stepwise chronoamperometry measurements were performed on mesoporous TiO_2 thin films dyed with OsN3, cast on fluorine-doped tin–oxide-coated glass (FTO) substrates (OsN3|TiO_2|FTO), and immersed in 100 mM acetonitrile electrolyte solution while probing in the 200 – 1100 nm spectral region. After each potential step, absorbance values were measured at 790 nm with averaging intervals of 0.1 s until there was no significant change in the signal, indicating that the film had approximately reached equilibrium at the applied potential. We then measured absorption spectra over the full range of applied potential biases, an example result of which is shown in **Figure 12**.

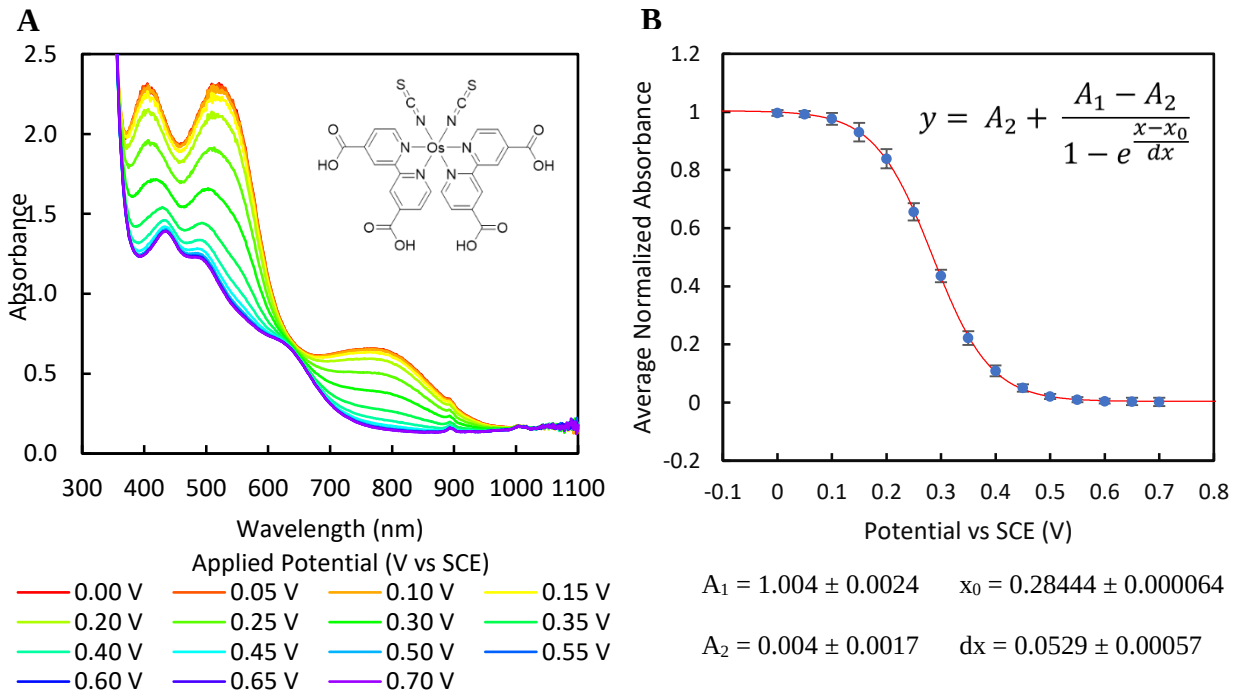

Figure 12: (A) Electronic absorption spectra of OsN3|TiO_2|FTO immersed in 100 mM $TBAClO_4$ acetonitrile solution at the indicated applied potentials versus SCE. The inset shows the chemical structure of OsN3. (B) Average normalized absorbance as a function of potential and best fits to the Boltzmann sigmoid equation and fitted parameters shown on the figure. Error bars indicate one standard deviation based on deviation between wavelengths.

Ultraviolet–visible electronic absorption spectra were consistent with the occurrence of a single redox process with almost all dyes bound to the thin film in the oxidized state at potentials more positive than 0.7 V *versus* SCE and in the reduced state at potentials negative of 0.0 V *versus* SCE. When the absorbance values at each wavelength were normalized to the corresponding values at 0.0 V and 0.7 V of applied potential bias, averaged across the full spectrum, and plotted as a function of applied potential, a sigmoid-shaped curve resulted (**Figure 12B**). The resulting sigmoid curves closely fit to the Boltzmann Sigmoid Equation (**Equation 3**).

(3) Boltzmann Sigmoid Equation

$$y = A_2 + \frac{A_1 - A_2}{1 - e^{\frac{x - x_0}{dx}}}$$

(4) Nernst-Beers-Boltzmann Sigmoid Equation

$$Abs = Abs_{ox} + \frac{Abs_{red} - Abs_{ox}}{1 + e^{\frac{nF}{RT}\left(E - E^{0\prime}\right)}}$$

(5) Normalized Nernst-Beers-Boltzmann Sigmoid Equation

$$\frac{Abs - Abs_{ox}}{Abs_{red} - Abs_{ox}} = \frac{1}{1 + e^{\frac{nF}{RT}\left(E - E^{0\prime}\right)}}$$

The Nernst Equation and the Beer–Lambert law can be combined to find the expected absorbance at a given potential of a fully equilibrated dyed film (**Equation 4**). This is identical in form to the Boltzmann Sigmoid Equation (**Equation 3**). To compare all wavelengths simultaneously, we normalize **Equation 4,** which yields **Equation 5.** The fitting parameters can then be translated to physically significant values: x_0 translates directly to the formal potential of the dye, $E^{o\prime}$. dx is expected to translate to $\frac{RT}{nF}$ which is ~26 mV for a one-electron process at room temperature. However, we consistently measured dx to be approximately twice the expected value, necessitating an additional fitting parameter, the non-ideality factor (α) to correct the stretch of the sigmoidal functon.[56] This led to the use of a modified fitting formula, **Equation 6.**

(6) Modified Normalized Nernst-Beers-Boltzmann Sigmoid Equation

$$\frac{Abs-Abs_{ox}}{Abs_{red}-Abs_{ox}} = \frac{1}{1+e^{\frac{nF}{\alpha RT}\left(E-E^{0\prime}\right)}}$$

The inclusion of α in **Equation 6** draws attention to the non-ideal Nernstian behavior of OsN3 bound to the surface of TiO_2. This can be described by modifying the Nernst Equation (**Equation 7)**. A table of measured parameters can be found in **Table 3**.

(7) Modified Nernst Equation

$$E = E^{0\prime} - \frac{\alpha RT}{nF} ln(Q)$$

Table 3: Measured formal potentials, E°', and ideality factors, α.

	E°' (V *vs* SCE)		α	
n	mean	σ	mean	σ
13	0.325	0.040	2.22	0.16

We have not identified the origin of α but there are several possible explanations. α could be considered as in increase in the effective temperature of the system. The surface of TiO_2 is not uniform and so the dyes do not all exist in equivalent chemical environments. This increased inhomogeneity could lead to a broadened redox response. Alternatively, the Nernst equation assumes that dissolved species are not in electronic contact with each other. On a dyed film, dyes separation distance is small enough such that each dye is impacted by the electric field generated by surrounding dyes. Thus, as dyes are oxidized, it would become more difficult to oxidize additional dyes, broadening the redox response to potential. Regardless of the physical mechanism, the ratio of reduced-to-oxidized dye, *Q*, is less responsive to changes in potential when bound to a mesoporous thin film than when dissolved in a liquid electrolyte solution.

Potential Step Chronoamperometry

Once we had identified that the oxidation and reduction of dyes bound to a mesoporous TiO_2 scaffold followed a modified Nernst behavior, we also wanted to identify whether self-

exchange electron transfer followed standard kinetic diffusion models. The Cottrell equation (**Equation** 8) describes the instantaneous electric current as a function of time of a planar electrode under mass transport diffusion control in a semi-infinite solution, after application of a potential step sufficiently large to completely oxidize or reduce all molecules at the surface. If self-exchange electron transfer of a dyed film follows standard diffusion kinetics, its current response should match the Cottrell equation.

(8) The Cottrell Equation

$$i = \frac{nFAC\sqrt{D}}{\sqrt{\pi t}}$$

Integrating the Cottrell equation yields the Anson equation (**Equation 9**), which is more commonly used to determine diffusion coefficients because it is less sensitive to non-Faradaic capacitive currents and the presence of electroactive surface-adsorbed species.

(9) The Anson Equation

$$q = \frac{2nFAC\sqrt{Dt}}{\sqrt{\pi}}$$

We applied alternating potential steps at 0.0 and 0.7 V versus SCE for five minutes each to fully reduce and oxidize the film while measuring current. The background current corresponding to oxidation or reduction of non-dye species was subtracted. The total current passed due to dye oxidation or reduction was plotted with respect to the square root of time (**Figure 13**). To extract the apparent diffusion coefficient we fit the linear portion of the resulting curve to the Anson equation, corresponding to the first 60% of current passed. After the first 60% of total current passed the curves stop exhibiting linear behavior because the assumption in the Cottrell model of infinite solution length fails when oxidized or reduced dyes begin to reach the edge of the ~5 μm thick film. The concentration, *C*, in the Anson equation was measured as the total charge passed during the entire potential step divided by the film volume.

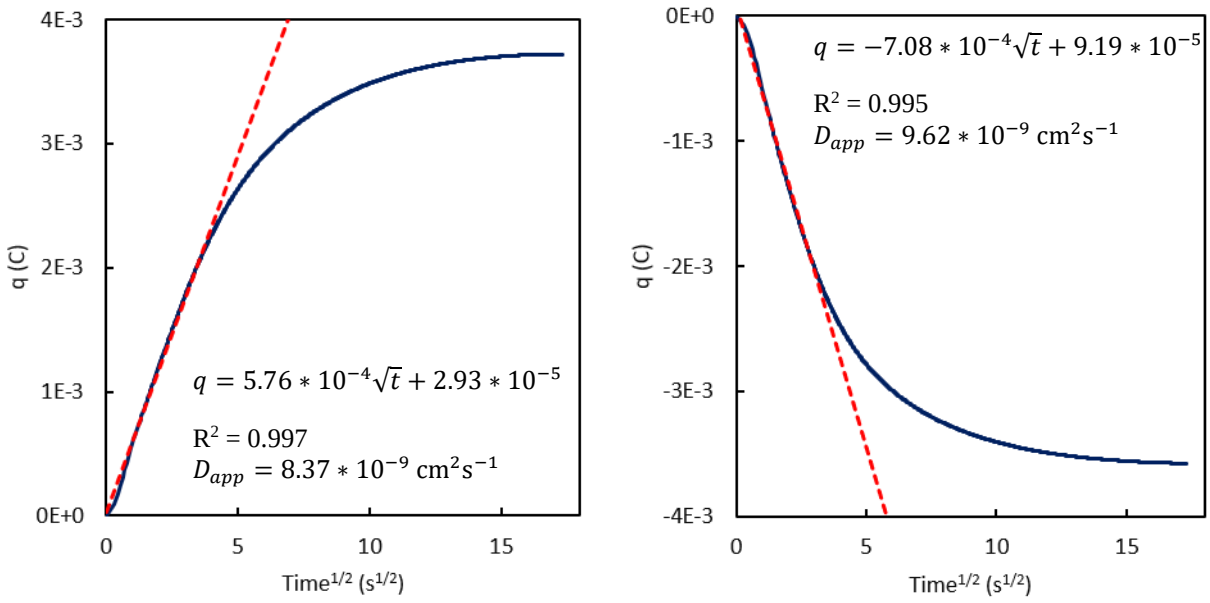

Figure 13: Net charge passed as a function of the square root of time for OsN3|TiO_2|FTO immersed in 100 mM $TBAClO_4$ acetonitrile solution (blue solid line), with best-fit equation (red dashed line), R^2, and extrapolated D_{app} shown, after a potential step to (a) 0.8 V versus SCE followed by (b) 0.0 V versus SCE.

At first glance it may seem that the D_{app} value calculated under anodic and cathodic conditions should be the same because the process of self-exchange electron transfer is the same in either situation. The average D_{app} values for oxidation and reduction processes were found to be the same, however, the values on a single film were often different with no repeatable trend for which was faster. **Table 4** contains a summary of the measured D_{app} values.

Table 4: D_{app} values determined by chronoamperometry.

	D_{app} (cm^2/s), Anodic Process		D_{app} (cm^2/s), Cathodic Process	
n	Mean	σ	mean	σ
22	1.16×10^{-8}	4.9×10^{-9}	1.16×10^{-8}	5.2×10^{-9}

Potential Step Chonoabsorptometry

Another method used to measure concentrations of oxidized and reduced dyes after a potential step is by measuring absorption at a single wavelength over time. This method avoids the errors in the measurement of current due to capacitive charging and side reactions. While performing the previously described chronoamperometry experiments we simultaneously probed

oxidized and reduced dye concentrations using electronic absorption spectroscopy. The Anson equation (**Equation 9**) can be modified using the Beer–Lambert law to **Equation 10**, which uses normalized change in absorbance instead of current to extract D_{app} values.

(10) Spectroelectrochemistry Variant Anson Equation

$$\frac{\mathrm{Abs}-Abs_{red}}{Abs_{ox}-Abs_{red}} = \frac{2\sqrt{Dt}}{d\sqrt{\pi}}$$

Similar to the chronoamperometry experiment, we graphed normalized absorption as a function of the square root of time and fit the linear portion of the resulting curve to extract the apparent diffusion coefficient (**Figure 14**). The linear portion was defined to be the first 60% of the absorption change, after which, a significant fraction of oxidized or reduced dyes were assumed to reach the edge of the film. A table of measured parameters can be found in

Table 5.

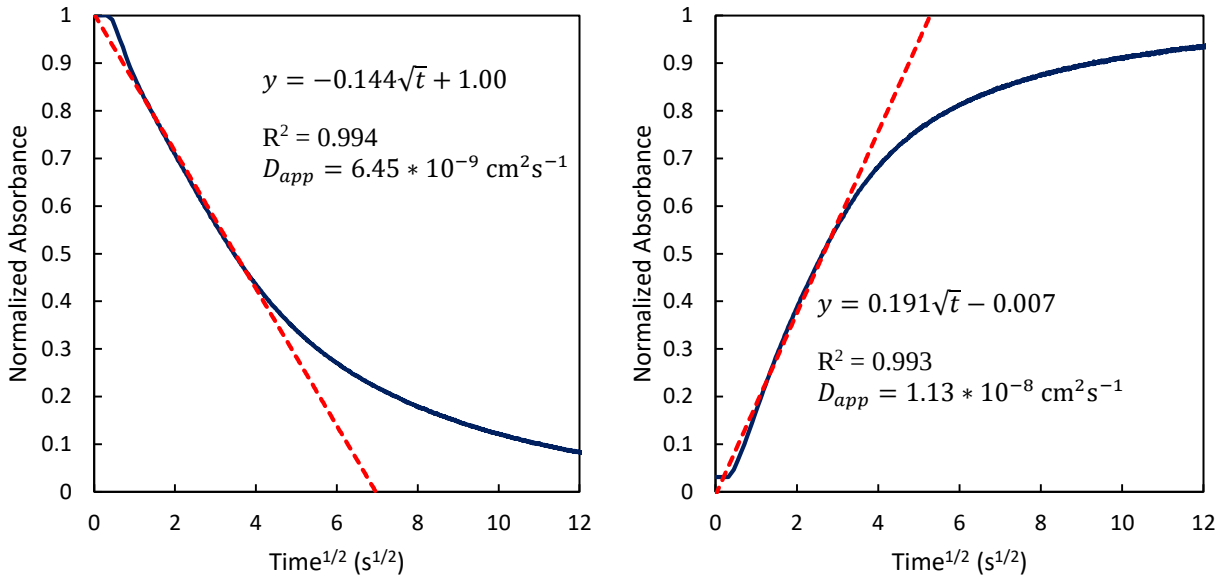

Figure 14: Normalized absorbance at 790 nm as a function of the square root of time for OsN3|TiO_2|FTO immersed in 100 mM $TBAClO_4$ acetonitrile solution (blue solid line), with best-fit equation (red dashed line), R^2, and extrapolated D_{app} shown, after a potential step to (a) 0.8 V versus SCE followed by (b) 0.0 V versus SCE.

Table 5: D_{app} values determined by spectroelectrochemistry.

	D_{app} (cm^2/s), Anodic Process		D_{app} (cm^2/s), Cathodic Process	
n	mean	σ	mean	σ
21	1.1×10^{-8}	0.6×10^{-8}	1.3×10^{-8}	0.6×10^{-8}

The D_{app} values measured using spectroelectrochemistry under anodic and cathodic conditions on a single film were often different, with no film-to-film trend to indicate which was larger. D_{app} values measured under cathodic conditions were, on average, slightly larger than D_{app} values measured under anodic conditions, however, these two values are within experimental error of each other.

The D_{app} values measured by chronoamperometry as the current over time were on average within experimental error of the D_{app} values measured simultaneously using electronic absorption spectroscopy. On a single film in a single measurement, the values were often different.

There are two differences in the assumptions made in our measurement of D_{app} using **Equation 9** and **Equation 10**. Using **Equation 9** we calculated the total amount of dye bound to the films, n_{CA}, as the total current passed, the average film thickness, $\bar{d}$, by profilometry, and the geometric film area, *A*, by image analysis. We used these three values to calculate the dye concentration, *C*. **Equation 10** eliminates the need for a separately measured dye concentration by use of normalized absorbance. However, normalization makes the equation dependent on the film thickness at the location of the probe beam, d_{spec}, which may vary slightly from the average thickness, $\bar{d}$, due to local inhomogeneity. Normalization ensures that only electrochemically active dyes are measured which is in agreement with our method of calculating the concentration of dyes using total current passed. D_{app} values measured by chronoamperometry and spectroelectrochemistry can be related to the difference in relevant thicknesses by **Equation 11.**

(11) Comparison of D_{app} values obtained by chronoamperometry and spectroelectrochemistry

$$\frac{D_{CA}}{D_{spec}} = \left(\frac{\bar{d}}{d_{spec}}\right)^2$$

Equation 11 provides a good explanation of how D_{app} values measured using chronoamperometry and spectroelectrochemistry could yield different results even when measured simultaneously. It also provides a rationale for why the average values would be the same. If the spectrometer probe beam randomly samples the films over many trials, d_{spec} will average to $\bar{d}$. Moving the films to probe several locations of the thin film and/or increasing the size of the probe beam are non-trivial and therefore, they were not performed.

Cyclic Voltammetry

A third method to determine diffusion coefficients uses cyclic voltammetry and values of the peak current as a function of scan rate using the Randles-Sevcik equation (**Equation 12**).

(12) Randles-Sevcik Equation

$$i_p = 0.4463nFAC\left(\frac{nFvD}{RT}\right)^{\frac{1}{2}}$$

The Randles-Sevcik equation is derived by solving the time-dependent concentration profile of an infinite solution using the diffusion equation with a linear potential sweep combined with the Nernst equation as the electrode boundary condition.[80] Dyes bound to mesoporous TiO_2 thin films obey a modified version of the Nernst Equation (**Equation 7**) which must be used to produce a modified Randles-Sevcik equation (**Equation 13**). The only difference between the two is the addition of the non-ideality factor, α. Failure to measure and include α will result in underestimation of D_{app} by a factor of α.

(13) Modified Randles-Sevcik Equation

$$i_p = 0.4463nFAC\left(\frac{nFvD}{\alpha RT}\right)^{\frac{1}{2}}$$

We performed cyclic voltammetry for OsN3|TiO_2|FTO at several scan rates and used the modified Randles-Sevcik Equation to extract the apparent diffusion coefficient of self-exchange electron transfer. One example dataset is shown in **Figure 15**.

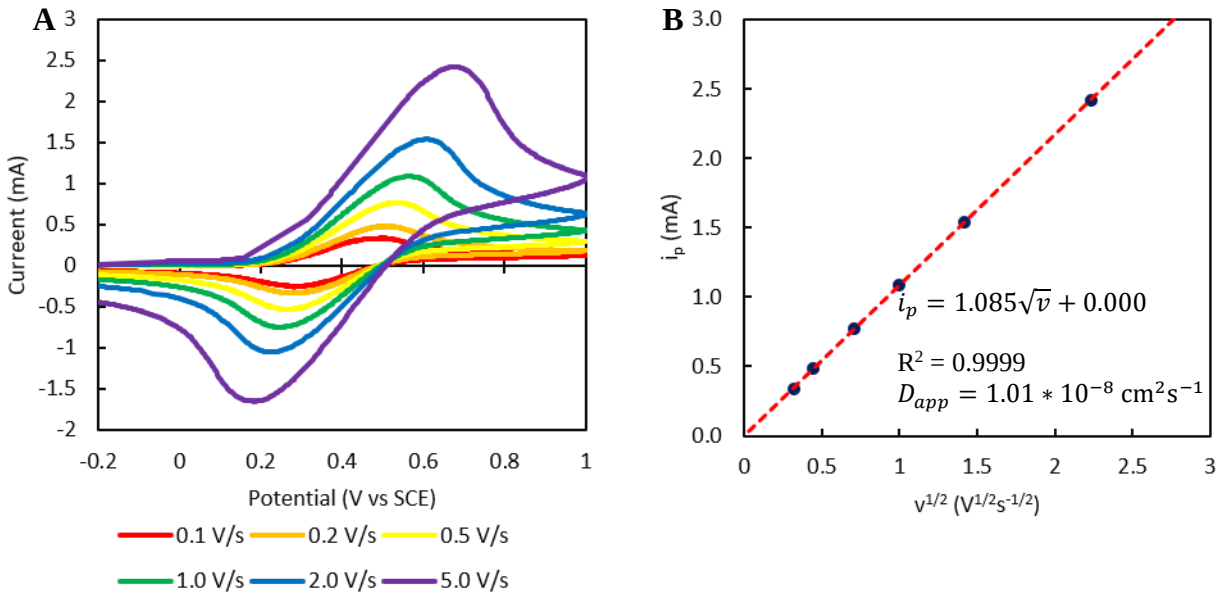

Figure 15: (a) Cyclic voltammograms at several scan rates of OsN3|TiO_2|FTO immersed in 100 mM $TBAClO_4$ acetonitrile solution. (b) Peak current plotted as a function of the square root of the scan rate (blue circles) with best-fit equation (dashed red line), R^2, and D_{app} shown.

This measurement was performed on 22 samples, which resulted in an average D_{app} value of 1.0×10^{-8} cm^2 s^{-1} and a standard deviation of 0.3×10^{-8} cm^2 s^{-1}. The D_{app} value obtained by cyclic voltammetry is best compared to the D_{app} value obtained by chronoamperometry because both techniques use the same assumptions for dye concentration and use current as their reporting value. We observed that D_{app} values obtained by cyclic voltammetry were typically smaller than D_{app} values obtained by chronoamperometry even after correcting for α.

One possible explanation for this discrepancy is that the peak current of cyclic voltammograms is decreased in systems with significant potential drop due to uncompensated resistance. Our systems typically had uncompensated resistance values (R_u) of ~40 Ω. We wrote

a simple finite-element analysis cyclic voltammetry modeling program to investigate the effect of α and uncompensated resistance on measured D_{app} values using the Randles-Sevcik equation (**Equation 13**). **Figure 16** contains modeled cyclic voltammograms using simple typical values for our system both including and neglecting α. Notice that the modeled cyclic voltammogram with α = 2.2 has earlier onset of oxidation and reduction in the forward and reverse sweeps, decreased peak height, and greater peak-to-peak splitting than the modeled cyclic voltammogram with α = 1. This result is a critical observation, because the peak height is the important parameter used to determine D_{app} using cyclic voltammetry.

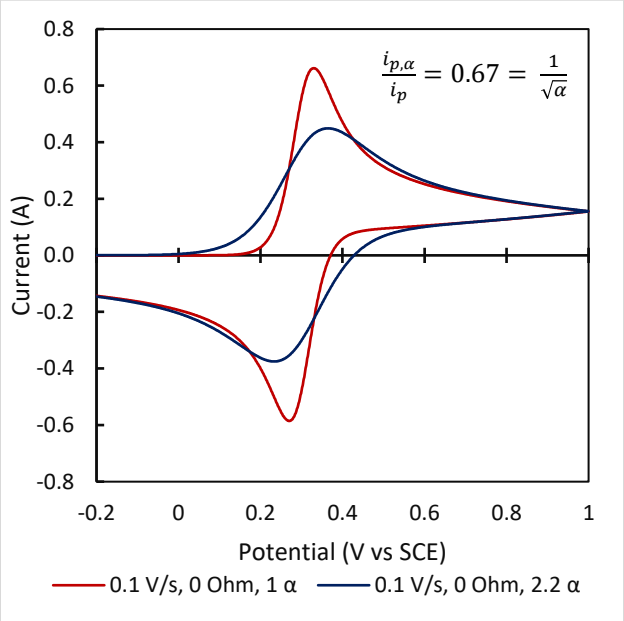

Figure 16: Simulated cyclic voltammograms of OsN3|TiO_2|FTO with peak current ratio shown and the following standard values: d = 5 μm, T = 298 K, A = 0.4 cm^2, C = 0.2 M, $E^{o'}$ = 0.3 V vs SCE, D_{app} = 1 × 10^{-8} cm^2 s^{-1}; red: α = 1 (ideal), R_u = 0 Ω, v = 0.1 V s^{-1}; blue: α = 2.2 (typical), R_u = 0 Ω, v = 0.1 V s^{-1}.

Figure 17 contains modeled cyclic voltammograms using simple typical values for our system both including and neglecting uncompensated resistance. Notice that modeled cyclic voltammograms that include a contribution due to uncompensated resistance have smaller peak currents and greater peak-to-peak splitting than modeled cyclic voltammograms that neglect uncompensated resistance. This affect is more profound at higher scan rates due to the resulting

larger current and potential drop due to uncompensated resistance. This is also a critical observation, because as mentioned above, the peak height it the important parameter used to determine D_{app} using cyclic voltammetry.

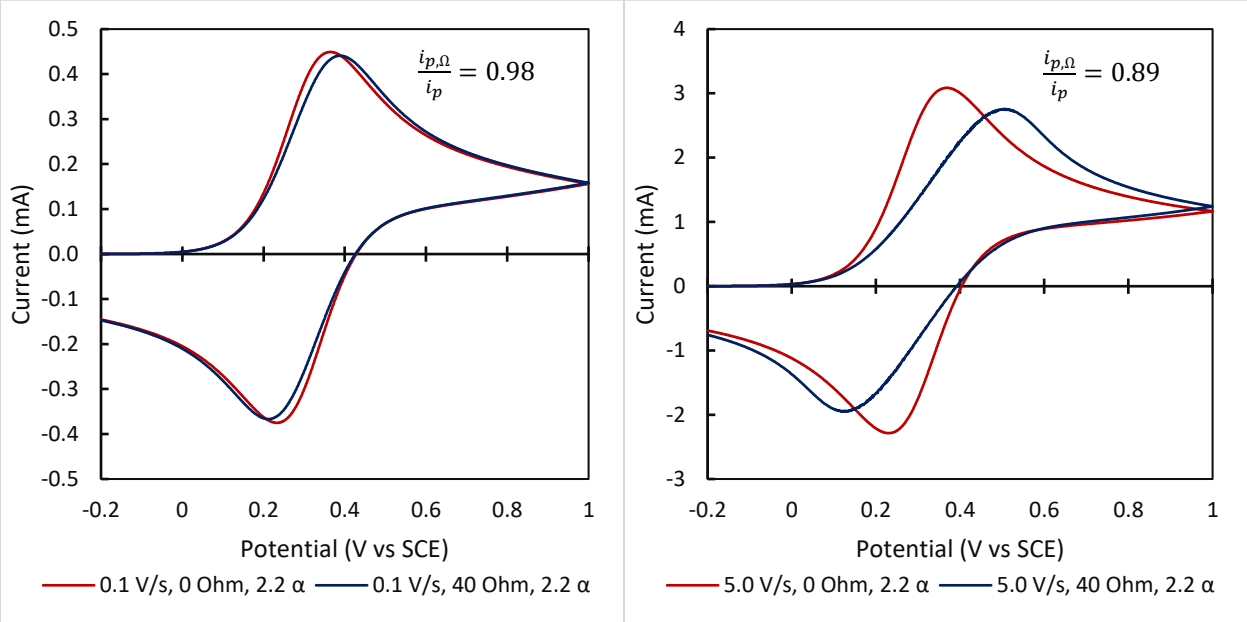

Figure 17: Modeled cyclic voltammograms of OsN3 dyed TiO_2 mesoporous films with standard values. d=5 μm, T = 298 K, A = 0.4 cm^2, C = 0.2 M, E_0' = 0.3 V vs SCE, D_{app} = 1×10^{-8} cm^2s^{-1}. Left) Red: α = 2.2, R_u = 0 Ω (ideal), v = 0.1 Vs^{-1}. Blue: α = 2.2, R_u = 40 Ω (typical), v = 0.1 Vs^{-1}. Right) Red: α = 2.2, R_u = 0 Ω (ideal), v = 5.0 Vs^{-1}. Blue: α = 2.2, R_u = 40 Ω (typical), v = 5.0 Vs^{-1}. Peak current ratios inset.

Figure 18 contains modeled cyclic voltammograms using average measured values for OsN3 on TiO_2 assuming a D_{app} value of 1.16×10^{-8} cm^2 s^{-1} and 47.2 Ω resistance at several scan rates. The resulting peak currents are fit to a line and the slope is used to measure a new D_{app} value of 8.01×10^{-9} cm^2 s^{-1}. Even though the modeled peak current as a function of the square root of scan rate closely fits a line with an R^2 of 0.9987 it yields an underestimation of the original simulated D_{app} value by a factor of 0.69. The experimental ratio of D_{app} as measured by cyclic voltammetry to D_{app} as measured by chronoamperometry was 0.90. This discrepancy is less than we would expect, even after correcting for uncompensated resistance. This is probably

due potential-dependent anodic background current, which was also observed in chronoamperometry experiments, contributing to the peak current.

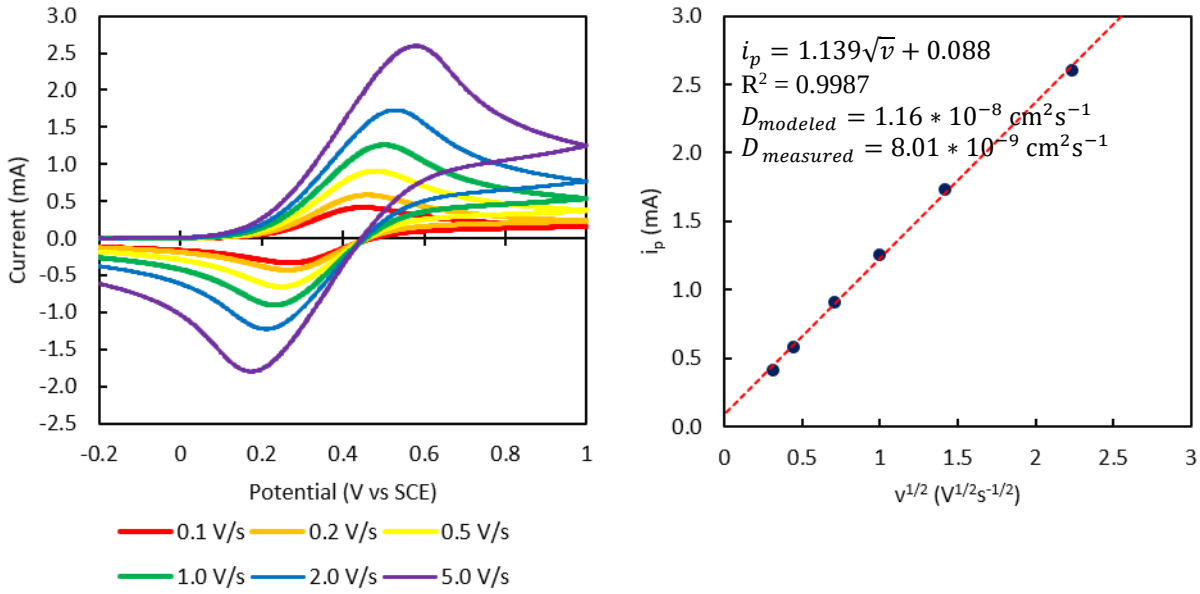

Figure 18: Left: modeled cyclic voltammograms of OsN3 dyed TiO_2 mesoporous films at multiple scan rates with average values. d = 5.58 µm, T = 293.7 K, A = 0.412 cm^2, C = 0.170 M, $E^{o'}$ = 0.325 V vs SCE, D_{app} = 1.16 × 10^{-8} cm^2 s^{-1}, R_u = 47.2 Ω, α = 2.22. Right: peak modeled current plotted as a function of the square root of scan rate with fitting function, R^2, and D_{app} inset. Blue circles are modeled data and the red dashed line is the linear fit.

Dye Concentration and Electroactivity

It is possible that not all dyes bound to the surface of the mesoporous film are accessible via a self-exchange electron-transfer percolation network. Inaccessible dyes would be inactive in D_{app} measurement techniques because they would not contribute to current measured by chronoamperometry and cyclic voltammetry or the change in film absorbance. The total concentration of dyes on the films was measured by a dye desorption experiment and compared to the electroactive dye concentration measured by chronoamperometry. On average, 79% of dyes were electroactive with a standard deviation of 13%. **Equation 14** describes the effect different measured concentrations have on measured D_{app} value using chronoamperometry or

cyclic voltammetry. In our case, this would reduce the average measured D_{app} value by a factor of 0.62.

(14) Comparison of D_{app} values obtained using different concentration measurements

$$\frac{D_{\text{total}}}{D_{\text{active}}} = \left(\frac{C_{\text{active}}}{C_{\text{total}}}\right)^2$$

One interesting application of **Equation 14** is to estimate the proportion of active dyes in a sample by comparing D_{app} values measured by chronoamperometry or cyclic voltammetry with the D_{app} value measured by spectroelectrochemistry. The D_{app} value measured by spectroelectrochemistry always uses the active concentration of dyes by internal normalization of the change in absorption, yielding D_{active}. The D_{app} values determined by chronoamperometry and cyclic are dependent on the dye concentration measurement method. Using the dye desorption method of concentration determination would allow determination of D_{total}. This could be useful if there were large background or capacitive currents in chronoamperometry experiments preventing direct electrochemical measurement of electroactive dye concentration.

Outlook and Relevance to Studies on Dye-Sensitized Mesoporous Materials

The analyses above clearly show that there are confounding effects in each method used to quantify the effective diffusion coefficient, D_{app}, as a representation value for the rate of self-exchange electron transfer across the surface of these materials scaffolds. Care must be taken when using each method so that accurate values of D_{app} can be obtained.

For chronoamperometry, time-dependent and potential-dependent background currents were subtracted from the measured current values. This step could be eliminated or reduced in significance by using greater purity electrolyte solution and using a reference electrode that does not introduce contaminants as the SCE's likely did. The electroactive dye concentration was calculated based on the total corrected current passed during the measurement, the film area

measured by image analysis, and the average film thickness measured by profilometry. Measuring the total dye concentration by dye desorption instead of charged passed yields a larger concentration and smaller D_{app} value that could not be compared with D_{app} values obtained using chronoabsorptometry.

For chronoabsorptimetry, the electroactive dye concentration was internally assumed by normalization of the change in absorption during the measurement. The average film thickness was measured using profilometry but did not always perfectly match the film thickness at the probe beam location. To account for this discrepancy many samples were measured and the results averaged. An alternative way to avoid this error would be precise control of film thickness, sample placement, beam size, and beam location.

For cyclic voltammetry, the Randles-Sevcik equation was modified to account for non-Nernstian behavior of dyes bound to TiO_2. The correction factor was determined by steady state spectroelectrochemistry. The dye concentration was determined by measuring using the same methods as the chronoamperometry experiments. The film was fully reduced prior to each measurement by application of a sufficiently negative potential step and the first sweep of the cyclic voltammogram was used. The D_{app} values determined this way were smaller than D_{app} values determined by chronoamperometry and chronoabsorptometry because of the effects of uncompensated resistance on cyclic voltammetry peak height. However, correcting for resistance created D_{app} values that were larger than those obtained by chronoamperometry and chronoabsorptometry because of the contribution of the time-dependent, potential-dependent background currents, also observed in chronoamperometry experiments, to peak current height. This background current could not be easily corrected for due to its time-dependent, potential-dependent, surface-area-dependent, and likely dye-mediated nature. Uncompensated resistance

should be minimized by using small electrodes and placing the reference electrode as close to the working electrode as possible. Background currents can be minimized in the same way described for chronoamperometry experiments. In the absence of significant uncompensated resistance and background currents the non-ideality factor can be estimated by measuring the peak to peak separation in the cyclic voltammogram, eliminating the need for the steady state spectroelectrochemistry measurement using **Equation** $\Delta E_p = \frac{2.22\alpha RT}{nF}$ (15**.**

$$\Delta E_p = \frac{2.22\alpha RT}{nF} \tag{15}$$

D_{app} values measured under anodic and cathodic conditions using chronoamperometery and chronoabsorptometry were often different on individual films but were statistically the same when averaged over many films. D_{app} values varied from film to film and were dependent on electroactive dye concentration. Consecutive measurements of D_{app} on the same film also showed some variation. D_{app} values measured simultaneously using chronoamperometry and chonoabsorptometry often yielded different results because chronoamperometry sampled the full film but chronoabsoptometry only sampled the location of the probe beam and film surfaces were not perfectly flat. However, when averaged over many films, D_{app} values measured using chronoamperometry and chronoabsorptomery were the same within error. Ultimately, even when taking great care to control the experimental conditions, data averaging was necessary to obtain consistent results.

If these considerations are not taken into account, then the accuracy of calculated D_{app} values can suffer significantly. Only once accurate analyses of data are performed can values measured by different researchers and different research groups be compared so that collective trends and knowledge about what limits values of D_{app} can be identified. Another confounding

factor, which we did not explore here, is that film morphology likely affects D_{app} values. In order for multiple groups to compare values, they will need to use the same film preparation techniques as well.

Conclusions

D_{app} values for self-exchange electron-transfer reactions between OsN3, an infrared-absorbing osmium–polypyridyl dye which is stable for hours in the Os(III) oxidized state, bound to mesoporous TiO_2 thin films were measured using chronoamperometry, chonoabsorptometry, and cyclic voltammetry and the results were compared. Chronoamperometry was the simplest of the three techniques to perform as it does not require a spectrometer, but required background current correction. Chonoabsorptometry was more difficult to perform than chronoamperometry because it requires the use of a spectrometer in tandem with a potentiostat or source meter. Chonoabsorptometry results were easier to interpret than chronoamperometry because absorption measurements were insensitive to background and capacitive currents and therefore required fewer corrections. Cyclic voltammetry was the most difficult technique to perform accurately due to the greater number of supporting measurements and necessary corrections. Due to the non-Nernstian behavior of dyes when bound to mesoporous TiO_2, a non-ideality correction factor was added to the Nernst and Randles-Sevcik equations as measured by spectroelectrochemistry. D_{app} values measured by cyclic voltammetry were smaller than D_{app} values measured by chronoamperometry due to a reduction in peak height caused by uncompensated resistance. Dye concentrations determined by chronoamperometry and dye desorption methods gave different results because not all dyes bound to the surface were electroactive.

Experimental Section

A Note of Explanation

When this experiment was initially conceived, different electrolytes in solution and in base-pretreatment were expected to yield different D_{app} values. We prepared samples using multiple mixtures of both aqueous LiOH and TBAOH in base-pretreatment solutions and ran our experiments in multiple mixtures of $LiClO_4$ and $TBAClO_4$ electrolyte. While it is possible that there may still be an effect of base-pretreatment and solution electrolyte on D_{app}, this effect is small compared to the natural slide-to-slide variation and could not be distinguished with the 22 samples that we report herein and so the results are reported in aggregate.

Reagents and Chemicals

All chemicals were purchased and used without further purification unless stated otherwise. For spectroelectrochemical experiments and laser spectroscopy studies the following reagents were used: acetonitrile (ACS/HPLC 99.9%, Honeywell Burdick & Jackson), methanol (certified ACS 99.9%, Fisher Chemical), lithium perchlorate (battery grade 99.99%, Aldrich), tetra-*n*-butylammonium perchlorate (98%, TCI), which was additionally purified by recrystallization from methanol, Alconox powdered precision cleaner (Alconox), lithium hydroxide (laboratory grade anhydrous, Fisher Scientific), tetra-*n*-butylammonium hydroxide 40%, w/w aqueous solution (Alfa Aesar), lithium iodide (99%, anhydrous, Acros Organics), tetra-*n*-butylammonium iodide (≥ 99.0%, Aldrich).

Preparation of Dyed Thin Films for Spectroelectrochemical Measurements

Fluorine-doped tin–oxide-coated glass (FTO) substrates (2.0 cm × 0.9 cm × 2.2 mm, TEC 7, Hartford Glass) were sonicated in 5% wt aqueous Alconox solution for 15 min, rinsed with water, sonicated in ethanol for 15 min, and rinsed with ethanol. A 5 mm strip of TiO_2 paste was

applied 3 mm from one of the short edges of the FTO using the doctor blade method with Scotch Magic Tape spacer and a Teflon coated razor blade and sintered in a box muffle furnace. The experimentally optimized procedure is as follows: temperature was raised at a rate of 3 °C per minutes to 90 °C, held at 90 °C for 1 h, raised at a rate of 3 °C per minutes to 500 °C, held at 500 °C for 1 h, and then allowed to cool to room temperature. A 7 cm long "gas and oil resistant II" insulated multicore zinc–copper wire was cut and 5 mm of insulation was stripped from each end. The wire was taped to the conductive side of the FTO substrate opposite of the TiO_2 thin film using copper foil tape with conductive adhesive (Freely). GE White Silicone II was applied to the wire, copper tape, and FTO to completely cover any exposed metal surface that could come in contact with electrolyte solution and allowed to cure in air overnight. The thin films were then base-pretreated for 15 minutes in a 1 mM total concentration aqueous solution containing LiOH, TBAOH, or a combination thereof with a LiOH:TBAOH molar ratio equal to the initial ratio of Li^+ and TBA^+ used in the acetonitrile electrolyte in subsequent electrochemistry experiments. Excess water and base were removed by soaking in acetonitrile for 15 minutes. The thin film was then immersed in a 1 mg/mL dye solution[37] containing 1:1, v/v of acetonitrile and methanol for a minimum of 48 h. Dyed slides were then soaked twice for 15 minutes in acetonitrile immediately prior to measurement to remove weakly bound dyes.

Preparation of Dyed Films for Nanosecond Transient Absorption Measurements

Glass slides (1.5" × 0.5" × 1 mm, Fisherbrand Plain Microscope Slides) were sonicated in 5% wt aqueous Alconox solution for 15 min, rinsed with water and ethanol, sonicated in ethanol for 15 min, and rinsed with ethanol. TiO_2 paste was then applied to 0.25 square inches of the glass slide using the doctor blade method with Scotch Magic Tape spacer and sintered in a box

muffle furnace. The temperature was raised at a rate of 3 °C per minutes to 90 °C, held at 90 °C for 1 h, raised at a rate of 3 °C per minutes to 500 °C, held at 500 °C for 1 h, and then allowed to cool to room temperature. The thin film was then base-pretreated for 15 minutes in a pH 11 aqueous solution containing LiOH, TBAOH, or a combination thereof with a LiOH:TBAOH ratio equal to the initial ratio of Li^+ and TBA^+ used in the acetonitrile electrolyte in subsequent laser experiments. The thin film was then immersed in a saturated dye solution[37] containing 3:1, v/v of acetonitrile and methanol for a minimum of 48 h. Dyed slides were then soaked for 15 minutes in 100 mM solutions of LiI, TBAI, or a combination thereof with a LiOH:TBAOH ratio equal to the initial ratio of Li^+ and TBA^+ used in the acetonitrile electrolyte in subsequent laser experiments, to chemically reduce any dyes in the Os(III) state to the Os(II) state as observed by electronic absorption spectroscopy. Immediately prior to measurement dyed slides were soaked twice for 15 minutes each in acetonitrile to remove weakly bound dyes.

Electrochemical and Photoelectrochemical Measurements

General Procedures

Three-electrode electrochemical measurements were performed using a Bio-Logic VSP-300 potentiostat in grounded mode using a dyed TiO_2 working electrode, an aqueous KCl-saturated calomel electrode reference electrode, and a platinum mesh counter electrode. The three electrodes, a magnetic stir bar, and 14 ml of supporting electrolyte were assembled into a 1 cm × 1 cm custom borosilicate glass spectroelectrochemical cuvette that was placed in an Agilent Cary 60 Electronic Absorption Spectrophotometer. The cell was sealed and purged with argon gas for 15 minutes prior to measurement. Stirring and argon bubbling continued during all electrochemical experiments.

Cyclic Voltammetry

The working electrode was places as close as possible, ~3 mm, to the reference electrode frit. An initial open-circuit potential measurement was performed for 30 sec to ensure that the cell was set-up correctly. This was followed by cyclic voltammetry measurements with scan limits of 1.0 V and –0.2 V versus reference and scan rates of 20, 10, 5, 2, 1, 0.5, 0.2, and 0.1 V/s, performing two scans at each scan rate.

Chronoamperometry

The working electrode was lowered so that the dyed TiO_2 film was facing the incident optical probe beam and positioned orthogonal to it. Potentiostatic chronoamperometry measurements were performed while measuring current and total absorbance at 790 nm, which corresponds to the peak absorbance of the metal-to-ligand charge transfer direct triplet excitation band, every 0.1 s. Potentials steps of 1.0 V versus reference, which is well positive of the redox potential of the dye, ~0.325 V, and 0.0 V versus reference which is quite negative of the redox potential of the dye were applied 12 times each, alternating every 5 minutes. The large potential steps were important to avoid having interfacial electron-transfer limit the observed behavior so that only inter-dye self-exchange electron transfer dominates, behavior that was important for analysis using the Cottrell/Anson equations and interpretations of the behavior as such.

Steady State Spectroelectrochemistry

Steady State Spectroelectrochemistry was performed immediately following chronoamperometry experiments without changing the cell geometry. Potential steps were applied from 0.00 to 0.70 V vs SCE in increments of 0.05 V. After each potential step is applied,

the absorbance at 790 nm was observed until no additional change could be seen, usually 3 to 10 minutes after the potential step was applied. A full spectrum scan was then taken from 200 nm to 1100 nm before the next potential step was applied.

Dye Desorption Measurements

An aqueous stock solution containing 10 mM $Na_2S_2O_4$ and 10 mM LiOH was prepared. $Na_2S_2O_4$ was chosen for its reducing properties and LiOH was chosen for its ability to desorb and dissolve bound dyes at concentrations above 1 mM. A standard dye solution was prepared by dissolving solid OsN3 dye in the reducing stock solution to make a 0.1 mM dye solution which was serially diluted to make solutions with OsN3 concentrations of 0.05 mM, 0.025 mM, 0.0125 mM, 0.00625 mM, and 0.003125 mM. Electronic absorption spectra from 200 nm to 1100 nm were taken of the OsN3 dying solutions in a standard 1 cm quartz cuvette using basic reducing stock solution as a blank. The resulting spectra were linearly fit to determine the molar absorptivity coefficients of OsN3 under the given conditions. After electrochemical measurement dyed slides were stripped of attached wires, tape, and caulk by scraping with a razor blade. The remaining dyed TiO_2 on FTO slide was immersed in 3 ml of basic reducing stock solution for a minimum time of 15 minutes and a maximum time of 1 h during which the solution was gently shaken every 5 minutes. Each slide was then removed from solution and observed to be colorless. Electronic absorption spectra from 200 nm to 1100 nm of the desorption solution in a standard 1 cm quartz cuvette was then taken using basic reducing stock solution as a blank. The resulting spectra were then compared with the calibrated molar absorptivity spectrum to determine total dye concentration in the desorption solution.

Film Thickness Measurements

Profilometry

A profilometer (Bruker Dektak XT) was used to measure the step height and profile between the bare FTO and mesoporous TiO_2 film of the samples. The system used a 12.5 μm radius tip perpendicular to the sample with 5 mg of force scanned over 6 mm in 30 seconds.

Scanning Electron Microscopy

Scanning electron microscopy images and energy-dispersive X-ray spectroscopy overlays of several thin films were acquired on an FEI Magellan 400L XHR and film thicknesses were estimated from cross-sectional images. The drawing tool in the analysis software provided by FEI was used to measure distances from the TiO_2|FTO interface to the top surface of TiO_2. Scanning electron microscopy measurements were found to be generally consistent with profilometry measurements and our expectations of film composition.

Experimental Series

Mixed Electrolyte Series

Measurements were performed in acetonitrile solutions containing one of the following: 100 mM $LiClO_4$, 100 mM $TBAClO_4$, and 10:90 mM, 20:80 mM, 30:70 mM, 40:60 mM, 50:50 mM, 60:40, 70:30 mM, 80:20 mM, and 90:10 mM $LiClO_4$:$TBAClO_4$. For these experiments, the TiO_2 film was both base-pretreated in aqueous base and stored in acetonitrile with identical concentrations of Li^+ and TBA^+ used in the subsequent experiment. Cyclic voltammetry was performed prior to chronoamperometry. Steady state spectroelectrochemistry was not performed. In cyclic voltammetry experiments the second sweep was used and peak currents were measured as the peak current minus the initial current of the forward sweep at -0.2 V. The non-ideality

factor was considered to be the average ideality factor measured in all other experiments. The chronoamperometry experiment of the 70:30 mM ratio slide was disqualified due to electrode connection errors made while repositioning the slide.

Single Electrolyte Series

Measurements were performed in acetonitrile solutions containing either 100 mM $LiClO_4$ or 100 mM $TBAClO_4$. Films were base-pretreated using aqueous solutions of either 1 mM LiOH or 1 mM TBAOH. Three slides were prepared using each of the four possible combinations of conditions. Cyclic voltammetry was performed prior to chronoamperometry and steady state spectroelectrochemistry. Between each cyclic voltammetry experiment of different scan rate chronoamperometry was performed at -0.2 V vs reference for 5 minutes to fully reduce the film. The first sweep was used for analysis and peak current was considered to be the absolute value of the peak current without baseline subtraction. The non-ideality factor was considered to be the non-ideality factor measured for that specific film by steady state spectroelectrochemistry. One experiment was disqualified due to a grounding error.

Nanosecond Transient Absorption Spectroscopy

Dyed films were placed in custom quartz cuvettes with 5 ml of 100 mM supporting electrolyte in acetonitrile, where the supporting electrolyte is composed of $LiClO_4$ and $TBAClO_4$ in a given ratio. Argon was bubbled through the solution for 30 minutes prior to measurement. The samples were placed in a cuvette holder in a custom nanosecond transient absorption spectroscopy system. Transient absorption difference spectra were measured using pump–probe spectroscopy with a 532 nm pump pulse (beam diameter = 8 mm, pulse width = 7 ns FWHM) from the frequency-doubled 1064 nm fundamental line of an Nd:YAG laser (Minilite, Continuum). The laser power was measured using a thermal power sensor head (S310C,

Thorlabs). The continuous-wave probe beam was generated by a xenon arc lamp bulb (150 W, 18 V, 6200 K, IN-02KD2, Interlight). The lamp housing and power supply were taken from an Applied Photophysics LKS60 laser flash photolysis spectrometer. The sample was placed at a 45° angle with respect to both the pump and probe beams, with both beams first traversing the TiO_2-coated side of the glass slides and meeting perpendicular to each other. After passing through the sample and some focusing optics the probe beam enters a monochromator (Cornerstone 260, Newport), equipped with a long-pass filter mounted in a filter wheel (USFW100, Newport) and programmed to remove light of the half-wavelength of ech selected single wavelength, whose intensity is measured by a photomultiplier tube (R928, Hamamatsu) in a 5-stage photomultiplier tube housing taken from an Applied Photophysics LKS60 laser flash photolysis spectrometer. The photomultiplier tube and housing were powered by a high voltage power supply set at 800 V (PS325/2500V-25W, Stanford Research Systems). The signal was digitized by an oscilloscope (HDO4034, Teledyne LeCroy). Signal acquisition was triggered by a silicon diode (FDS100, Thorlabs) off of scattered pump laser light. The laser intensity was 1.3 mJ per pulse for the 100 mM $TBAClO_4$ samples and then reduced to 0.7 mJ per pulse for the remaining samples to provide the same change in absorption at 400 ns after excitation. Data was acquired from 5 μs before the laser pulse to 45 μs after the laser pulse with a 2.5 GHz sampling rate, 20 MHz bandwidth, and terminated at a 50 Ω resistor. Data was collected from 350 nm to 700 nm in 5 nm steps by averaging 1000 shots at a 10 Hz repetition rate under pump–probe and pump only conditions. The data was parsed by subtracting the pump only data from the pump–probe data, averaging signals recorded prior to pulsed-laser excitation, and using that value as the initial light intensity for the calculation of the change in absorbance for each data point. Data was reduced by 100-point averaging.

Example Data Analysis

Chronoamperometry

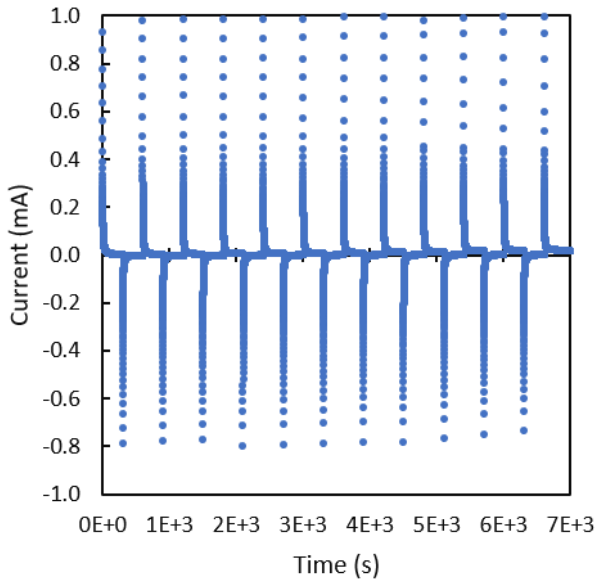

Figure 19. Measured current as a function of time from OsN3|TiO_2|FTO immersed in 100 mM $TBAClO_4$ acetonitrile solution as the potential is alternately stepped between 0.0 *vs* SCE and 1.0 V *vs* SCE.

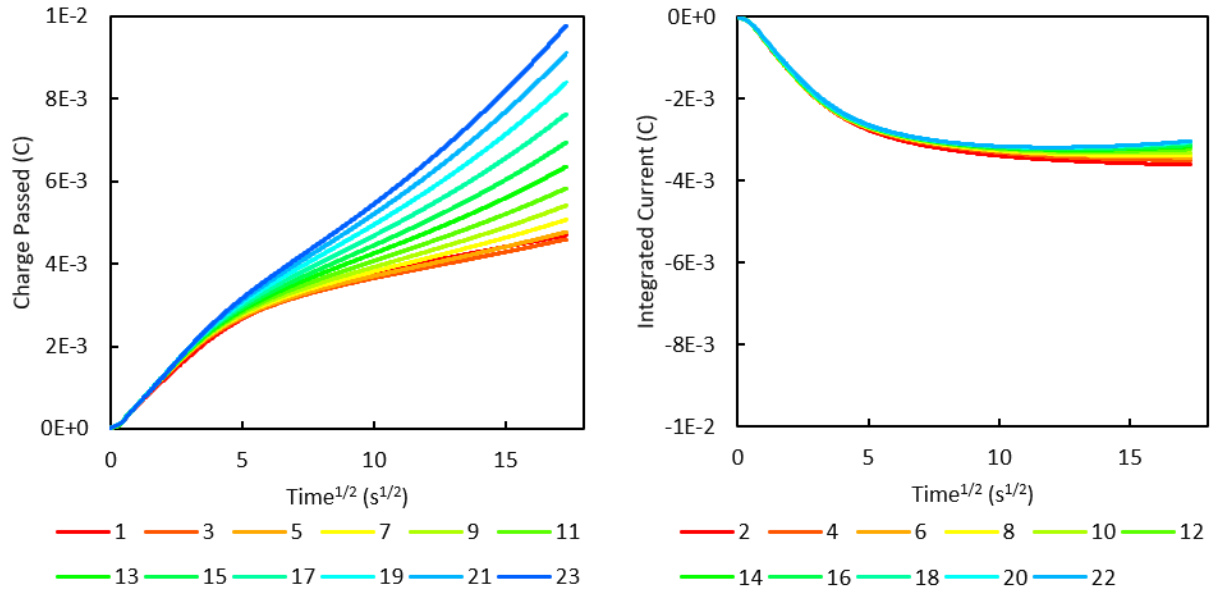

Figure 20: total charge passed as function of the square root of time time at an OsN3 dyed mesoporous TiO_2 film on an FTO electrode in 100 mM $TBAClO_4$ solution in acetonitrile for 12 separate potential steps of 1.0 V vs SCE (right) and 0.0 V vs SCE (left). Note that the total charge passed does not converge as would be expected for a film with a finite amount of dyes.

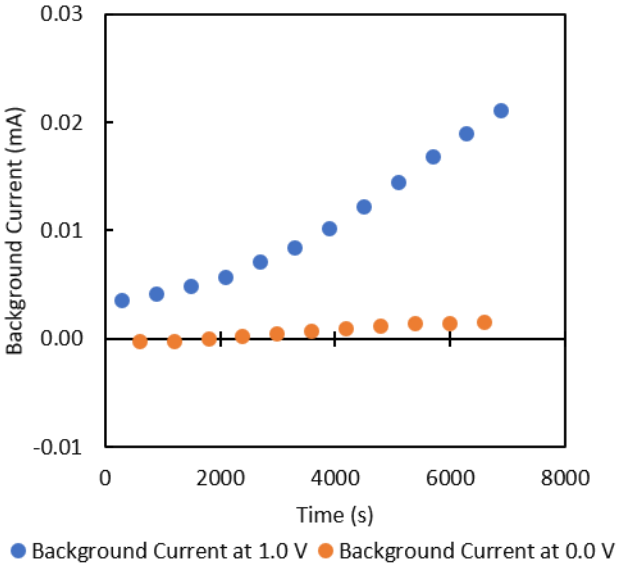

Figure 21: final measured currents for each potential step as a function of time of at an OsN3 dyed mesoporous TiO_2 film on an FTO electrode in 100 mM $TBAClO_4$ solution in acetonitrile. This response is typical for our system. Note that background currents increase over time, probably due to slow introduction of water and chloride ions into the system from the SCE reference electrode.

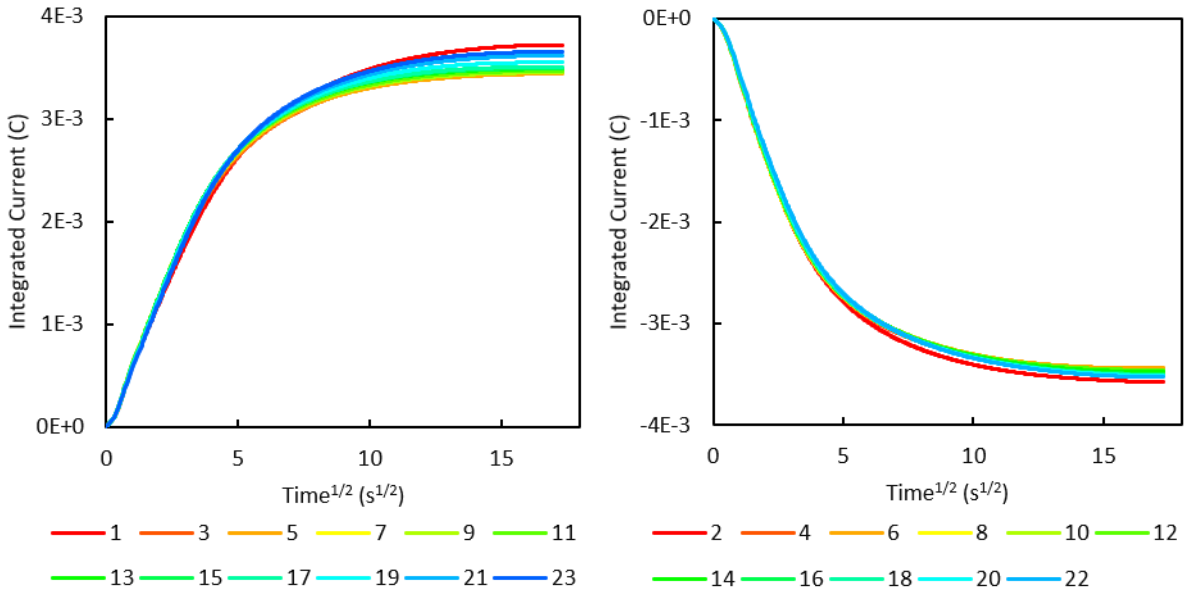

Figure 23: total charge passed after background current correction as function of the square root of time time at an OsN3 dyed mesoporous TiO_2 film on an FTO electrode in 100 mM $TBAClO_4$ solution in acetonitrile for 23 separate potential steps of 1.0 V vs SCE (right) and 0.0 V vs SCE (left). Note that the total charge passed converges as more or less as expected for a film with a finite amount of dyes.

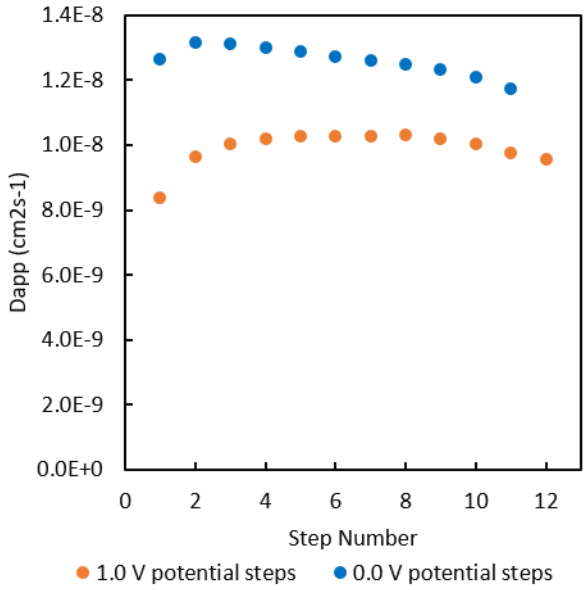

Figure 24: Measured D_{app} using chronoamperometry as a function of potential step cycle number for an OsN3 dyed mesoporous TiO_2 film on an FTO electrode in 100 mM $TBAClO_4$ solution in acetonitrile. Note that there is an initial increase followed by a slow decrease in D_{app}. This behavior is typical of our films.

Chonoabsorptometry

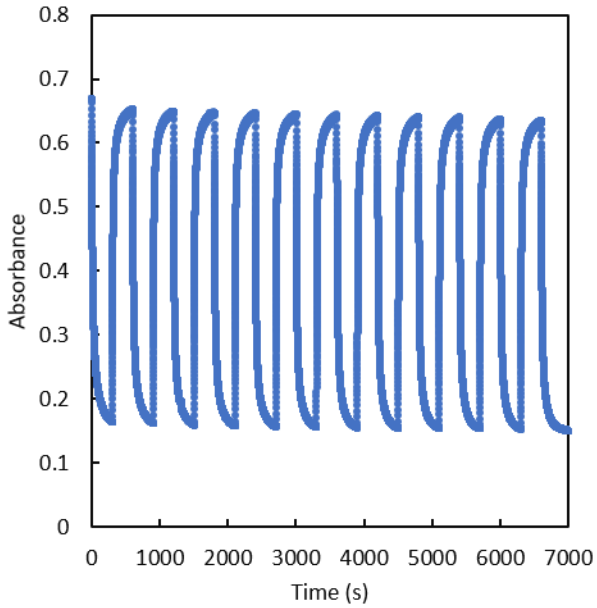

Figure 25: Measured absorbance at 790 nm as a function of time of an OsN3 dyed mesoporous TiO_2 film on an FTO electrode in 100 mM $TBAClO_4$ solution in acetonitrile as potential is alternately stepped between 0.0 vs SCE and 1.0 V vs SCE.

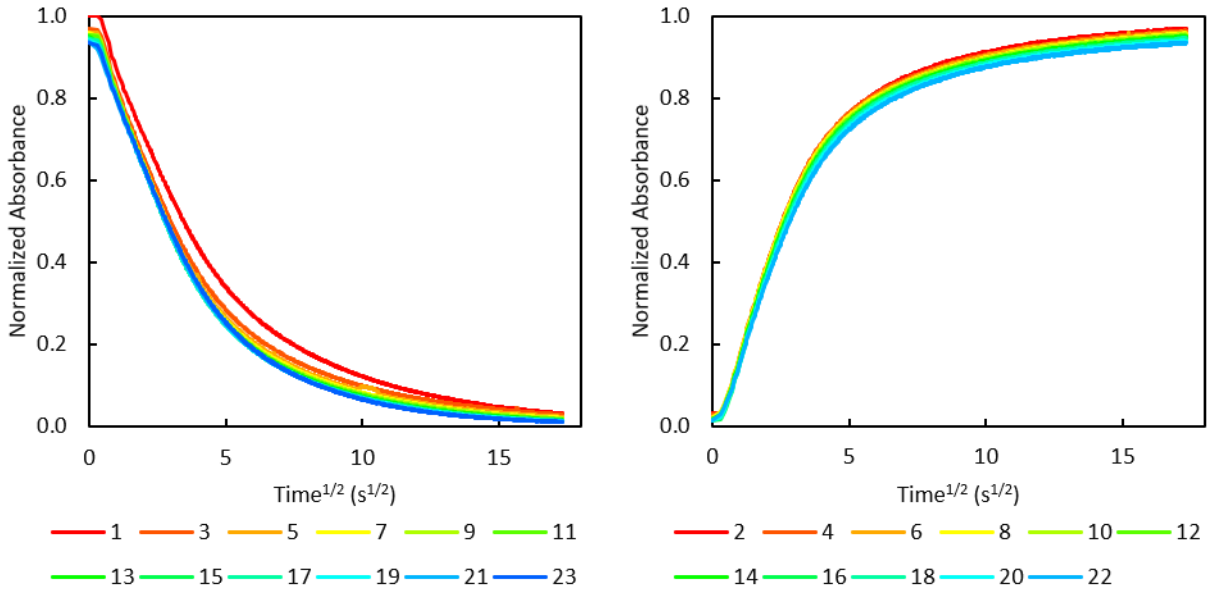

Figure 26: Normalized absorbance at 790 nm as a function of the square root of time of an OsN3 dyed mesoporous TiO_2 film on an FTO electrode in 100 mM $TBAClO_4$ solution in acetonitrile for 23 separate potential steps of 1.0 V vs SCE (right) and 0.0 V vs SCE (left). Note that there is a slight downward shift in both initial and final absorbance values with increasing step number.

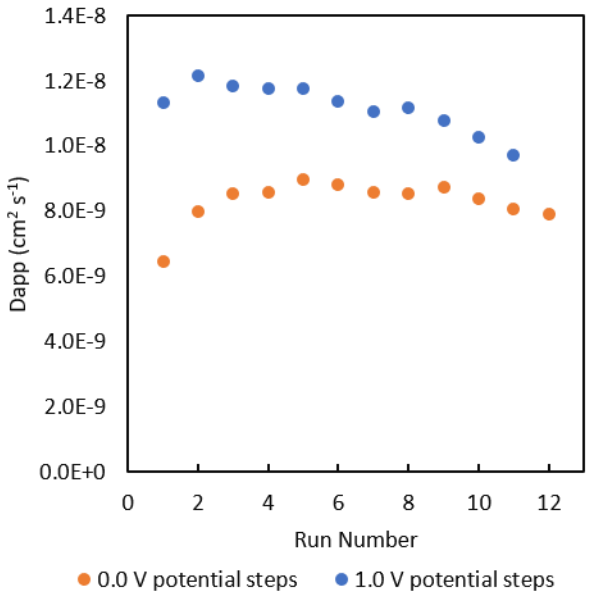

Figure 27: Measured D_{app} using chonoabsorptometry as a function of potential step cycle number for an OsN3 dyed mesoporous TiO_2 film on an FTO electrode in 100 mM $TBAClO_4$ solution in acetonitrile. Note that there is an initial increase followed by a slow decrease in D_{app}. This behavior is typical of our films.

Supporting Measurements

*D*app Concentration Dependence

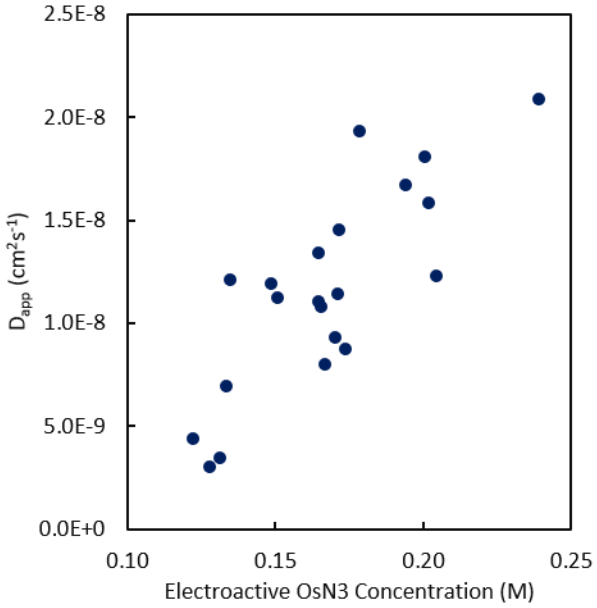

Figure 28: Average D_{app} value of OsN3 dyed TiO_2 films measured by chronoamperometry as a function of electroactive OsN3 concentration measured by chronoamperometry.

Absorptivity Coefficient Determination

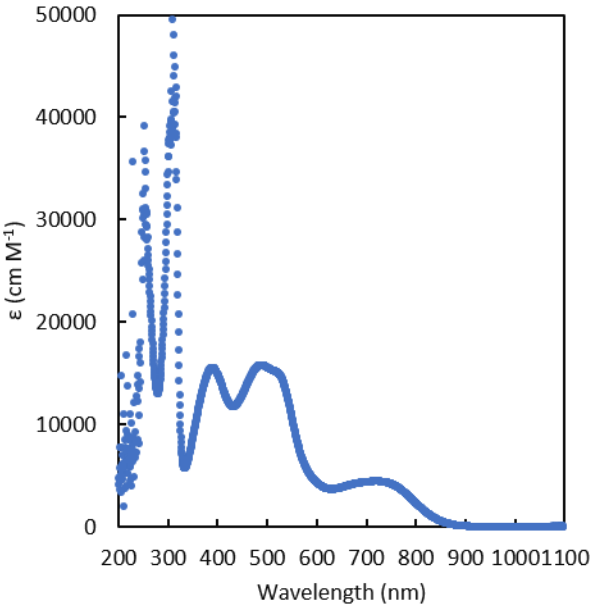

Figure 29: Molar absorptivity coefficient as a function of wavelength of OsN3 dye dissolved in an aqueous solution containing 10 mM $Na_2S_2O_4$ and 10 mM LiOH.

Film Thickness Measurement

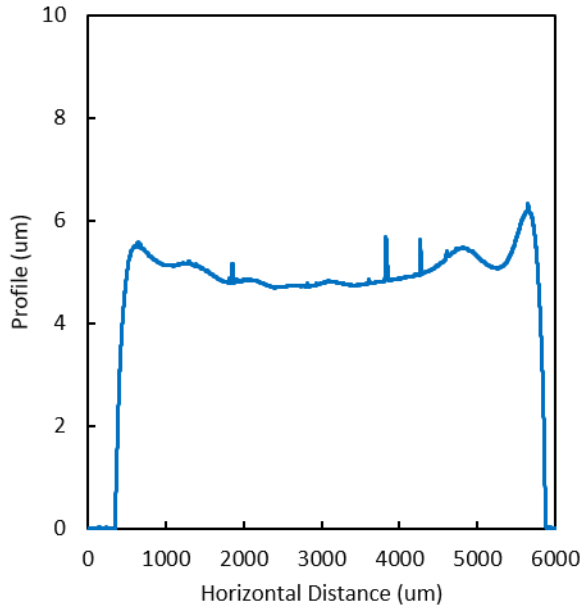

Figure 30: An example of film profile height as a function of horizontal distance as measured by profilometry of a TiO_2 film on FTO glass after dye desorption. Note that the film is thicker at the edges than the middle and contains some random variations which is typical of all the samples we measure.

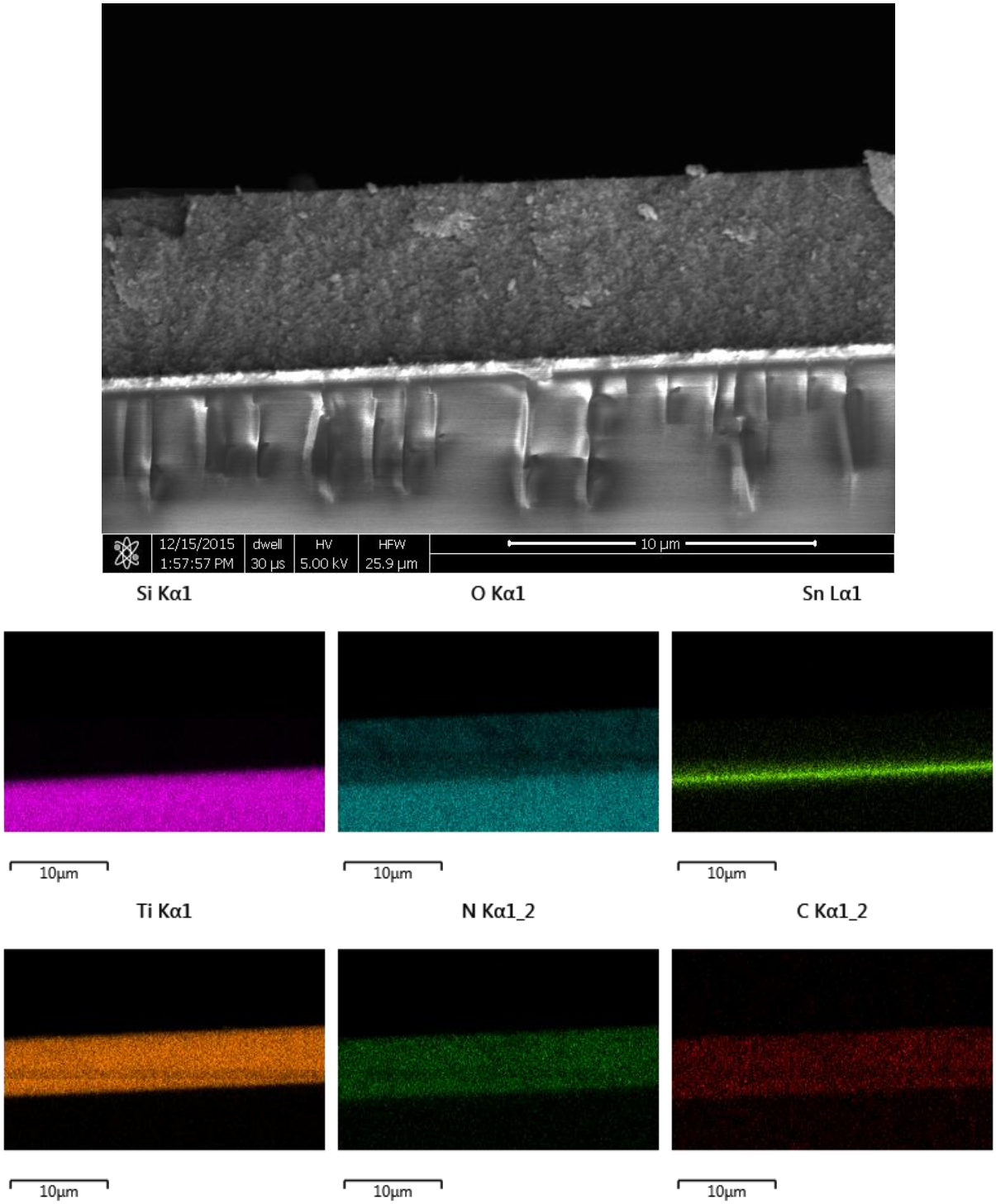

Figure 31. Top Row: cross sectional scanning electron microscopy image of OsN3 dyed mesoporous TiO_2 film on an FTO substrate. Bottom Row: false colored energy-dispersive X-ray spectroscopy images of the same film showing the distribution of various elements.

Nanosecond Transient Absorption

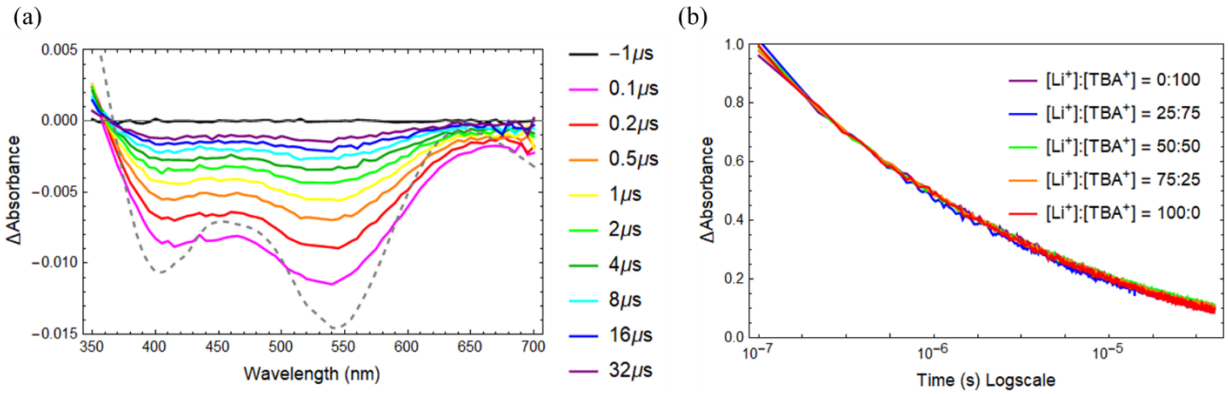

Figure 32: (a) Transient absorption spectra measured at the indicated delay times relative to the arrival of the incident laser pulse for dyed TiO_2 thin films immersed in 100 mM $TBAClO_4$ acetonitrile electrolyte. Overlaid (gray dashed line) is the difference absorption spectrum of the oxidized minus reduced dye ground-state absorption spectra. (b) Normalized transient absorption kinetics on a logarithmic timescale for dyed TiO_2 thin films immersed in acetonitrile electrolytes containing the indicated amounts of $LiClO_4$ and $TBAClO_4$. The nearly identical decay lifetimes support the hypothesis that electrolyte cations do not affect OsN3 hole hopping rates.

Application of Foot-of-the-Wave Analysis to Dyed Mesoporous Semiconducting Thin Films

Introduction

Dyed wide bandgap semiconductors are used as to produce electricity in dye sensitized solar cells (DSSCs)[1,33,34] and to store energy in the form of chemical bonds in solar fuel production schemes.[51] The mechanism in most of these schemes is a dye molecule absorbs a photon, creating an excited electron and a vacant orbital. If the dye is bound to an n-type semiconductor it transfers an electron to the semiconductors conduction band and becomes oxidized. If the semiconductor is p-type, the dye accepts an electron from the valence band of the semiconductor and becomes reduced. The oxidized or reduced dye is then regenerated by a redox couple in the contacting medium, which is usually a liquid electrolyte solution. Dye regeneration by charge transfer catalysis is critically important to device performance and is often the single step with the greatest potential drop in the device.[1] Here we present a method of determining the second order charge transfer rate constant of electron transfer between dyes bound to mesoporous semiconductor surface and redox species in solution using foot-of-the-wave analysis (FotW).[81]

Theory: Foot-of-the-Wave

FotW analysis is a method of interpreting results obtained from linear sweep voltammetry to extract kinetic data. Most kinetic interpretation methods look at data taken in the peak or diffusion limited current-voltage regimes.[82] High-current, high-overpotential conditions can introduce sources of error such as uncompensated IR drop, secondary reactions, substrate consumption, and self-inhibition by reaction products. FotW avoids these sources of error by looking at the "foot" of the current response when only mild potentials and small currents exist. FotW makes the following assumptions: 1) The electrode is only sensitive to the catalyst and not sensitive to the substrate. 2) The initial electron transfer between the electrode and the catalyst is reversible and follows Nernstian behavior. 3) Electron transfer between the catalyst and the substrate is ultimately irreversible even if several reaction steps occur. 4) Electron transfer between the catalyst and the substrate regenerates the catalyst. These assumptions are summarized for the case of oxidative catalysis in **Scheme 1**.

Scheme 1

$$Cat \rightleftarrows Cat^{+} + e^{-}$$

$$Cat^{+} + Sub \rightarrow Cat + Sub^{+}$$

The current response of an electrode under these conditions can be described by **Equation 16** as long as there is not significant substrate consumption and substrate concentration is large compared to catalyst concentration.[80] **Equation 16** can be broken up into two parts: **Equation 17**, which describes the maximum possible catalytic current, and **Equation 18** which is the proportion of catalyst oxidized at the electrode surface at a given potential as described by the Nernst equation. During a linear sweep voltammogram of a system containing catalyst and

substrate, at early times and at low current densities when substrate consumption is small, the current should be linear with respect to the proportion of catalyst molecules that are oxidized at the electrode surface at a given potential.

(16) Catalytic current at an electrode with catalyst in solution

$$i = \frac{nFA[Cat]_0\sqrt{2kD_{Cat}[Sub]_0}}{1 + e^{\frac{nF}{RT}(E^0_{Cat} - E)}}$$

(17) Maximum current at an electrode with a catalyst in solution

$$i_{max} = nFA[Cat]_0\sqrt{2kD_{Cat}[Sub]_0}$$

(18) Proportion of a Nernstian species oxidized at a given potential

$$\frac{[Cat^+]}{[Cat]_0} = \frac{1}{1 + e^{\frac{nF}{RT}(E^0_{Cat} - E)}}$$

Equation 16 can be further simplified by performing linear sweep voltammograms on a solution containing only catalyst and a solution containing both catalyst and substrate. In the absence of substrate, the peak current of the linear sweep voltammogram can be described by the Randles-Sevcik equation (**Equation 19**).

(19) Randles-Sevcik Equation describing peak current of a linear sweep voltammogram

$$i_{peak} = 0.4463nFA[Cat]_0\sqrt{\frac{nFvD_{cat}}{RT}}$$

Normalizing **Equation 16** by **Equation 19** yields **Equation 20** which contains the easily controlled variables scan rate (v) and initial substrate concentration ($[Sub]_0$) while remaining linear with respect to the proportion of catalyst oxidized at the electrode surface at a given potential.

(20) Foot-of-the-wave relationship

$$\frac{i}{i_{0,peak}} = \frac{2.24\sqrt{\frac{RT}{nFv}2k[Sub]_0}}{1 + e^{\frac{nF}{RT}(E^0_{Cat} - E)}}$$

Theory: Application of Foot-of-the-Wave to Dyed Mesoporous Films

FotW is most commonly applied to water electrolysis and CO_2 reduction catalysts.[83–85] This is partially due to the popularity of those two reactions but is also due to how easily they satisfy FotW assumptions. Water electrolysis reactions are slow at many electrodes materials, glassy carbon for example,[86] so it is not difficult to create a system where the electrode is catalyst selective.

A dyed mesoporous wide bandgap semiconductor deposited on fluorine doped tin oxide (FTO) glass can also satisfy FotW assumptions with the bound dyes acting as catalysts and a redox active substrate in contacting solution. Even though dyes are bound and do not physically diffuse as a catalyst would in typical FotW, the positions of oxidized and reduced catalyst molecules change following diffusion kinetics via the hole hopping mechanism described in the previous chapter. FTO glass transfers charge well to surface bound species but does not readily transfer charge with solution species. This allows the electrode to be selectively sensitive to dyes when the substrate is a typical DSSC redox shuttle such as iodide/triiodide,[20,87] cobalt(II/III) complexes,[12,24] and ferrocene/ferrocenium derivatives[15,18] which have fast electron transfer kinetics at most electrode materials. This allows us to measure charge transfer coefficients between dyes and redox couples under DSSC-like conditions after certain corrections are made.

Dyes bound to mesoporous substrate often obey a modified Nernst equation as described in the previous chapter. The non-ideality factor, α, introduced in the modified Nernst equation also must be used to modify all equations derived from the Nernst equation. **Equations 16**, **18**, **19**, and **20** become **Equations (**21, **22**, **23**, and **24**. **Equation 17** is not affected.

(21) Catalytic current of a dyed mesoporous film

$$i = \frac{nFA[Cat]_0\sqrt{2kD_{Cat}[Sub]_0}}{1 + e^{\frac{nF}{\alpha RT}(E^0_{Cat} - E)}}$$

(22) Proportion of dyes on a mesoporous film oxidized at a given potential

$$\frac{[Cat^+]}{[Cat]_0} = \frac{1}{1 + e^{\frac{nF}{\alpha RT}(E^0_{Cat} - E)}}$$

(23)Modified Randles-Sevcik equation describing peak current of a linear sweep voltammogram of a dyed mesoporous film

$$i_{peak} = 0.4463nFA[Cat]_0\sqrt{\frac{nFvD_{cat}}{\alpha RT}}$$

(24) Foot-of-the wave relationship of a dyed mesoporous film

$$\frac{i}{i_{peak}} = \frac{2.24\sqrt{\frac{\alpha RT}{nFv}2k[Sub]_0}}{1 + e^{\frac{nF}{\alpha RT}(E^0_{Cat} - E)}}$$

Theory: Future Improvements

FotW as applied to water oxidation and reduction catalysis is most commonly done using an ultramicroelectrode. One advantage of an UME is that UMEs pass negligible current which results in only minute changes to bulk concentrations and low uncompensated IR drop. Our dye-

sensitized TiO_2 electrodes are much larger, pass more current, and have greater IR drop. This IR drop can perturb the peak current during the catalyst only measurement. To compensate, it is possible to measure the active dye concentration and apparent diffusion coefficient directly using potential step chronoamperometry. This would allow direct use of **Equation 21** and may provide better accuracy given the difficulty of accurately measuring peak current as discussed in the previous chapter. However, this was not done in the work contained in this thesis due to time constraints.

Results and Discussion

We performed FotW on mesoporous TiO_2 deposited on FTO glass electrodes dyed with OsN3 dye. The two substrates used were LiI and 1,1'-dimethylferrocene (dmFc). For each electrode the non-ideality factor, α, and the dye formal oxidation potential were determined using steady state stepwise potential step spectroelectrochemistry. Cyclic voltammetry with multiple scan rates was performed in absence of substrate and with multiple substrate concentrations. Example cyclic voltammograms with a scan rate of 0.1 V s^{-1} varying substrate concentration are shown in **Figure 33**.

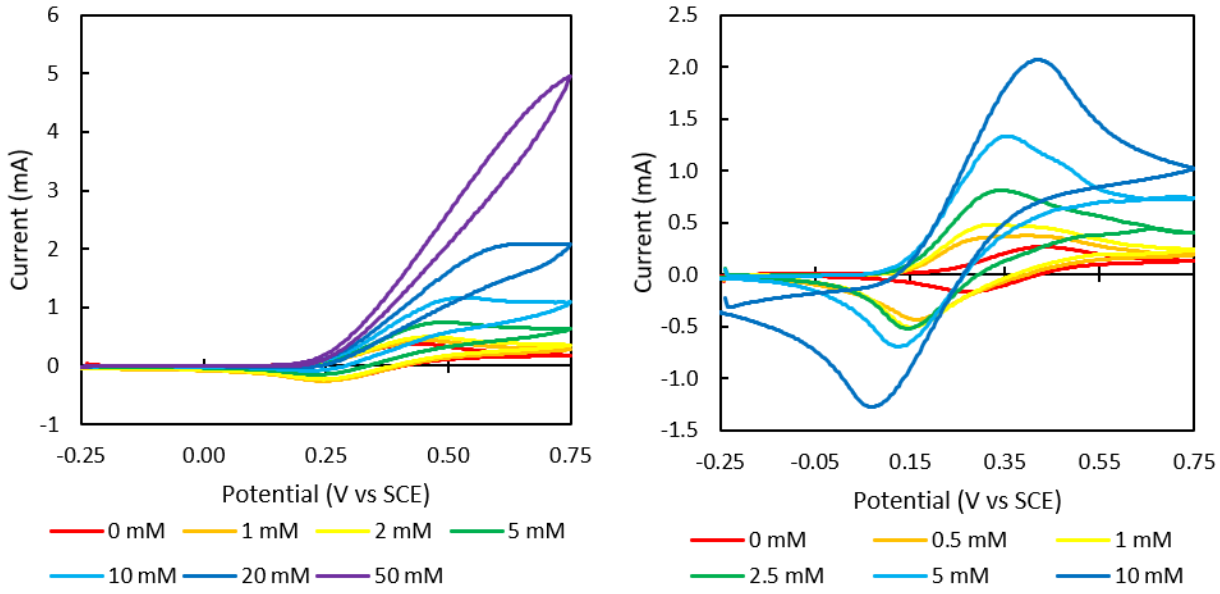

Figure 33: Cyclic voltammograms of OsN3 dyed TiO_2 mesoporous films on FTO glass in 100 mM $LiClO_4$ solution in acetonitrile at 0.1 V s^{-1} scan rate with varying concentration of substrate. Left: LiI as substrate. Right: dmFc as substrate.

To convert each cyclic voltammogram to a FotW style graph, the potential values of the forward potential sweep were transformed into the proportion of dyes oxidized at the electrode surface using **Equation 22**. The corresponding current values were normalized by the peak current of the dyed film in the absence of substrate at the given scan rate. **Figure 34** shows the FotW style graphs of the cyclic voltammograms shown in **Figure 33**.

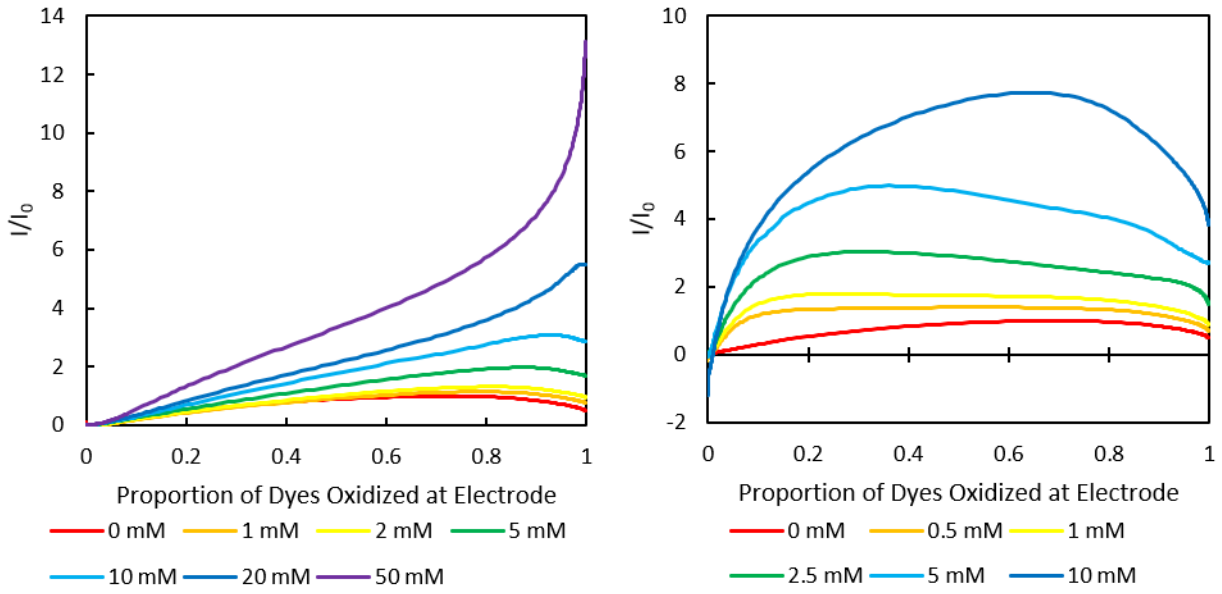

Figure 34: FotW style graphs showing normalized current as a function of the proportion of dyes oxidized at the surface electrode surface of OsN3 dyed TiO_2 mesoporous films on FTO glass in 100 mM $LiClO_4$ solution in acetonitrile at 0.1 V s^{-1} scan rate with varying concentration of substrate. Left: LiI as substrate. Right: dmFc as substrate.

The FotW style graph of OsN3 dye on TiO_2 with LiI substrate shown on the left of **Figure 34** demonstrates the necessary features of a FotW style graph. Each trace originates close to the origin of the graph, indicating that the electrode is selective for the dye. If the FTO electrode were not selective for OsN3 and current was passing from the electrode directly to the LiI substrate, substantial current would pass at potentials negative of the dye oxidation onset due to the standard potential of LiI in acetonitrile falling negative of the formal potential of the dye. This would translate to a FotW y-intercept greater than zero. The graph on the left of **Figure 34** demonstrates a long linear region extending from the origin that is typical of near ideal FotW conditions where substrate consumption is small. The first 40% of these curves were fit to a line as shown in **Figure 35**. 40% dye oxidation at the electrode surface is more than what would be considered the "foot" of the wave, but the response is close enough to ideal that fitting only the foot is not necessary.

The FotW style graph of OsN3 dye on TiO_2 with dmFc substrate shown on the right of **Figure 34** is not as ideal as the FotW style graph with LiI substrate. At low concentrations of dmFc the trace originates close to the origin but at higher concentrations the trace origin drifts towards negative values. This is probably due to the reduction of 1,1'-dimethyl ferrocenium that was created during earlier cyclic voltammograms. The linear region of the trace is also much shorter, quickly forming a humped shape that is typical of FotW conditions where substrate consumption is large.[81] The first 5% of these curves maintain enough linearity to be fit to a line as shown in **Figure 35**. The first 5% is the "foot" of the wave, as the name of this analysis technique implies.

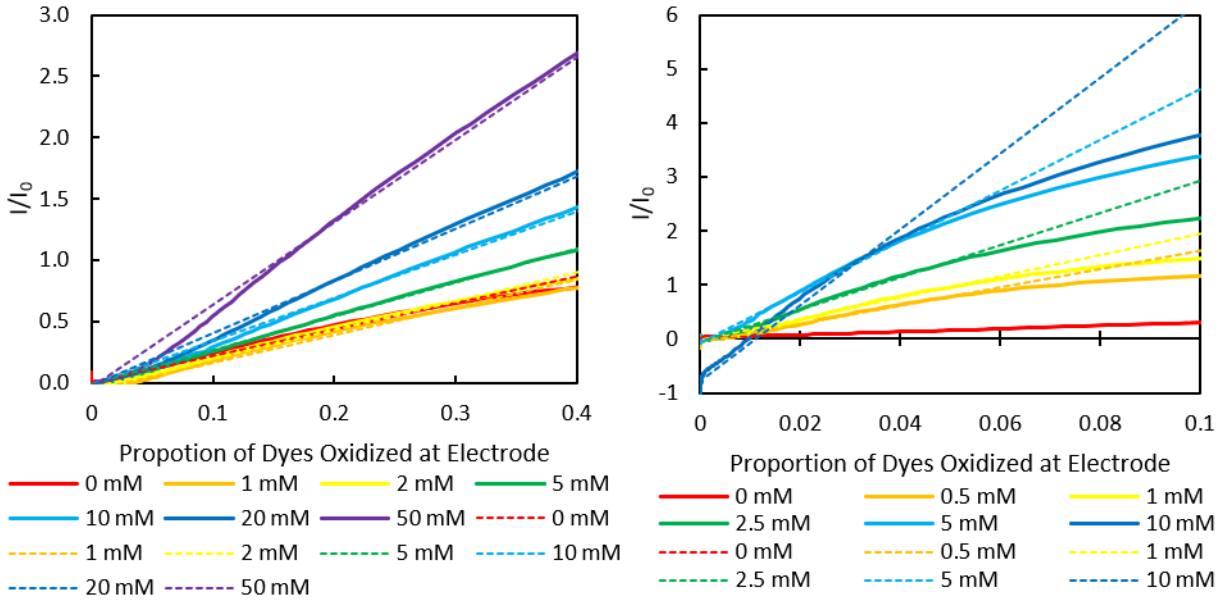

Figure 35: FotW style graphs showing normalized current as a function of the proportion of dyes oxidized at the surface electrode surface of OsN3 dyed TiO_2 mesoporous films on FTO glass in 100 mM $LiClO_4$ solution in acetonitrile at 0.1 V s^{-1} scan rate with varying concentration of substrate. Solid lines are experimental results and dashed lines are fits. Left: LiI as substrate. Right: dmFc as substrate.

The slopes obtained from linear fit of the FotW style graphs should have a linear dependence on the square root of substrate concentration and square root of the inverse scan rate

described in **Equation 25**. The linearity of FotW slope in our system with respect to these variables is shown in **Figure 36**.

(25) Functional form of the FotW slope

$$FotW\ Slope = 2.24\sqrt{\frac{\alpha RT}{nFv}2k[Sub]_0}$$

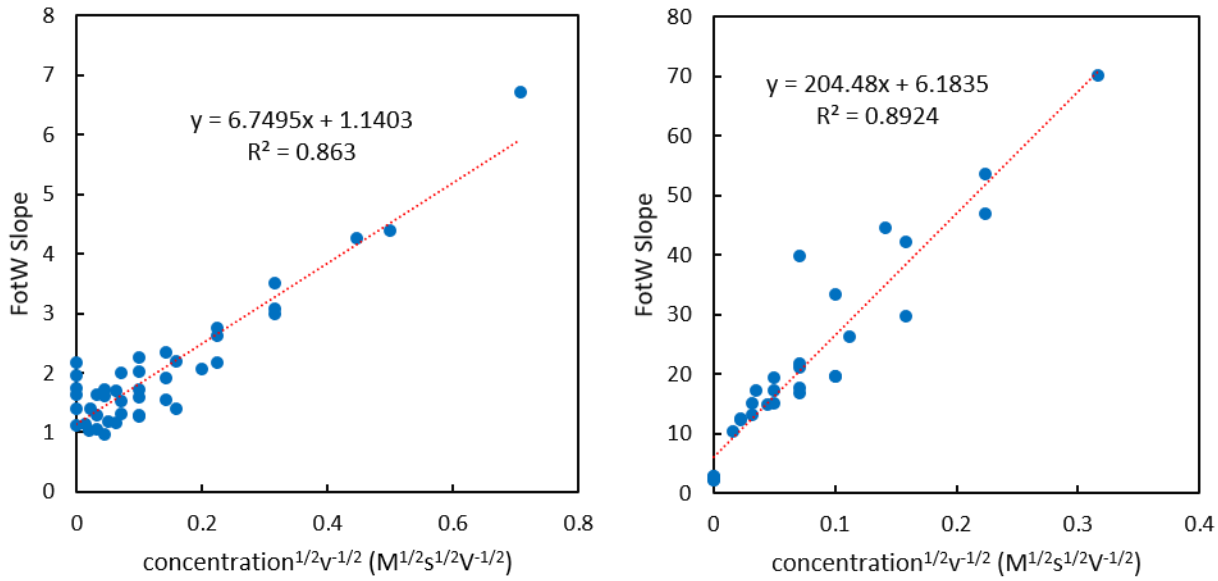

Figure 36: FotW slope of OsN3 dyed TiO_2 mesoporous films on FTO glass in 100 mM $LiClO_4$ solution in acetonitrile as a function of the square root of inverse scan rate times the square root of substrate concentration with linear fitting function and R^2 inset. Blue points are measured values with dashed red line linear fit. Left: LiI as substrate. Right: dmFc as substrate.

The data shown in **Figure 36** show a roughly linear trend with a slope that can be correlated to the second order electron transfer rate constant (k), fundamental constants, and previously measured values using **Equation 26**.

(26) Relationship between k and the slope of FotW slopes

$$Slope = 2.24\sqrt{\frac{\alpha RT}{nF}2k}$$

Table 6: Measured second order rate constants

	dmFc	LiI
OsN3	74,000	78
$OsCl_2$	9,300	
OsI_2	230	< 1

Units are in $M^{-1}s^{-1}$

The values of k for the electron transfer between OsN3, $OsCl_2$, or OsI_2 dyes with dmFc or LiI are listed in

Table **6**. For comparison, a diffusion limited process would have a k value between 10^8 and 10^{10} $M^{-1}s^{-1}$.[88] This indicates that regeneration of the measured oxidized osmium dyes by I^- is slow and would probably limit cell performance while regeneration of these by dmFc would be faster and would probably not limit cell performance except in the case of OsI_2 where regeneration by dmFc is still slow. FotW measurements done by Nazila Farhang on RuN3 dye with LiI substrate suggest that it has a k value of approximately 5000 $M^{-1}s^{-1}$, although these results are not fully realiable due to the poor stability of oxidized RuN3 on the timescale of the experiment. Assuming a 0.5 M I^- concentration in a solar cell environment, the time constant for regeneration would be 25 ms for OsN3 and 0.4 ms for RuN3.

Conclusion

Foot-of-the-wave analysis (FotW) was applied to cyclic voltammograms of dyed titanium dioxide mesoporous thin films on FTO glass electrodes with LiI and 1,1'-dimethylferrocene (dmFc) substrates. This required modification of FotW equations to account for the non-Nernstian behavior of dyes in these conditions. Both substrates demonstrated normalized catalytic currents that were linear with respect to the proportion of dye oxidized at the electrode surface with intercepts near zero, indicating that electron transfer to the substrate is dye mediated. The observed response of LiI was typical of conditions where substrate is not significantly consumed while the observed response of dmFc was typical of a substrate that is rapidly consumed. The slopes of the normalized current with respect to the proportion of dye oxidized at the electrode surface were proportional to the square root of the substrate concentration and the square root of the inverse scan rate. This allowed for the determination of the second order rate constant for electron transfer between oxidized dye and substrate.

Measured rate constants varied from <1 $M^{-1}s^{-1}$ to 74,000 $M^{-1}s^{-1}$. All measured rate constants for interaction between oxidized dye and dimethyl ferrocene were faster than all measured rate constants for interaction between dimethyl ferrocene and LiI. the order of activity for dyes was OsN3 > $OsCl_2$ > OsI_2. This type of analysis could be applied to DSSC type systems to evaluate potential redox shuttles or to solar fuels schemes to evaluate dye and catalyst activity and selectivity.

Procedures

Reagents and Chemicals

All chemicals were purchased and used without further purification unless stated otherwise. For spectroelectrochemical experiments and laser spectroscopy studies the following reagents were used: acetonitrile (ACS/HPLC 99.9%, Honeywell Burdick & Jackson), methanol (certified ACS 99.9%, Fisher Chemical), lithium perchlorate (battery grade 99.99%, Aldrich), Alconox powdered precision cleaner (Alconox), lithium hydroxide (laboratory grade anhydrous, Fisher Scientific), lithium iodide (99%, anhydrous, Acros Organics).

General Electrochemical Procedures

Three-electrode electrochemical measurements were performed using a Bio-Logic VSP-300 potentiostat in grounded mode using a dyed TiO_2 working electrode, an aqueous LiCl-saturated SCE reference electrode, and a platinum mesh counter electrode. The three electrodes, a magnetic stir bar, and 14 ml of 100 mM $LiClO_4$ in acetonitrile were assembled into a 1 cm × 1 cm custom borosilicate glass spectroelectrochemical cuvette which was placed in an Agilent Cary 60 Electronic Absorption Spectrophotometer. The cell was sealed and purged with argon

gas for 15 minutes prior to measurement. Stirring and argon bubbling continued during all electrochemical experiments.

Steady State Spectroelectrochemistry

Steady state spectroelectrochemistry was performed prior to cyclic voltammetry measurements as described in the previous chapter

Cyclic Voltammetry

After steady state spectroelectrochemistry, slides were relocated to an electrochemical beaker and 10 ml of 100 mM $LiClO_4$ in acetonitrile was added as supporting electrolyte. The working electrode was is moved as close as possible, ~3 mm, to the reference electrode frit. An initial 30 second open circuit potential measurement was performed to ensure that the cell was set-up correctly. An EIS measurement was performed with a center voltage of 0 V vs open circuit potential, a sinusoidal amplitude of 10 mV, a frequency range 7 MHz to 2 Hz using logarithmic spacing with 6 points per decade. This was followed by cyclic voltammetry measurements with scan limits of 0.75 V and –0.25 V versus reference and scan rates of 5, 2, 1, 0.5, 0.2, and 0.1 V/s, performing two scans at each scan rate but only using the first for analysis. After all cyclic voltammetry scan are complete, a second EIS measurement was performed.

Substrate Additions

Substrate solutions containing either 100 mM LiI or 50 mM dmFc + 100 mM $LiClO_4$ in acetonitrile were prepared. After cyclic voltammetry measurements were performed in the absence of substrate, substrate solution was injected such that a total volume of 0.101 ml, 0.204 ml, 0.526 ml, 1.111 ml, 2.500 ml, and 10.00 ml was injected for substrate measurements 1, 2,

3, 4, 5, and 6 respectively. After each injection cyclic voltammetry was performed again as described above.

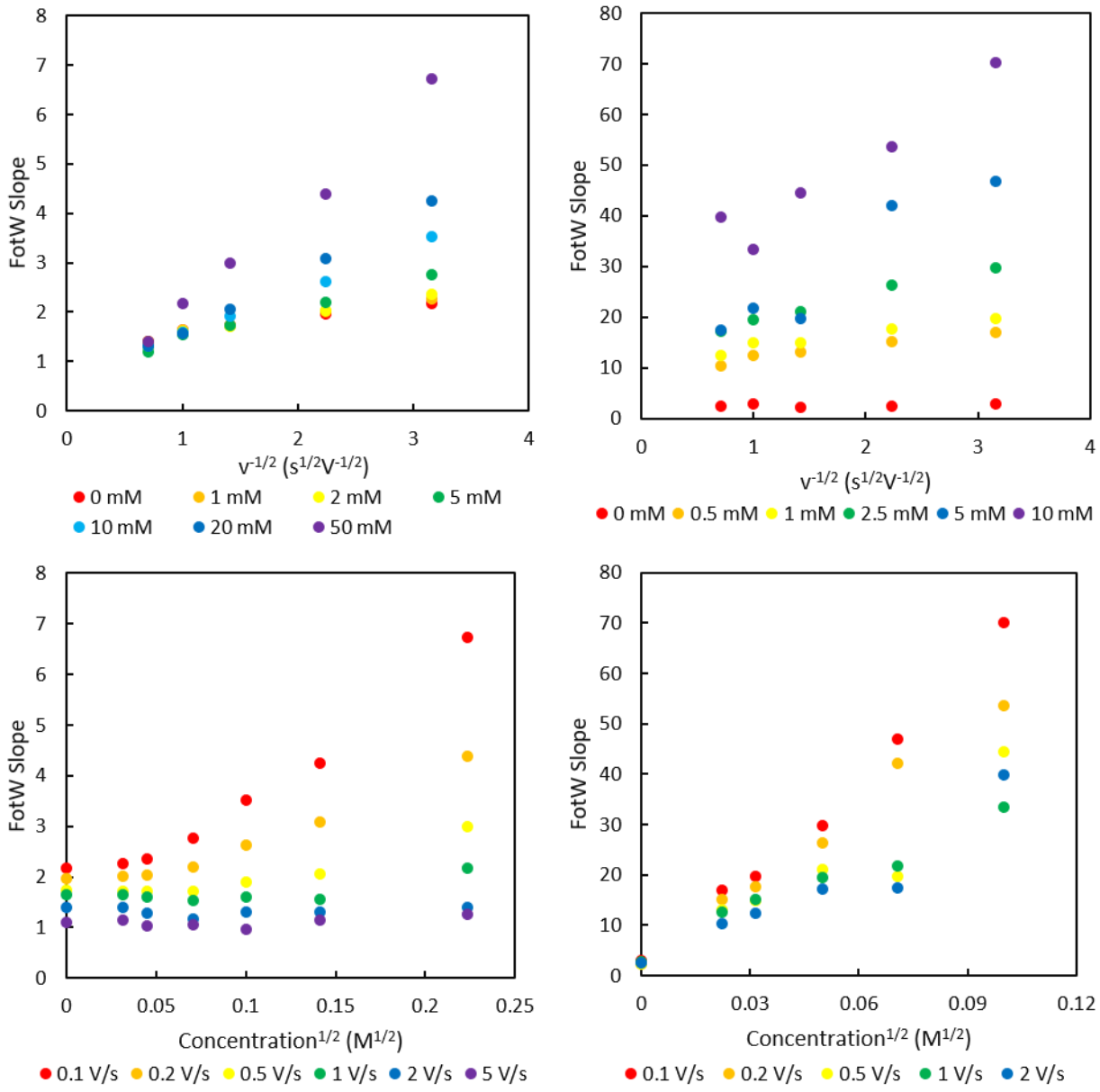

Figure 37: FotW slope of OsN3 dyed TiO_2 mesoporous films on FTO glass in 100 mM $LiClO_4$ solution in acetonitrile as a function of the square root of inverse scan rate and the square root of substrate concentration. Left: LiI as substrate. Right: dmFc as substrate.

All four graphs in

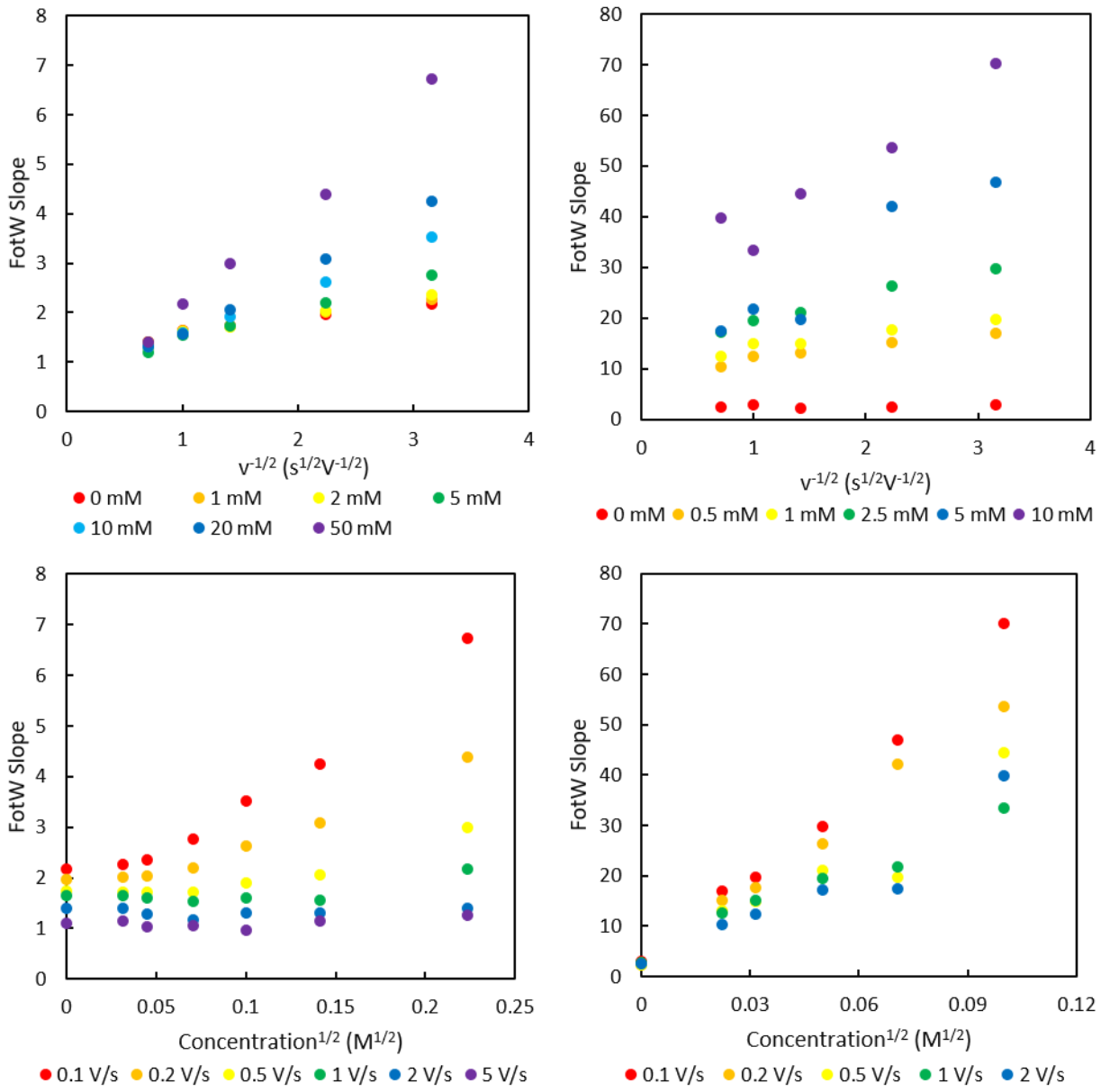

Figure 37 show approximately linear behavior as would be expected by FotW analysis. Only the FotW slope as a function of the square root of inverse scan rate with LiI substrate demonstrates an intercept close to zero as would be expected. FotW slope as a function of the square root of substrate concentration for both LiI and dmFc substrates intercept the y-axis at values between 1 and 2. This is because the FotW relationship assumes that substrate concentration is larger

relative to catalyst concentration and so current is primarily due to catalysis of substrate and current due to oxidation of catalyst is negligible. In our system, the dye concentration on the film is close to 200 mM, which is larger than all substrate concentrations measured. This causes its contribution to current and FotW slope to be nonzero. Because all currents are normalized by the peak current of the dye in absence of substrate, the minimum slope of FotW graphs, even in the absence of substrate is 1. The reason for the nonzero intercept for FotW slope as a function of the square root of inverse scan rate for dmFc substrate is unclear.

Nanosecond Transient Microwave Conductivity and Nanosecond Transient Absorption Measurements of Dye-Sensitized Solar Cells Containing Liquid Redox Electrolyte

Introduction

For an n-type DSSC to function, there are several conditions that need to be met.[1,18,29,89]

(1) Dyes must inject electrons into the semiconductor support when it excited by light.

(2) Injected electrons must not recombine with oxidized dyes before diffusing to the electrode contact.

(3) Oxidized dyes must be regenerated by the redox shuttle before recombining with injected electrons.

(4) Injected electrons must not shunt to oxidized redox shuttle.

(5) Excited dyes must not shunt to oxidized redox shuttle.

A powerful tool set for resolving these processes is time resolved pulsed laser spectroscopy. Under normal operating conditions, DSSCs are continuously illuminated so excitation, injection, regeneration, and shunting also occur continuously, quickly reaching a steady state that cannot easily measured or deciphered beyond a net current and voltage. Pulsed laser spectroscopy simplifies the process by delivering light in a short pulse so all excitation occurs at approximately the same time. By probing the system at different times after the pulse, kinetic information about subsequent processes can be determined. The two types of pulsed laser

spectroscopy discussed in this chapter are nanosecond transient absorption (nsTA) and nanosecond transient microwave conductivity (TrMC).

For nanosecond transient absorption, samples were excited with an Nd-YAG laser passed through a doubling crystal to achieve its second harmonic wavelength of 532 nm. Excitation and subsequent processes cause a change in the absorption spectra of the film of the due to the generation of new species. These changes were probed continuously by illuminating samples with a xenon arc lamp and selecting a single wavelength with a monochromator and filter wheel. The signals were measured by a PMT and digitized by an oscilloscope with 0.2 ns time resolution. By sweeping the wavelength selected by the monochromator, absorption kinetics across the entire visible region could be measured. The change in absorption can be compared with the difference in absorption between oxidized and reduced dye, redox shuttle, and semiconductor to determine which species are present at each point in time.[90] nsTA is most sensitive species with large changes in absorption such as oxidized and reduced dye and least sensitive to species with a small change in absorption such as neutral and negatively charged TiO_2.

For transient microwave conductivity, samples were excited with an Nd-YAG laser passed through a doubling crystal to achieve its second harmonic wavelength of 532 nm. Excitation and subsequent injection increase the number of mobile electrons in the TiO_2 conduction band. These electrons are probed continuously by microwave reflection. Microwaves interact with and reflect from mobile charge carriers. The difference in reflected microwaves after the laser pulse is proportional to sum of the mobilities of generated charge carriers.[91] The technique is most sensitive to highly mobile electrons in TiO_2 and less sensitive to ions. The difference in sensitivity is so drastic that the TrMC signal can be considered to be exclusively

due to electrons in the TiO_2 conduction band in most cases.[92,93] This makes TrMC a good complimentary technique to nsTA which is least sensitive to electrons and most sensitive to dyes and redox shuttle.

Results and Discussion: Injection and Recombination Lifetime

To determine if dyes inject into TiO_2, nanosecond transient absorption and TrMC were performed on dyed TiO_2 films in the presence of 100 mM $LiClO_4$ electrolyte solution. $LiClO_4$ is an electrochemically inert salt that cannot regenerate the dye or cause shunting.[94] The only processes that could occur after excitation are injection and TiO_2 electron to oxidized dye recombination. Li^+ ion has also been shown to promote electron injection by adsorbing to and intercalating into TiO_2 and lowering the TiO_2 conduction band edge.[95] Transient absorption full spectra of RuN3, OsN3, OsI_2, and $OsCl_2$ dyes with overlaid difference spectra are shown in **Figure 38**.

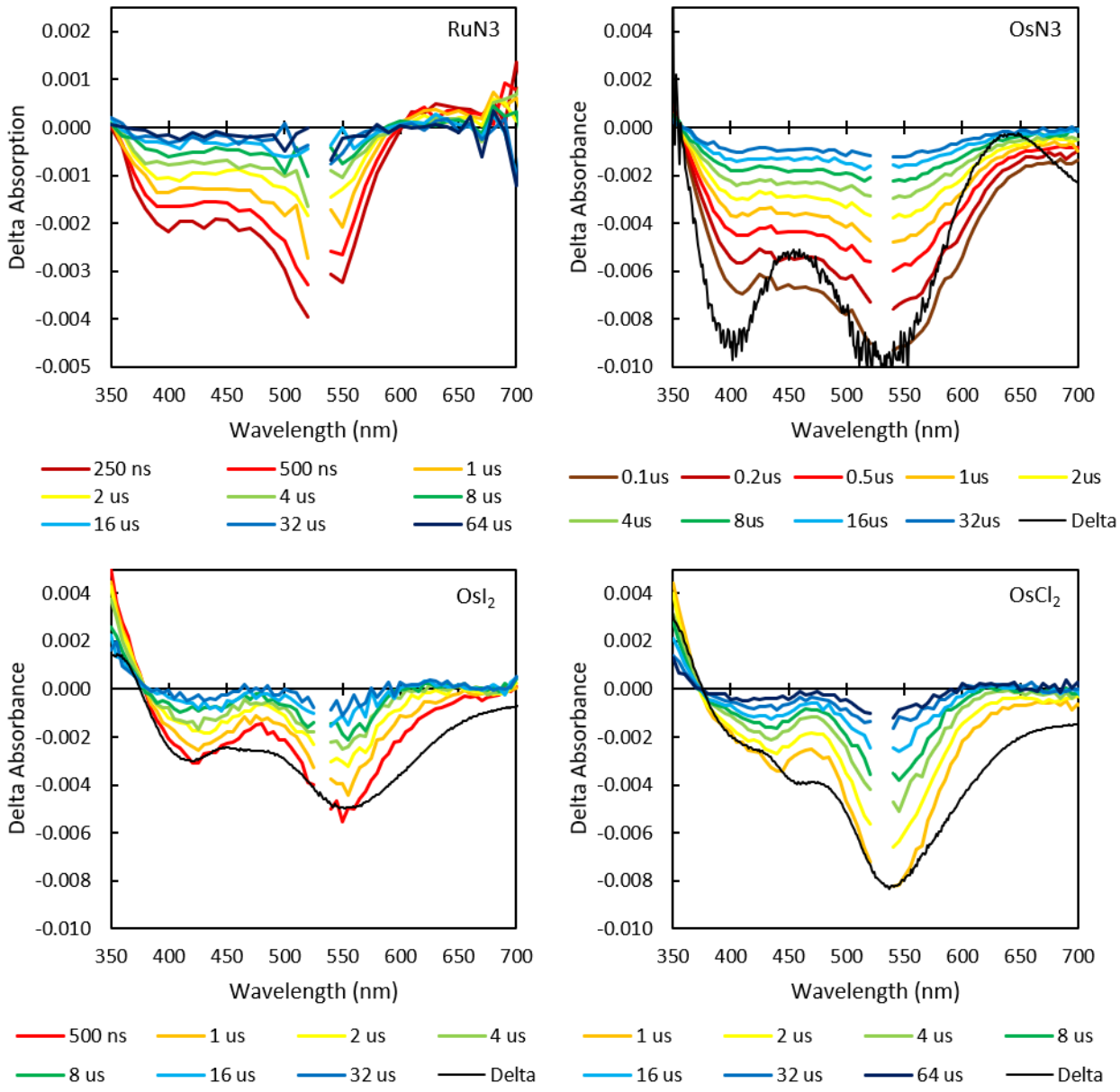

Figure 38: Nanosecond transient absorption spectra showing change in absorbance as a function of wavelength at various times after excitation of dyed TiO_2 mesoporous films in 100 mM $LiClO_4$ solution in acetonitrile with overlaid delta absorption spectra obtained via spectroelectrochemistry (black). Upper left: RuN3 dye with no delta absorption spectrum. Upper right: OsN3. Lower left: OsI_2. Lower right: $OsCl_2$.

The transient absorption spectra in **Figure 38** show a bleach in the two metal-to-ligand charge transfer bands in the 350 to 700 nm region demonstrated by all dyes discussed in this thesis. The spectra of RuN3 and OsN3 match those previously reported under similar conditions in both spectrum and kinetics.[41,96] The transient absorption spectra also generally match the delta

spectra obtained by spectroelectrochemistry which suggests that excited dyes inject into TiO_2 generating oxidized dyes. The differences between the delta spectra and the transient absorption spectra are due to several differences between the two conditions. Under transient absorption conditions there are excess electrons present in the conduction band which would stark shift the dye absorption spectra[97–99] and contribute a positive change in absorbance at wavelengths longer than 400 nm.[100] This is consistent with the positive shift in the transient absorption spectrum relative to the delta spectrum seen for all dyes around 700 nm. Under spectroelectrochemical conditions there is a deficit of electrons in the TiO_2 conduction band which would cause an opposite stark shift of that seen in the transient absorption spectrum, slightly changing the absorption spectrum. It is safe to conclude that injection occurred even though the spectra do not match perfectly, fulfilling criterion (1) in the chapter introduction.

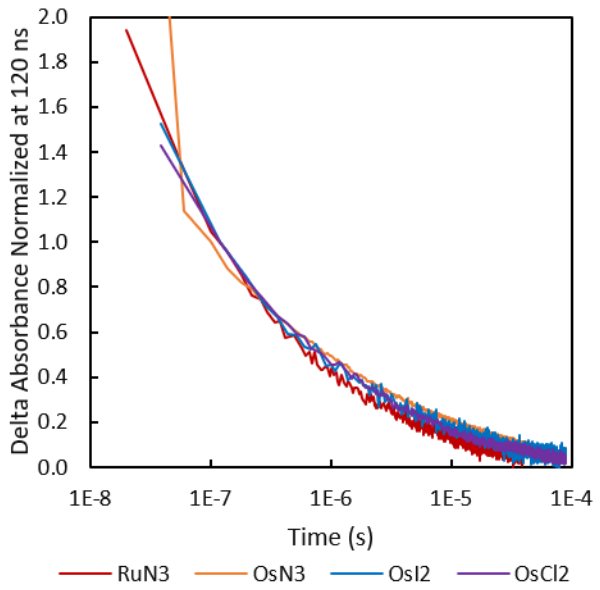

Figure 39: Nanosecond transient absorption spectra of RuN3 (red), OsN3 (orange), OsI_2 (blue), and $OsCl_2$ (purple) showing change in absorbance at 560 nm normalized at 120 ns as a function of time at various times after excitation of dyed TiO_2 mesoporous films in 100 mM $LiClO_4$ solution in acetonitrile.

Single wavelength kinetics of transient absorption measurements in $LiClO_4$ electrolyte are shown in **Figure 39**. All dyes showed very similar decay rates. OsN3 displayed the slowest

decay rate, $OsCl_2$ and OsI_2 displayed equal intermediate decay rates, and RuN3 showed the fastest decay. This decay is the recombination of electrons in TiO_2 to oxidized dye. RuN3 is known to produce solar cells with very high quantum yields[40] so any dye with a slower recombination rate should also be capable of high charge collection rates, fulfilling criterion (2) in the chapter introduction.

Results and Discussion: RuN3 Control Dye

RuN3 was used as a control dye to demonstrate nsTA and TrMC results on a dye that quickly regenerates and does not shunt. nsTA and TrMC measurements were performed on RuN3 dye in the electrolyte solution most commonly used by Nate Lewis's group in complete solar cells that contains LiI, LiI_3, trifluoroacetic acid (TFA), 4-*tert*-butylpyridine (TBP), valeronitrile, and acetonitrile. abbreviated as "Lewis electrolyte". Full spectrum transient absorption data and single wavelength kinetics under these conditions are shown in **Figure 40**.

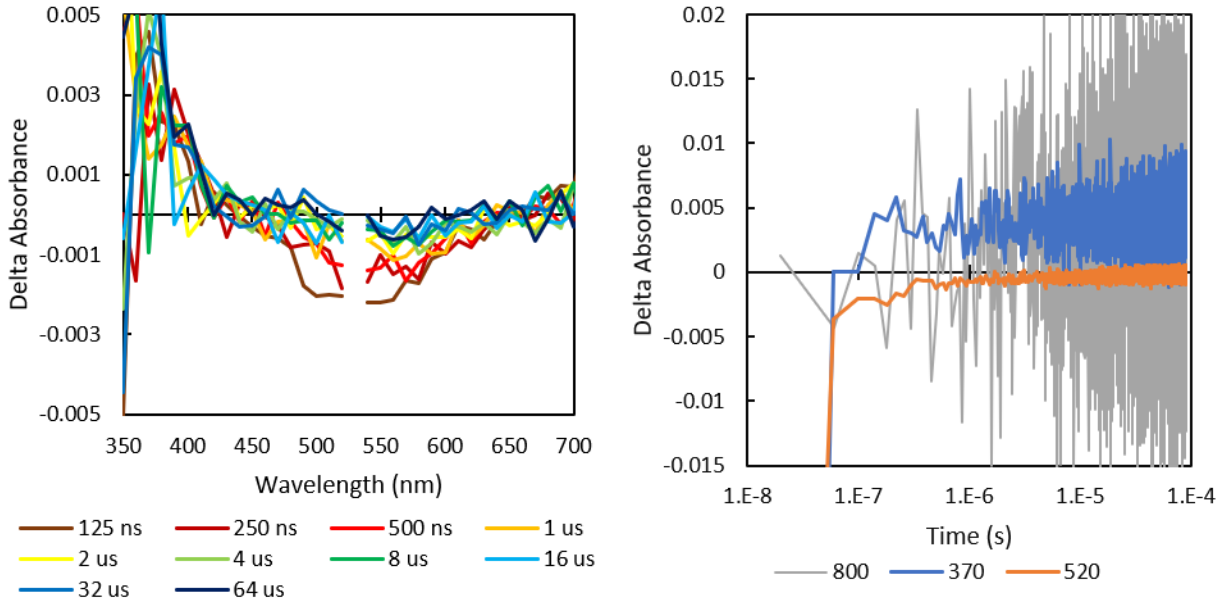

Figure 40: Nanosecond transient absorption spectroscopy of RuN3 dye on a mesoporous TiO_2 film with Lewis electrolyte containing 0.46 M LiI, 0.04 M LiI_3, 0.02 M TFA, and 0.07 M TBP solution in 85:15 v/v acetonitrile:valeronitrile. Left: delta absorbance as a function of wavelength at various times after excitation. Right: delta absorbance as a function of time at select wavelengths.

The full spectrum nsTA measurement of RuN3 in Lewis electrolyte differs from the full spectrum nsTA measurement of RuN3 in $LiClO_4$. Kinetics at 520-560 nm, the peak dye bleach, show a similar decay to baseline in both spectra, suggesting that dyes inject, are oxidized, and then reduced to their original form. In the presence of Lewis electrolyte, a growth appeared at 350-400 nm that overcame the initial dye bleach during the first 500 ns and then persisted for the duration of the measurement. This is consistent with the appearance of oxidized iodide species $I_2^{\cdot-}$ or I_3^-. The growth at 800 nm indicative of electrons in TiO_2 also persists for the duration of the Lewis electrolyte experiment. This suggests that electrons in TiO_2 have a longer lifetime than the oxidized dyes, indicating that dyes are reduced by electrolyte instead of electrons in TiO_2 and that recombination is between electrons in TiO_2 and oxidized electrolyte, which is slower than recombination to oxidized dye.

To better support these conclusions, nsTA and TrMC were performed on RuN3 dyed TiO_2 films with 100 mM LiI_3 solution in acetonitrile and 100 mM LiI solution in acetonitrile. The nsTA and TrMC spectra of RuN3 with LiI_3 solution are shown in **Figure 41**.

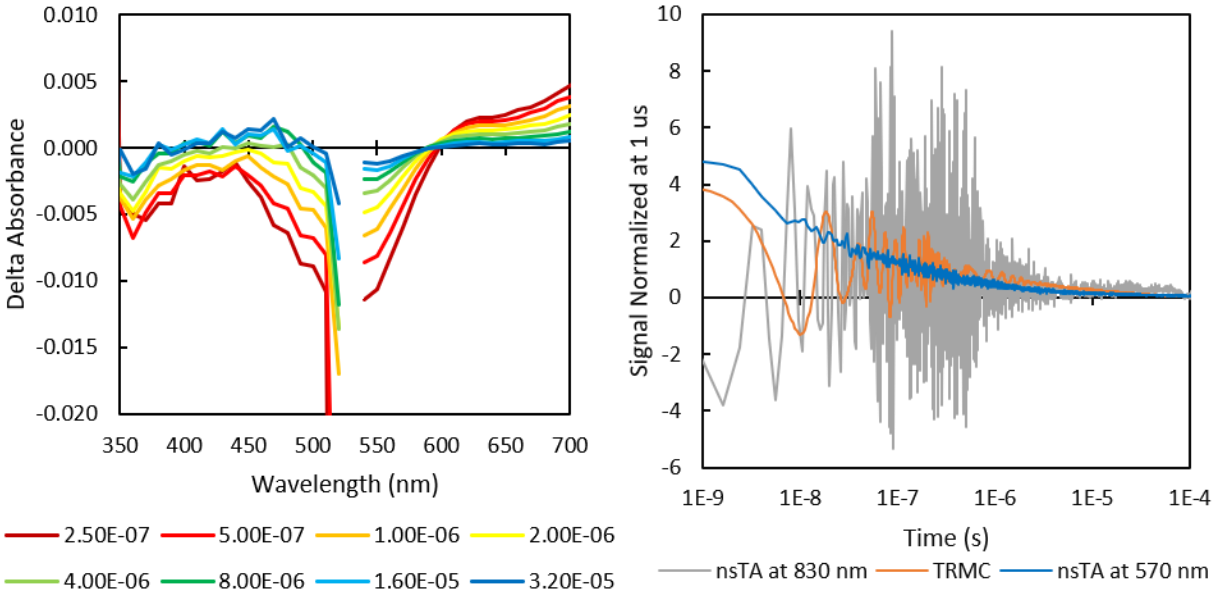

Figure 41: Nanosecond transient absorption spectroscopy of RuN3 dye on a mesoporous TiO_2 film with LiI_3 100 mM solution in acetonitrile. Left: delta absorbance as a function of wavelength at various times after excitation. Right: normalized delta absorbance at select wavelengths and normalized TrMC signal as a function of time.

The nsTA spectrum of RuN3 in the presence of 100 mM LiI is similar to the nsTA spectrum of RuN3 in the presence of 100 mM $LiClO_4$ in shape and decay kinetics, suggesting that the primary pathway, injection followed by recombination of electrons in TiO_2 to oxidized dyes, is the same in both cases. It is possible that some dye is regenerated by I_3^-, generating I_2, indicated by the growth at 400-500 nm and a slightly longer TrMC signal and TiO_2 electron signal at 830 nm compared to the oxidized dye signal at 570 nm. It does not appear that electron in TiO_2 shunt to LiI_3, a typically oxidizing agent, at a faster speed than they recombine to oxidized dye.

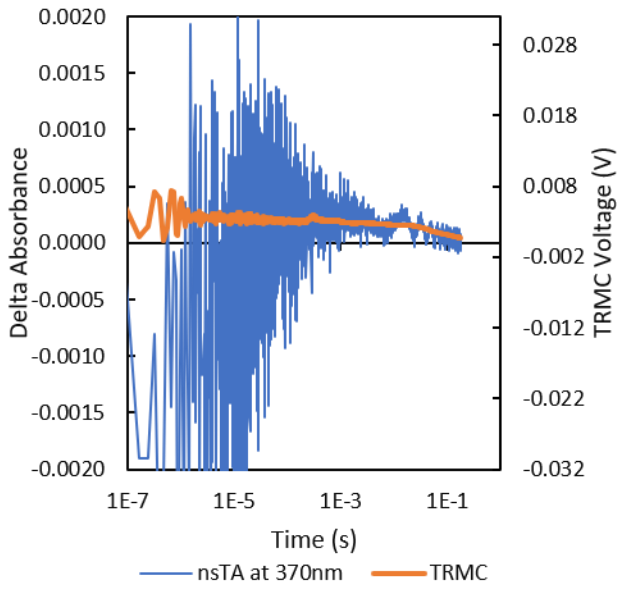

Figure 42: Overlaid nsTA at 370 nm (blue) and TrMC (orange) signals as a function of time of RuN3 dye on a mesoporous TiO_2 film with LiI_3 100 mM solution in acetonitrile.

Figure 42 contains a comparison of the nsTA signal at 370 nm and the TrMC signal of a RuN3 dyed TiO_2 film in 100 mM LiI solution in acetonitrile, a typically reducing environment. The nsTA signal starts as bleach, typical of oxidized dye, that transforms into a growth, typical

of the presence of oxidized iodide species. The decay of the oxidized iodide species can be overlaid with the decay of the TrMC signal which is indicative of the electrons in TiO_2 showing that these two processes have the same kinetics. This suggests that recombination of electrons in TiO_2 to oxidized redox shuttle is the primary recombination mode, although the exact mechanism is not determined. It may be direct recombination of the two species or it could be dye mediated, specifically ground state reduced dyes may be oxidized by the oxidized iodide species and then recombine with electrons in TiO_2. In either case, electron in TiO_2 to oxidized iodide recombination is approximately three orders of magnitude slower than electron in TiO_2 to oxidized dye recombination.

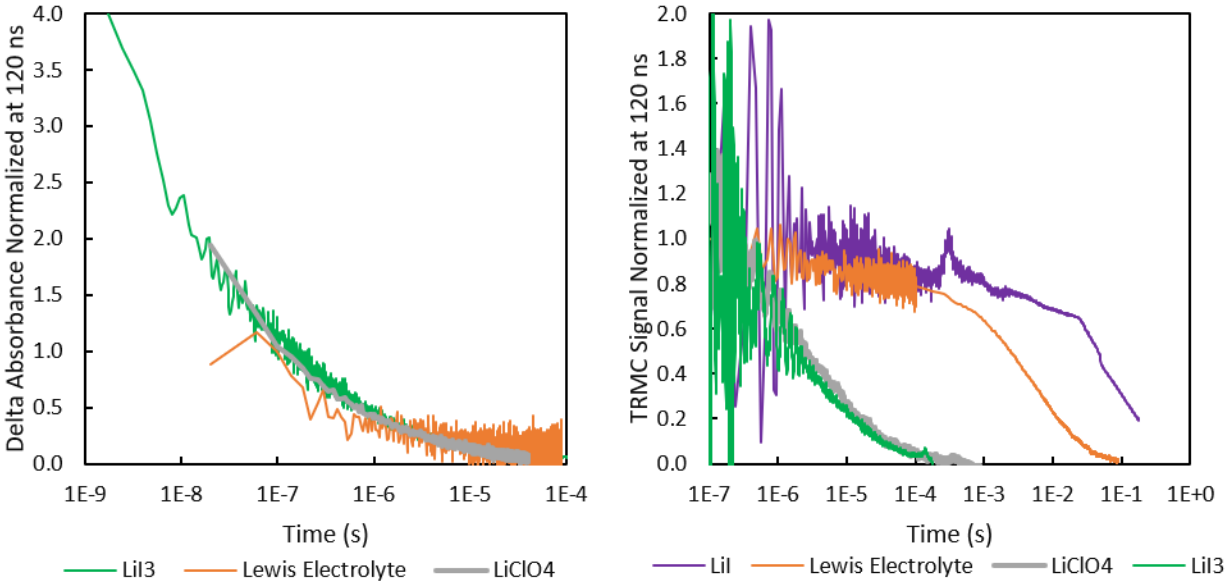

Figure 43: Kinetic plots of RuN3 dye on mesoporous TiO_2 in 100 mM LiI (purple), Lewis electrolyte (orange), 100 mM $LiClO_4$ (grey), and 100 mM LiI_3 (green) solutions in acetonitrile. Left: nsTA spectra showing normalized delta absorbance at 560 nm as a function of time. Right: TrMC spectra showing normalized response as a function of time.

The left plot of **Figure 43** compares the normalized delta absorbance at 560 nm of RuN3 dyed TiO_2 films which is indicative of oxidized dye under various electrolyte conditions. Regeneration by solution species is impossible for $LiClO_4$ solution so any solution with faster

decay kinetics would indicate regeneration is occurring. The decay kinetics for $LiClO_4$ 100 mM and LiI_3 100 mM solutions were almost identical, indicating that LiI_3 did not substantially regenerate oxidized dye as expected. Decay kinetics with Lewis electrolyte was mildly faster, showing that regeneration by Lewis electrolyte did occur, as expected.

The right plot of Figure 43 compares the transient microwave conductivity spectra of RuN3 dyed TiO_2 films indicative of the presence of injected electrons in TiO_2. The TrMC signals provided additional evidence to the nsTA data supporting the claim that injection occurred. In the presence of $LiClO_4$, the kinetics of electron in TiO_2 disappearance determined by TrMC match the kinetics of oxidized dye disappearance determined by nsTA. The only reaction pathway possible with $LiClO_4$ electrolyte is electron to dye recombination so this was expected. In the presence of LiI_3 the decay rate is only marginally faster than in the presence of $LiClO_4$, indicating that if shunting of electrons in TiO_2 to I_3^- does occur, it occurs only slightly. In the presence of LiI, the decay is approximately three orders of magnitude slower than in the presence of $LiClO_4$. This supports the earlier claim that dyes were regenerated by I^- and recombination of electrons in TiO_2 to I_3^- is slow. In the presence of Lewis electrolyte, the TrMC is ~2 orders of magnitude slower than in the presence of $LiClO_4$, but ~1 order of magnitude faster than in the presence of pure LiI. This provides mild support for the dye-mediated recombination hypothesis. It could be argued that the faster recombination of Lewis electrolyte compared to LiI is due to the presence of LiI_3 in Lewis electrolyte so recombination to I_3^- is faster. However, the TrMC decay kinetics of RuN3 with LiI_3 solution was only marginally faster than in the presence of LiI_3 so I_3^- is a poor electron acceptor from TiO_2 compared to oxidized dyes. The solution potential Lewis electrolyte is positive of the solution potential of a pure LiI solution so on average a greater proportion of dyes on the surface of a film will be oxidized in the presence of lewis

electrolyte than in the presence of LiI solution. If recombination is dye-mediated this would surely accelerate it.

Results and Discussion: OsN3

OsN3 is the osmium analogue of RuN3. They are structurally similar with a comparable excited state energy level, injection yield, and electron in TiO_2 to oxidized dye lifetime. The most noticeable difference between RuN3 and OsN3 is their difference in ground state formal reduction potential, 0.7-0.8 and 0.325 V vs SCE respectively. It is likely that the more negative ground state of OsN3 would cause it to regenerate more slowly than RuN3, leading to the poor performance of DSSCs with OsN3 and I^-/I_3^- redox shuttle. To investigate this hypothesis, nsTA and TrMC were performed on OsN3 dyed mesoporous TiO_2 thin films with 100 mM LiI and 100 mM LiI_3 solutions in acetonitrile as well as Lewis electrolyte.

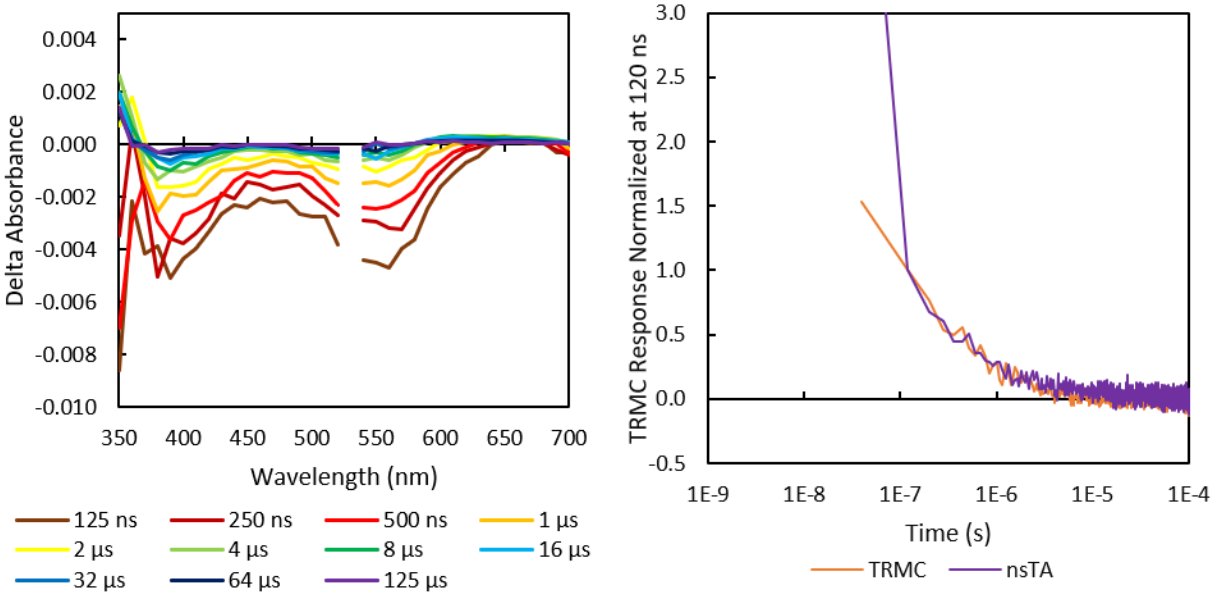

Figure 44: Nanosecond transient absorption spectroscopy of OsN3 dye on a mesoporous TiO_2 film with LiI 100 mM solution in acetonitrile. Left: delta absorbance as a function of wavelength at various times after excitation. Right: normalized delta absorbance at 560 nm and normalized TrMC signal as a function of time.

The nsTA spectrum of OsN3 with LiI 100 mM solution in acetonitrile shown on the left of **Figure 44** is very similar to the spectrum of OsN3 with $LiClO_4$ 100 mM solution in acetonitrile shown in the upper right of **Figure 38**, suggesting that similar processes are occurred under both conditions, specifically recombination between electrons in TiO_2 and oxidized dyes and an absence of dye regeneration. The nsTA spectrum of OsN3 with LiI solution lacks the growth at 370 nm indicative of dye reduction by I^-, forming $I_2^{\cdot-}$ and I_3^-, that can be seen in the nsTA spectrum of RuN3 dye with Lewis electrolyte shown in **Figure 40**. This supports a lack of OsN3 regeneration by I^-. The decay kinetics of electrons in TiO_2 shown by the TrMC spectrum on the right of **Figure 44** are identical to the decay kinetics of oxidized dye peak at 560 nm, suggesting that these two species disappear concurrently via electron in TiO_2 to oxidized dye recombination. While oxidized OsN3 regeneration by I^- is thermodynamically favored, it appears to be slower than recombination with electrons in TiO_2 and does not occur significantly.

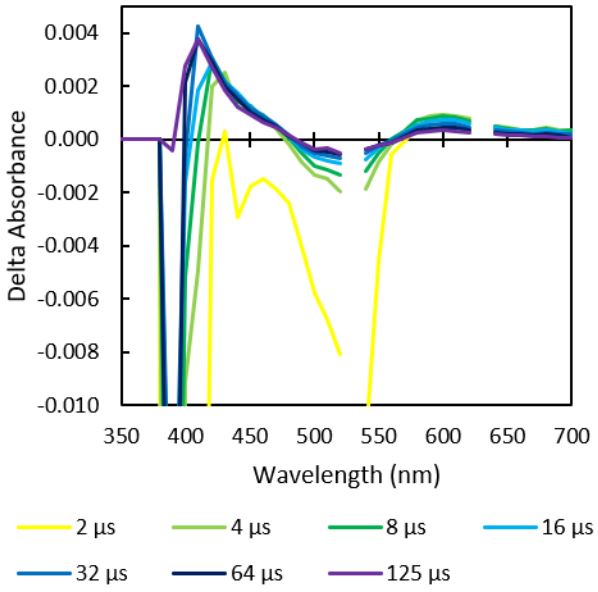

Figure 45: Nanosecond transient absorption spectroscopy of OsN3 dye on a mesoporous TiO_2 film with LiI 100 mM solution in acetonitrile showing delta absorbance as a function of wavelength at various times after excitation.

The nsTA spectrum of OsN3 with LiI_3 100 mM solution in acetonitrile shown in **Figure 45** is different from the nsTA spectra of OsN3 with $LiClO_4$ and LiI shown in **Figure 38** and **Figure 44**. The nsTA spectrum of OsN3 with LiI_3 shows growths from 400 to 475 nm and from 520 to 700 nm instead of a universal bleach. Additionally, the TrMC spectrum of OsN3 with LiI_3 shows no signal, suggesting that OsN3 either does not inject or electrons in TiO_2 have very short lifetimes below the resolution of our instrument under these conditions.

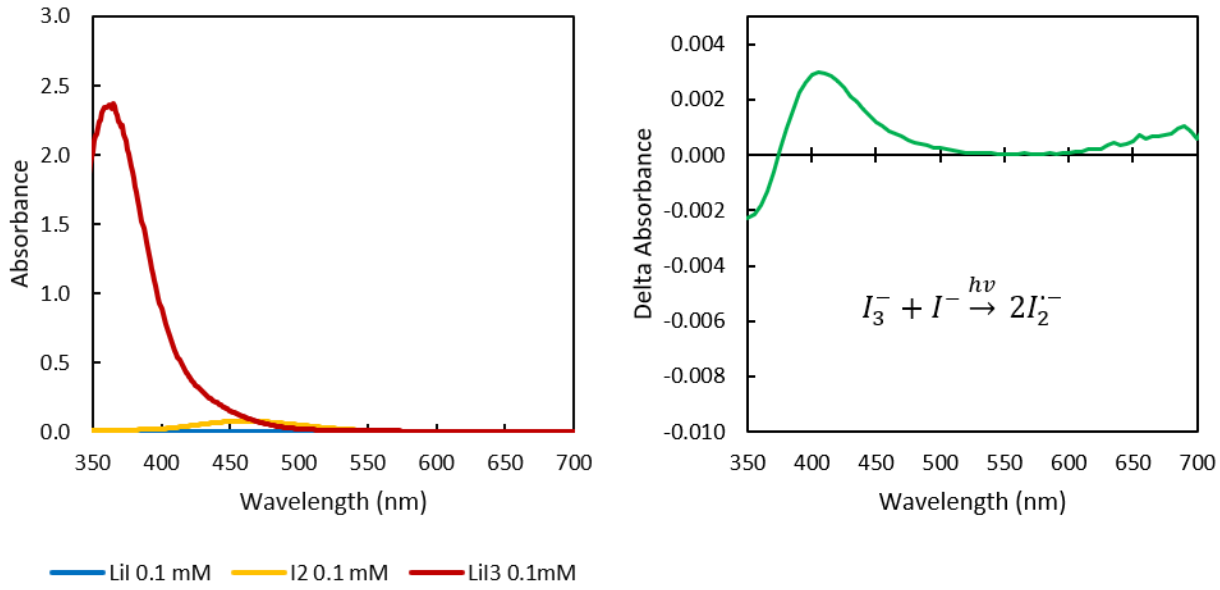

Figure 46: Left: UV-vis absorption spectrum of LiI, I_2, and LiI_3 0.1 mM solutions in acetonitrile in a 1 cm pathlength cuvette. Right: Transient absorption as a function of wavelength of a TBAI 0.1 mM + $TBAI_3$ 0.01 mM solution in acetonitrile at 500 ns with net chemical reaction inset.

To investigate the origin of the nsTA spectrum of OsN3 with LiI_3, absorption spectra of LiI, I_2, and LiI_3 solutions in acetonitrile were measured (**Figure 46** left). Consumption or production of any of these species could not explain growth at >520 nm of the nsTA spectrum of OsN3 with LiI_3 electrolyte because none of these species absorb at that wavelength. The graph on the right of **Figure 46** shows the nsTA spectrum of a mixture of TBAI and $TBAI_3$ in acetonitrile 500 ns after a laser pulse. This spectrum shows the difference in absorption caused by the conversion of I_3^- and I^- into two $I_2^{\cdot -}$.[101] A reasonable approximation of the nsTA spectrum

of OsN3 with LiI_3 can be made by a linear combination of nsTA spectrum of OsN3 with $LiClO_4$ (**Figure 38** upper right) and the nsTA spectrum of I_3^- excitation to produce $I_2^{\cdot -}$(**Figure 46** left). Several possible mechanisms could justify this. OsN3, when excited by light, may directly reduce I_3^- to I^- and $I_2^{\cdot -}$. OsN3 may inject, but the injected electron is rapidly scavenged by I_3^-, causing the same results. Concurrent excitation of both dye, which injects, and I_3^-, which dissociates, is unlikely because I_3^- excitation was not substantially observed in analogous experiments with RuN3, and no TrMC signal is observed which indicates electrons in TiO_2. Regardless of the mechanism, shunting occurs, which violates criterion (2) in the chapter introduction.

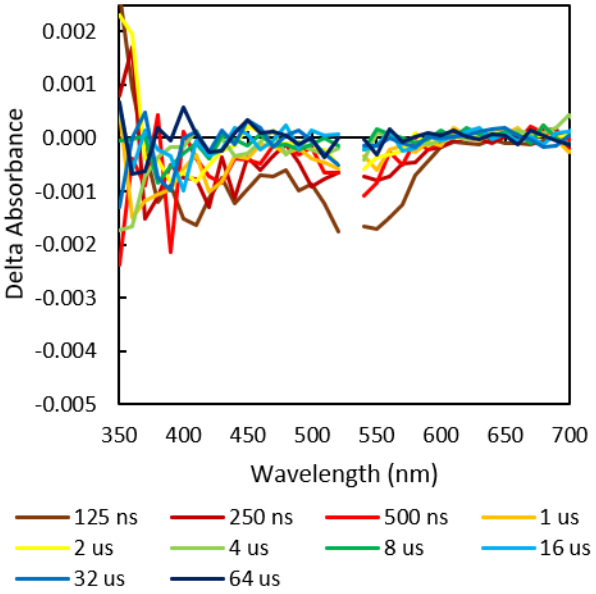

Figure 47: Nanosecond transient absorption spectroscopy of OsN3 dye on a mesoporous TiO_2 film with Lewis electrolyte containing 0.46 M LiI, 0.04 M LiI_3, 0.02 M TFA, and 0.07 M TBP solution in 85:15 v/v acetonitrile:valeronitrile. showing delta absorbance as a function of wavelength at various times after excitation.

The nsTA spectrum of OsN3 with Lewis electrolyte shown in **Figure 47** is remarkably similar to the nsTA spectrum of OsN3 with LiI shown in **Figure 44**. This suggests that either the presence of excess LiI or one of the additives, TFA or TBP, in Lewis electrolyte prevents the

shunting that occurs when only LiI_3 is present. No further investigation was done to determine which of these species prevented shunting.

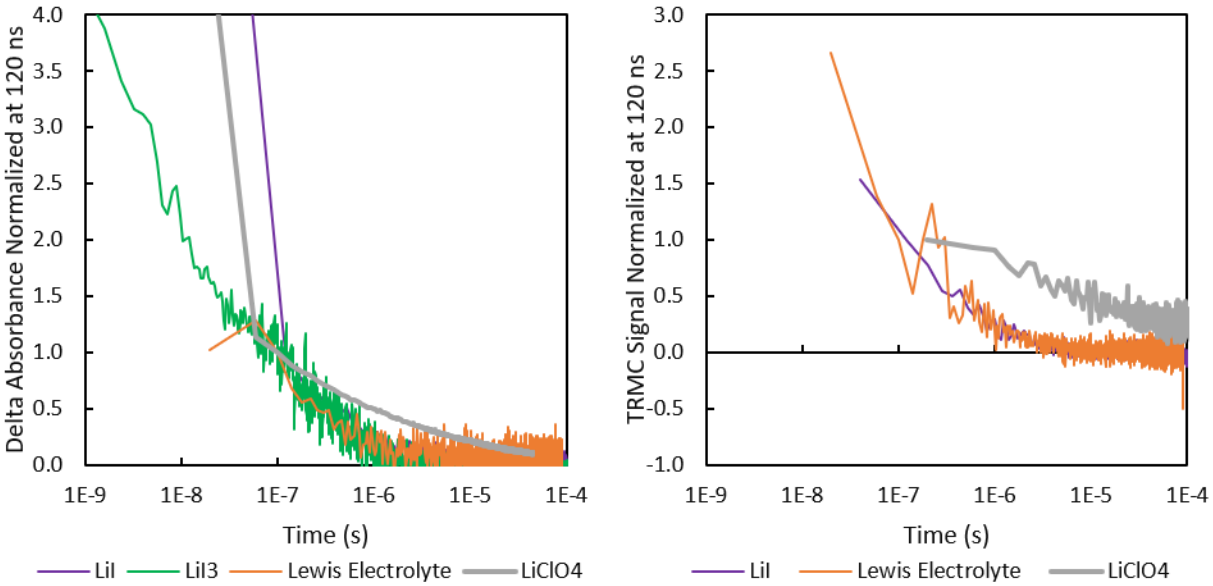

Figure 48: Kinetic plots of OsN3 dye on mesoporous TiO_2 in 100 mM LiI (purple), Lewis electrolyte (orange), 100 mM $LiClO_4$ (grey), and 100mM LiI_3 (green) solutions in acetonitrile. Left: nsTA spectra showing normalized delta absorbance at 560 nm as a function of time. Right: TrMC spectra showing normalized response as a function of time. TrMC for LiI_3 electrolyte is not graphed because it showed no signal.

Figure 48 compares the normalized delta absorbance at 560 nm of OsN3 dyed TiO_2 films which is indicative of oxidized dye under various electrolyte conditions. The decay kinetics for $LiClO_4$ 100 mM were the slowest of all measured conditions. Decay kinetics for LiI_3 100 mM, LiI_3 100 mM, and Lewis electrolyte solutions were almost identical. TrMC spectra indicative of electrons in TiO_2 of similar conditions matched the kinetics and trends showed in the nsTA spectra, with the exception of LiI_3 solution that showed no signal. This suggests that in the presence of $LiClO_4$, LiI, and Lewis electrolyte dye injection is followed predominantly by electron in TiO_2 to oxidized dye recombination and that regeneration is minimal. In the presence of LiI_3 and the absence of LiI, shunting occurs. It also appears that the presence of any iodide species speeds up recombination of electrons in TiO_2 to oxidized dye. These results explain the

poor performance of DSSCs with OsN3 dye, TiO_2 scaffold, and LiI/LiI_3 redox shuttle. While I^- is thermodynamically capable of regenerating oxidized OsN3, it does not occur fast enough to compete with electron in TiO_2 to oxidized dye recombination and so quantum yields for these solar cells are low.

Results and Discussion: $OsCl_2$

$OsCl_2$ has a narrower optical pseudo-bandgap and more negative ground state formal reduction potential than OsN3. DSSCs employing $OsCl_2$ with I^-/I_3^- electrolyte perform even more poorly than DSSCs employing OsN3 with I^-/I_3^- electrolyte. To determine if poor performance for $OsCl_2$ is due to slow regeneration kinetics, similar to OsN3, nsTA and TrMC were performed on $OsCl_2$ dyed mesoporous TiO_2 films with LiI 100 mM, and LiI_3 100 mM solutions in acetonitrile. Also, nsTA and TrMC were performed on $OsCl_2$ dyed films with dmFc 10 mM + $LiClO_4$ 100 mM solution in acetonitrile to see if a faster, 1-electron transfer species with similar formal reduction potential to I^-/I_3^- could regenerate the dye faster than I^-.

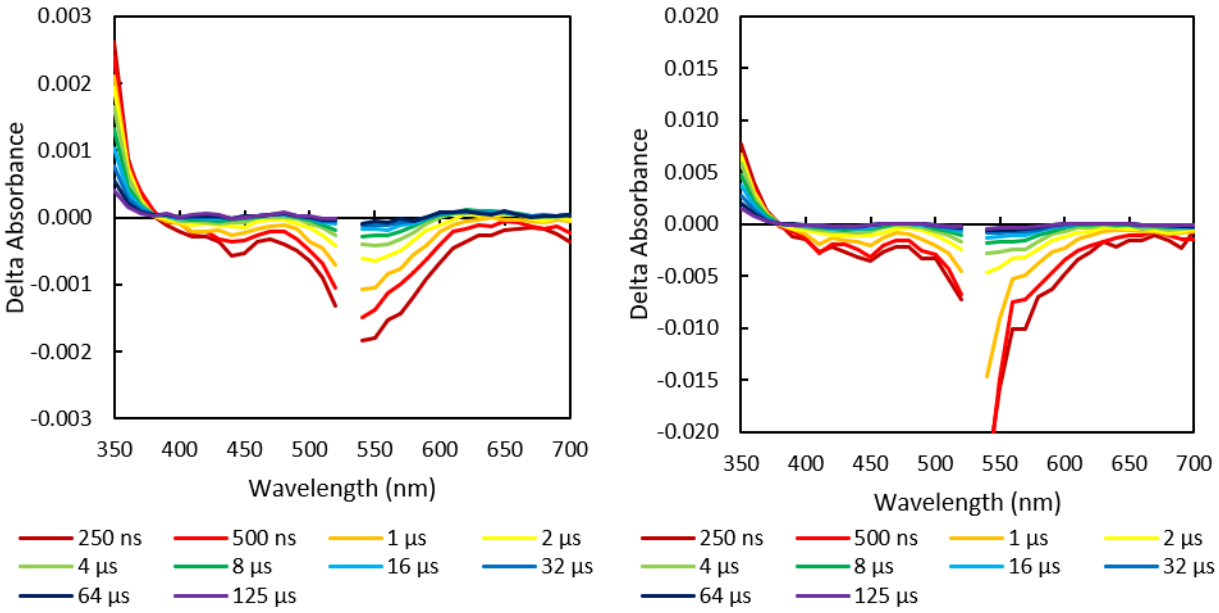

Figure 49: Nanosecond transient absorption spectroscopy of $OsCl_2$ dye on mesoporous TiO_2 films with LiI 100 mM solution (left) and dmFc 10 mM + $LiClO_4$ 100 mM solution (right) in acetonitrile showing delta absorbance as a function of wavelength at various times after excitation.

nsTA and TrMC measurements of $OsCl_2$ dye on TiO_2 films with LiI_3 100 mM solution failed to yield meaningful results due to the majority of $OsCl_2$ dyes existing in the oxidized state under these conditions. nsTA and TrMC of $OsCl_2$ dye on TiO_2 films with LiI 100 mM and dmFc 10 mM + $LiClO_4$ 100 mM solutions were more successful, yielding nsTA spectra shown in **Figure 49** that were very similar to the nsTA spectrum with $LiClO_4$ 100 mM shown in the lower right of **Figure 38**. No oxidized iodide species or 1,1'-dimethylferrocenium species were visible, suggesting that the predominant process was electron in TiO_2 to oxidized dye recombination and that regeneration was negligible.

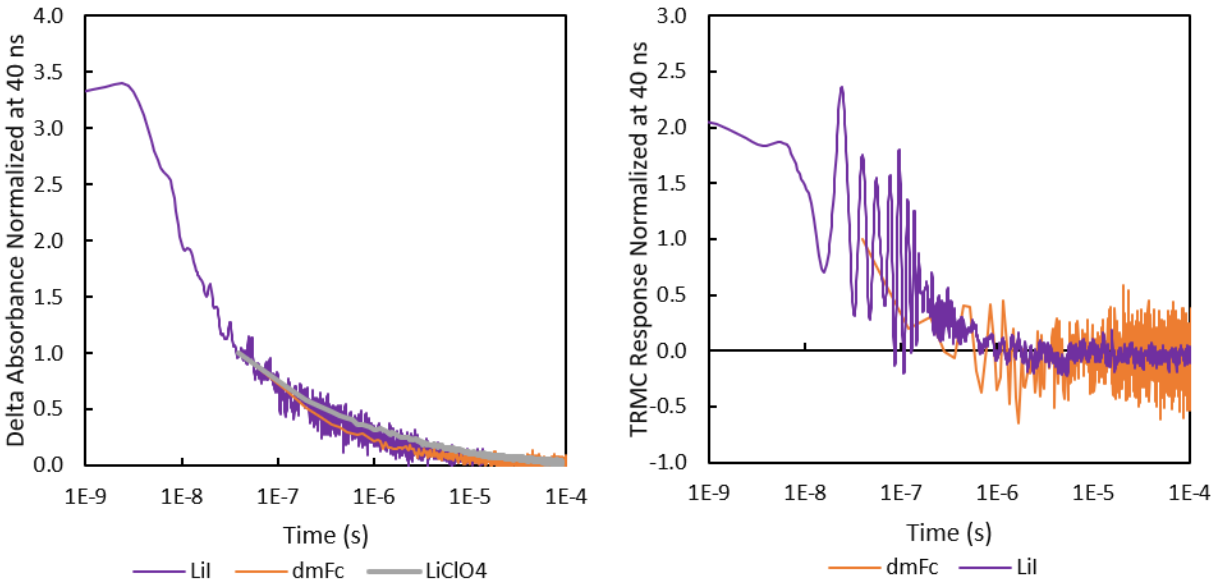

Figure 50: Kinetic plots of $OsCl_2$ dye on mesoporous TiO_2 in 100 mM LiI (purple), dmFc 10 mM + $LiClO_4$ 100 mM (orange), and 100 mM $LiClO_4$ (grey)solutions in acetonitrile. Left: nsTA spectra showing normalized delta absorbance at 560 nm as a function of time. Right: TrMC spectra showing normalized response as a function of time.

The nsTA kinetic traces at 560 nm, indicative of the presence of oxidized dye, of $OsCl_2$ dyed TiO_2 films demonstrated similar decay kinetics for all three measured solutions with $LiClO_4$ demonstrating the slowest kinetics and dmFc solution demonstrating the fastest kinetics. This suggests that either there is a slight amount of regeneration by dmFc and LiI or that recombination is faster due of the higher Fermi energy of the TiO_2 due to being in contact with more electron rich solutions. The TrMC traces, indicative of the presence of injected electron in the conduction band of TiO_2, for $OsCl_2$ dyed TiO_2 thin films for LiI and dmFc solutions were very similar and matched the kinetics of oxidized dye disappearance. This suggests that the predominant mode of oxidized dye reduction is by recombination with electrons in TiO_2. This result was expected for LiI, but was initially unexpected for dmFc. In retrospect, this result matches is consistent with the second order rate constant for oxidation of dmFc by oxidized $OsCl_2$ calculated by foot-of-the-wave analysis. Given a second order rate constant of 9,300 $M^{-1}s^{-}$

[1] and a dmFc concentration of 0.01 M, the resulting first order rate constant for dye regeneration would be expected to be 93 s^{-1} with a time constant of ~0.01 s. Considering that >90% of the dye has recombined by 0.0001 s, regeneration by dmFc 10 mM would be expected to be minor.

Conclusion

To better understand the fundamental electron transfer processes of mesoporous TiO_2 films sensitized with RuN3, OsN3, OsI_2, and $OsCl_2$ dyes, nanosecond transient absorption spectroscopy and nanosecond transient microwave conductivity measurements were performed on dyed TiO_2 films with supporting electrolyte containing $LiClO_4$ 100 mM, LiI 100 mM, LiI_3 100 mM, dmFc 10mM + $LiClO_4$ 100 mM, and full DSSC style "Lewis" electrolyte. All dyes were observed to inject electrons into the TiO_2 valence band with similar lifetimes evidenced by a bleach of the two metal to ligand charge transfer bands between 300 and 700 nm. RuN3 dye was efficiently regenerated by LiI solution resulting in electron in TiO_2 lifetimes, measured by TrMC, 4 orders of magnitude greater than in the absence of LiI, but did not demonstrate significant shunting to LiI_3 solution as would be expected of a high performing DSSC dye. OsN3 was not significantly regenerated by LiI and appeared to shunt to LiI_3 solution in the absence of excess LiI as would be expected of a poorly performing DSSC dye. $OsCl_2$ was not significantly regenerated by LiI or dmFc solutions, results were consistent with second order rate constant calculated by foot of the wave analysis.

Procedures

Sample Fabrication

For nsTA measurements using $LiClO_4$ 100 mM solution in acetonitrile, the slide preparation procedure was the same as the slide preparation procedure reported in the chapter photoelectrochemical characterization of infrared-absorbing osmium-polypyridyl dyes.

For TrMC measurements of OsN3 and RuN3 using $LiClO_4$ 100 mM solution, the slide preparation was the same as the procedure reported in the chapter photoelectrochemical characterization of infrared-absorbing osmium-polypyridyl dyes except that the slide dimensions were changed to 11 mm × 25 mm, the solvent was changed to propylene carbonate, and the measurement was performed of a wetted slide with a microscope glass coverslip (Fisherbrand Microscope Cover Glass #1).

For all other nsTA and TrMC measurements the slide preparation was the following:

Two 1 mm diameter holes were drilled into glass slides (Fisherbrand Plain Microscope Slides) of 11 mm × 25 mm × 1 mm dimensions 3 mm inset from opposite corners. Slides were sonicated in 5% wt aqueous Alconox solution for 15 min, rinsed with water and ethanol, sonicated in ethanol for 15 min, and rinsed with ethanol. TiO_2 paste was then applied to all but the upper and lower 2 mm of the glass slide using the doctor blade method with Scotch Magic Tape spacer and sintered in a box muffle furnace. The temperature was raised at a rate of 3 °C per minutes to 90 °C, held at 90 °C for 1 h, raised at a rate of 3 °C per minutes to 500 °C, held at 500 °C for 1 h, and then allowed to cool to room temperature. The thin film was then base-pretreated for 15 minutes in a pH 11 LiOH aqueous solution. The thin film was then immersed in a saturated dye solution[37] containing 3:1, v/v of acetonitrile and methanol for a minimum of 48 h. Dyed slides were soaked twice for 15 minutes each in acetonitrile to remove weakly bound dyes

and then 2 mm of dyed TiO_2 was removed by a Teflon coated razor blade from the right and left sides to make a dyed TiO_2 pane of 7 mm × 21 mm dimensions. A rectangular Surlyn window gasket (11 mm × 25 mm outer dimensions, 7 mm × 21 mm inner dimensions, Dysol 30 μm Surlyn Thermoplasic Sealant) was placed on the slide so that only exposed glass was covered. A microscope glass coverslip (11 mm × 25 mm, Fisherbrand Microscope Cover Glass #1) was placed over the Surlyn gasket and all components were secured by a pair of 0.5" binder clips. The assembly was placed into a preheated muffle furnace at 120 °C for 10 minutes to allow the Surlyn gasket to melt and seal the cell. The cells were allowed to cool for 10 minutes before removing the binder clips. Electrolyte solution was introduced via glass pipette into one of the two drilled holes. The two holes were plugged with parafilm, cleaned with a kimwipe, painted with a thin layer of UV-curable clear gel nail polish (Lina UV topcoat or ibd Hard Gel), and capped with microscope glass coverslips (3 mm × 3 mm, Fisherbrand Microscope Cover Glass #1). The nail polish was cured under UV light (HWAWTS Ultrafire) for thirty seconds. nsTA and TrMC Measurements were performed the same day. nsTA measurements were performed with the device at a 45° angle to the pump and probe beams such that neither the pump or probe was reflected into the monochromator.

nsTA

nsTA measurements were performed using the same procedure reported in the chapter photoelectrochemical characterization of infrared-absorbing osmium-polypyridyl dyes, but with the following modifications: For all dyed thin film samples except OsN3 with 100 mM $LiClO_4$ solution in acetonitrile, laser power was 1.5 mJ per pulse. The timescale of many experiments was increased with a maximum sampling rate of 250 kilosamples. For the TBAI 1 mM + $TBAI_3$

0.01 mM solution in acetonitrile, the excitation wavelength was changed to 355 nm by frequency tripling the fundamental Nd-Yag harmonic and the excitation power was 0.7 mJ per pulse.

TrMC

Microwaves were generated by a temperature-regulated X band voltage-controlled oscillator (Sivers IMA, VO3262X/00) tuned by a programmable power supply (Kiethley) and carried by a coaxial cable to a power splitter (Mini-Circuits, ZX10-2-126+) which divided the power evenly between the sample and reference arms of the device.

On the sample arm of the device, a coaxial cable carries the signal from the power splitter to an antenna inside a waveguide. The microwaves pass through an isolator (RF-Lambda, RFWI90F) and a variable attenuator (L3 Narda-ATM, 90-AF620A-10-6-6) typically set at 3 dB attenuation. The microwaves pass through a WR-90 3-port circulator (Waveline, 625-13) to a waveguide switch (Waveline, 678-E) which passes the microwaves to either the sample cavity or a copper plate. The microwaves reflect off the sample or copper plate, returning through the waveguide switch to the 3-port circulator and pass through a second isolator to a second waveguide switch which passes the microwaves either to a power meter (Rohde&Schwarz, NRP18T) or to an antenna which connects to a double balanced frequency mixer via a coaxial cable to be compared with the unperturbed reference arm signal.

On the reference arm of the device the signal passes through a coaxial cable to a voltage-controlled phase shifter (RF-Lambda, RVPT0818GBC) driven by a programmable power supply (Kiethley). The signal is amplified (Mini-Circuits, ZJL-153+) and then attenuated (Mini-Circuits, FW-X+) to best match the double balanced frequency mixer. The frequency mixer generates sum and difference frequencies of the reference and sample arms. The sum frequency is 16-24 GHz,

which is too fast for the 2.5GHz oscilloscope to detect. The difference frequency is the transient signal induced by the laser pulse. The oscilloscope acquisition is triggered off of a silicon diode which detects laser scatter in the same way as the nsTA system.

The sample was placed in a house-built resonant sample cavity at ¼ distance from the iris restricting microwave entry from the rest of the system to the laser grid which is transparent to visible light but totally reflects microwaves. The first switch was turned to the copper plate and the second switch was turned towards the power meter. The voltage applied to the voltage-controlled oscillator was swept across to generate the frequency range of interest and the power reflected from the copper plate was measured.

The first switch was then turned to the sample cavity and the frequency range swept again while measuring power. The reflected power spectrum of the sample cavity was divided by the reflected power spectrum of the copper plate to generate the resonance curve of the sample cavity which demonstrates a characteristic minimum at a frequency where the microwaves wavelength is equal to the cavity length. The voltage-controlled oscillator is set to generate microwaves at this frequency for the remainder of the measurement.

The second switch was then turned to the frequency mixer. The voltage applied to the phase shifter was swept to change the phase of the reference arm microwaves with respect to the signal arm microwaves and the signal amplitude and standard deviation were measured by the oscilloscope. Ideally the standard deviation would achieve a minimum when the signal amplitude was at a maximum or minimum value, although this was not always the true due to imperfect power matching of the signal and reference arms at the frequency mixer. In the case of a discrepancy, the phase shift that generated minimum noise was selected for the remainder of the measurement.

The oscilloscope acquisition was set to trigger off the silicon diode and the laser began firing. The sample cavity was blocked so that laser could not reach the sample. 7000 shots were averaged to collect a dark measurement.

The block was removed, and the laser was allowed to reach the sample. 7000 shots were averaged to collect a laser measurement.

The dark measurement was subtracted from the laser measurement to remove background electromagnetic signals. The resulting data was baselined so that the pretrigger average was equal to zero and averaged to 2500 points using either logarithmic or linear averaging.

An example data workup is shown below in **Figure 51**, **Figure 52**, and **Figure 53**.

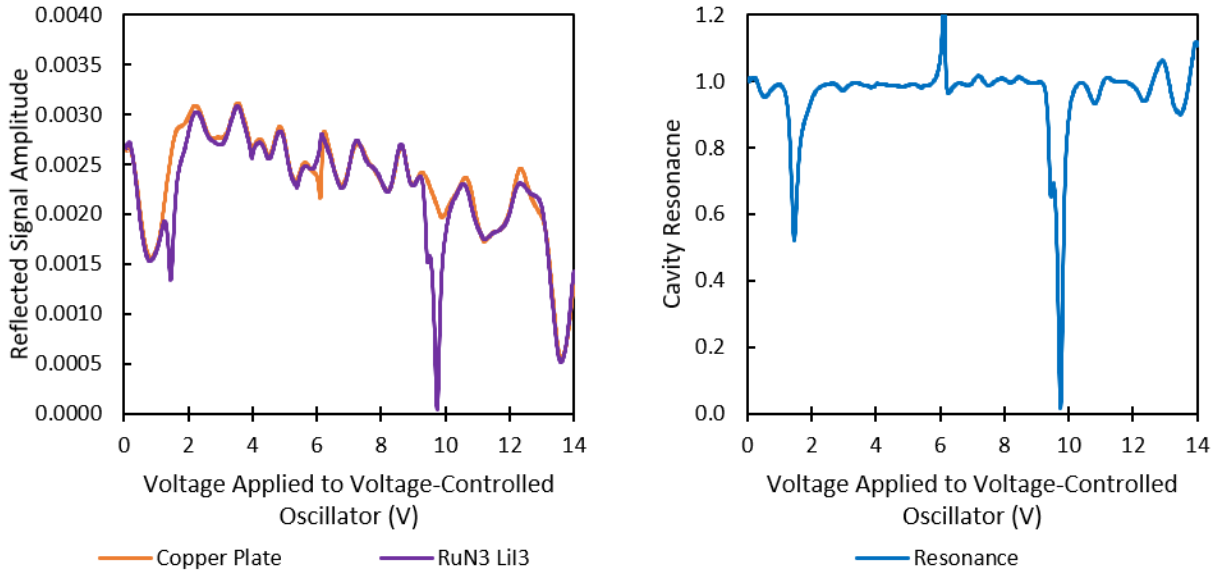

Figure 51: Steady state X band microwave measurements of a RuN3 dyed mesoporous TiO_2 film with LiI_3 100 mM electrolyte. Left: microwave power spectra showing reflected signal amplitude in arbitrary units as a function of applied voltage of a totally reflective copper plate (orange) and a the resonant sample cavity (purple). Right: The sample cavity resonance spectrum generated from the power spectra on the left. The resonance at 1.5 V is the useful microwave mode where one wavelength is equal to the effective cavity length. The resonance at 9.7 V is a non-useful microwave mode. The anti-resonance at 6 V is a system artefact.

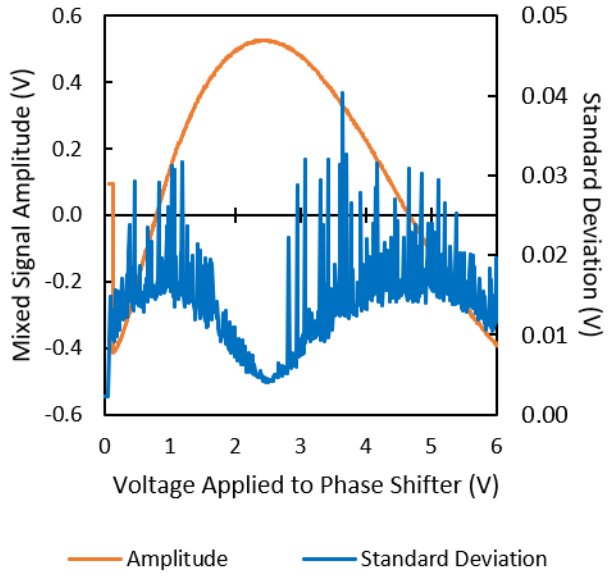

Figure 52: Steady state X band microwave measurements of a RuN3 dyed mesoporous TiO_2 film with LiI_3 100 mM electrolyte at the resonant frequency showing signal amplitude (orange) and standard deviation (blue) as a function of voltage applied to the phase shifter. The minimum noise occurs 50 mV positive of the peak signal.

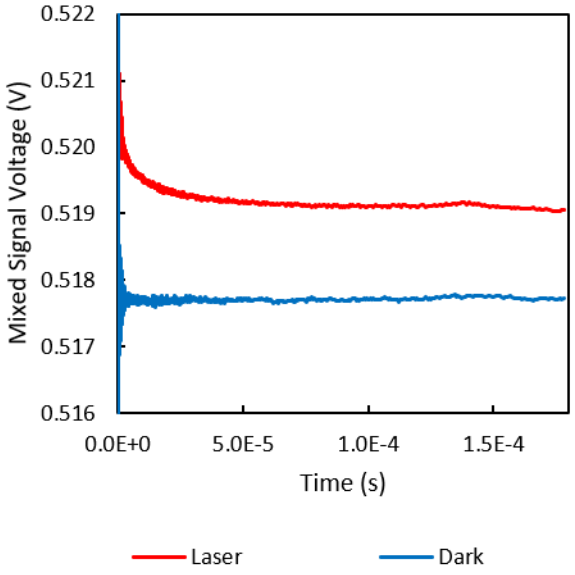

Figure 53: Transient X band microwave conductivity measurements of a RuN3 dyed mesoporous TiO_2 film with LiI_3 100 mM electrolyte at the phase-matched resonant frequency in the dark (blue) and after laser excitation (red). The 0.3% baseline shift is due to slight temperature variation of the voltage-controlled oscillator and phase shifter.

Attempts at a Two-Electron-Transfer Iodide Oxidation Catalyst

Introduction

From nanosecond transient absorption, nanosecond transient microwave conductivity, and foot-of-the-wave measurements, it appears that the factors limiting efficiency of infrared-absorbing osmium polypyridyl dyes in DSSCs is slow dye regeneration by the redox electrolyte. To continue leveraging the I^-/I_3^- redox couple's desirable features, specifically slow electron in TiO_2 to I_3^- recombination, high solubility, high mobility, low cost, and well aligned formal reduction potential, while overcoming its drawbacks, specifically slow regeneration due to a large one-electron-transfer activation energy, several two-electron-transfer catalysts were designed, synthesized, tested and implemented. Unfortunately, none of these catalysts enhanced DSSC performance.

Theory

The I^-/I_3^- redox shuttle is known to regenerate oxidized dyes via one-electron oxidation by conversion of two I^- reducing to diiodide (I_2^-). Two I_2^- molecules quickly disproportionate to form I^- and I_3^-.[17,20] At the counter electrode I_3^- is converted back to three I^- via a two-electron reduction. The large activation energy needed to generate the highly unstable intermediate I_2^- usually requires an overpotential of ~500 mV to occur on the timescale of electron in TiO_2 to oxidized dye recombination.

It is possible that a two-electron-transfer catalyst could accumulate charge from multiple dyes via one-electron transfer and then drive two-electron iodide oxidation directly (**Figure 2**). This would probably involve oxidation of two I^- to iodine (I_2) followed by association with a third I^- to form I_3^-. I_2 is much more stable than $I_2^{\cdot-}$ and would only be expected to require an overpotential of ~100 mV to achieve comparable electron transfer rates. A dye with a more negative formal reduction potential could be employed because it would drive a less energy intensive process, resulting in higher current and voltage output.[102]

Conductive Organic Polymer Catalyst: PEDOT

Sunlight is diffuse and so the majority of dyes are not expected to be excited twice before recombination occurs.[103] It is unlikely even for adjacent dyes to both be in the oxidized state. This introduces interesting challenges to charge accumulation. Using a conductive polymer as a charge accumulation catalyst could overcome the diffuse excitation problem by using large polymer aggregates that contact many dyes.

We initially thought that poly(3,4-ethylenedioxythiophene) (PEDOT) could act as a two-electron-transfer catalyst in DSSCs with the I^-/I_3^- redox shuttle. PEDOT is an electron rich polythiophene used to accumulate positive charge from multiple dyes in solid state DSSCs where it acts as a solid state redox shuttle.[104–106] PEDOT also catalyzes two-electron I_3^- reduction when used as a counter electrode in DSSCs.[107,108]By combining these functions it is possible that PEDOT could act as a two-electron-transfer catalyst by simultaneously accumulating charge and preforming two-electron I^- oxidation to I_2 (**Figure 2)**. PEDOT has been integrated into TiO_2 mesoporous films using spin coating and drop casting methods with poor penetration and surface

coverage. Photoelectropolymerization achieves greater surface coverage by polymerizing 3,4-ethylenedioxythiophene monomer (EDOT) directly onto the film.[104]

To confirm the hypothesis that PEDOT could be used as a two-electron-transfer catalyst with low overpotential relative to the redox electrolyte potential, PEDOT was electropolymerized onto an FTO electrode and then the electrode performance was compared with platinized FTO and unmodified FTO, the results of which are shown in Figure 54.

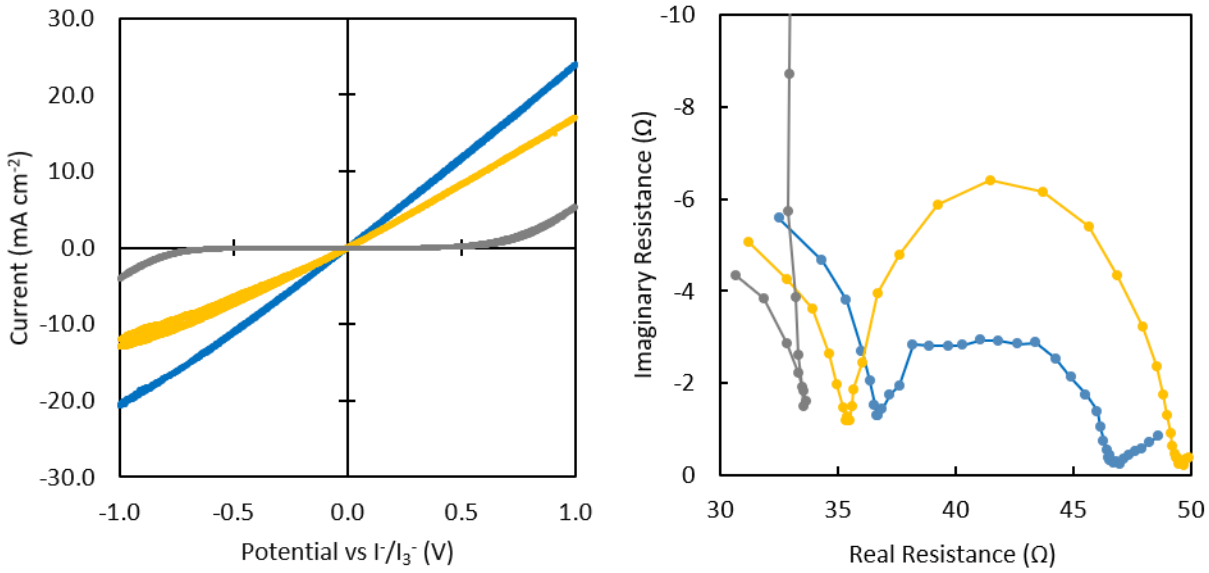

Figure 54: Cyclic voltammetry (left) and Nyquist plot of impedance (right) of unmodified FTO (gray), platinized FTO (yellow), and PEDOT on FTO (blue) in Lewis electrolyte.

Unmodified FTO showed very poor catalysis of LiI and LiI_3, requiring 0.5 V of overpotential in either direction of the solution potential before significant current passed. FTO that had been modified with platinum nanoclusters or PEDOT exhibited an ohmic catalytic response that was largely determined by solution resistance. Neither oxidative current was only mildly favored over reductive current as evidenced by the similar cyclic voltammogram slope in the oxidative and reductive regimes. Impedence spectroscopy of PEDOT demonstrated a lower charge transfer resistance than platinum nanoclusters. Considering that platinum nanoclusters are

a suitable counter electrode that does not impede cell performance for high performing RuN3 cells, PEDOT, which a lower charge transfer resistance should be capable of operating under high current densities without perturbing the performance of a DSSC.

To confirm the hypothesis that PEDOT could accumulate charge, cyclic voltammetry of EDOT monomer in tetrahydrofuran (THF) solution was performed and the results shown in **Figure 55**. EDOT is known to polymerize to PEDOT when oxidized via the reaction shown in **Figure 56**.

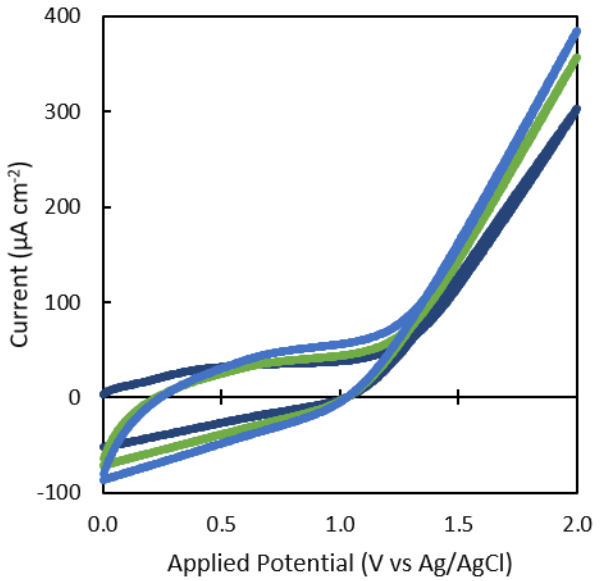

Figure 55: Consecutive cyclic voltammogram scans number 1 (dark blue), 4 (green), and 7 (light blue) of EDOT 0.05 M + $TBAClO_4$ 0.1 M in THF solution.

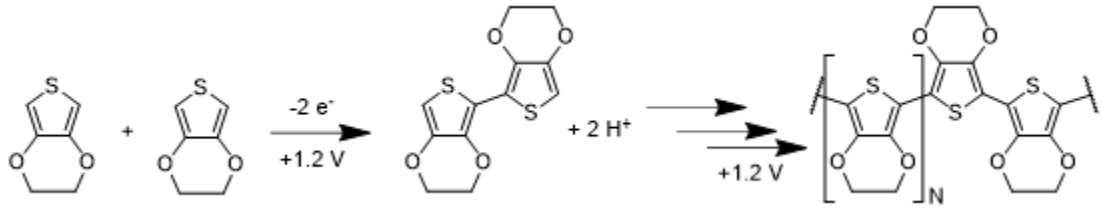

Figure 56: Reaction scheme of EDOT polymerization to PEDOT.

The polymerization onset potential was determined to be approximately +1.2 V versus Ag/AgCl. Consecutive scans showed greater current density beyond +1.2 V as the PEDOT

surface grew, exposing more active surface area for polymerization.[109] This greater surface area did not significantly increase the electrode capacitance as can be seen in the lack of hysteresis in the polymerization regime beyond 1.2 V vs Ag/AgCl. This suggests that the increasing hysteresis with scan number seen from 0 to 1.2 V vs Ag/AgCl is due to accumulation of charge on the PEDOT polymer deposited on the electrode surface.

To measure if PEDOT could serve as a two electron catalyst DSSCs were fabricated in pairs by dyeing mesoporous TiO_2 thin films on FTO coated glass with 1 mM solutions of $[Ru(bpy)_2(dcbpy)](PF_6)_2$, OsN719, or $Os(bpy)_2(dcbpy)$ dyes. Some basic properties of $[Ru(bpy)_2(dcbpy)](PF_6)_2$ and or $Os(bpy)_2(dcbpy)$ are listed in **Table 7**. One film from each pair was subjected to photoelectrochemical polymerization in 0.05 M EDOT solution to apply a thin layer of PEDOT. DSSCs were assembled from dyed films, a platinized FTO glass counter electrode, and a redox electrolyte composed of LiI and LiI_3 in buffered 85:15 acetonitrile:valeronitrile solution.

Table 7: Basic parameters of two additional dyes used in PEDOT containing DSSCs

Dye	E^0 (V vs. SCE)	$E^{0'*}$ (V vs. SCE)	$E_{0\text{-}0}$ (eV)
$[Ru(bpy)_2(dcbpy)](PF_6)_2$	1.23	–0.87	2.1
$Os(bpy)_2(dcbpy)$	0.81	–0.89	1.7

Table reproduced from the work of Lewis *et. al*.[37]

Table 8: Performance parameters of DSSCs fabricated with and without PEDOT catalyst

Dye	Catalyst	n[a]	V_{oc}[b] (V)	J_{sc}[b] (mA cm^{-2})	η[c] (%)
$[Ru(bpy)_2(dcbpy)](PF_6)_2$	PEDOT	2	0.41	0.56	0.14
$[Ru(bpy)_2(dcbpy)](PF_6)_2$	none	2	0.41	0.89	0.23
cis-$Os(dcbpy)_2(NCS)_2$	PEDOT	1	0.36	0.91	0.20
cis-$Os(dcbpy)_2(NCS)_2$	none	2	0.33	0.91	0.18
$Os(bpy)_2(dcbpy)$	PEDOT	3	0.33	1.1	0.18
$Os(bpy)_2(dcbpy)$	none	3	0.30	1.0	0.16
none	PEDOT	3	0.18	0.13	0.013
none	none	3	0.38	0.051	0.008

[a] number of cells measured. [b] values represent averages of N cells. [c] solar to electric energy conversion efficiency assuming 1 sun illumination of 100 mW cm^{-2}.

All measured cells demonstrated power production under simulated 1 Sun, AM1.5G illumination. Cells dyed with $[Ru(bpy)_2(dcbpy)](PF_6)_2$ were used as controls to measure the effect of PEDOT on dyes with a ground state potential that could readily oxidize I^- to I_2^- via a one-electron process. The presence of PEDOT did not appear to affect the open circuit potential (V_{oc}) but did decrease the short circuit photocurrent (J_{sc}) by 37% on average (**Table 8**).

In paired studies of osmium dye cells with PEDOT-containing and PEDOT-free cells fabricated in parallel from the same dyeing batch, all PEDOT-containing cells exhibited higher V_{oc} and equivalent or higher J_{sc} than their PEDOT-free counterpart with an average increase of 29±7 mV.

Undyed PEDOT-containing cells demonstrated a larger photocurrent than PEDOT-free cells because PEDOT acts as a weak dye (**Table 8**).[110] PEDOT-containing undyed cells produced an order of magnitude less current and solar-to-electric energy conversion efficiency than all dyed cells.

In brief, while PEDOT seemed to be a promising two-electron-transfer catalyst, it seemed to have little effect on cell performance.

Metal-Iodide Bonds as a Charge Accumulation Motif

Surface bound molecular catalysts can also be used to accumulate charge via a hole hopping mechanism. It has been shown both theoretically (see Kevin Tkaczibson's PhD Dissertation which hasn't been published yet and therefore cannot be cited, but will be by the time you read this) and experimentally[50] that an approximately 99:1 ratio of dyes to catalysts produces the greatest collection efficiency. Unfortunately, molecular low-overpotential I^- oxidation catalysts are poorly studied, probably because almost all conductive materials except

FTO rapidly perform I^- oxidation at low overpotential. Towards this, we investigated metal-iodide bonds as a charge accumulation motif.

We first investigated Pt(NCN)X (where NCN is 2,6-di(dimethylaminomethyl)benzene and X is Cl^- or I^-) which is known to coordinate multiple iodide atoms and chains of iodide atoms.[111,112] Cyclic voltammograms of Pt(NCN)Cl in dichloromethane, a non-coordinating solvent, showed a single, reversible two-electron transfer event typical of a Pt(II/IV) redox reaction. Cyclic voltammograms of Pt(NCN)Cl in acetonitrile, a coordinating solvent, show a non-reversible two-electron transfer at ~0.4 V vs SCE (**Figure 57** left).

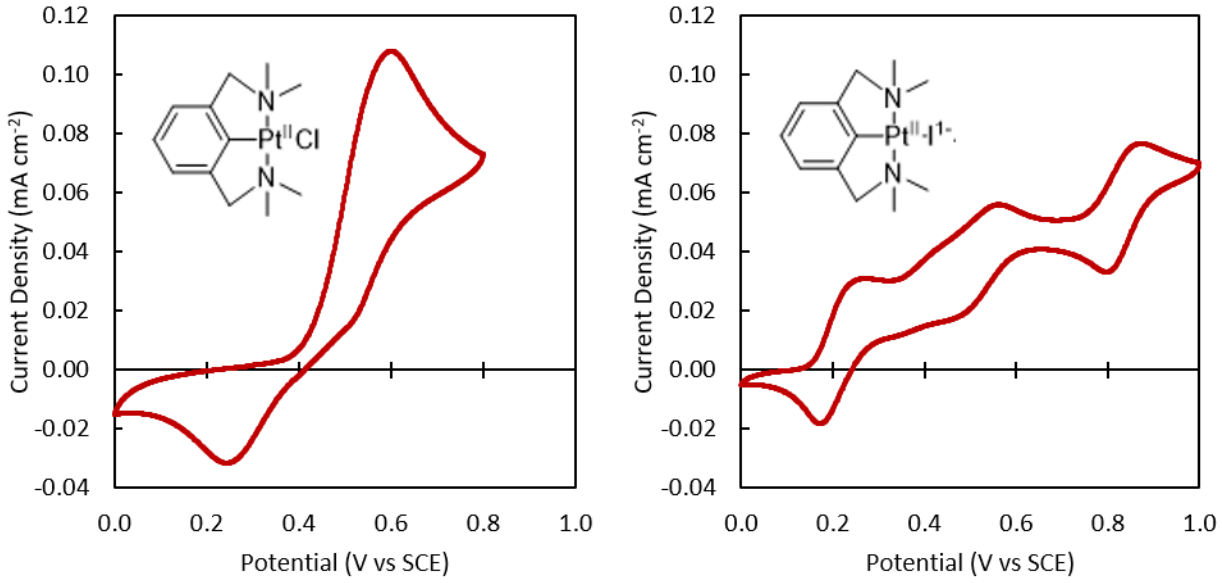

Figure 57: Cyclic voltammograms of Pt(NCN)Cl 0.5 mM (left) and Pt(NCN)I 0.5 mM (right) in 100 mM $LiClO_4$ in acetonitrile solution with chemical structures inset.

Our hypothesis is that, in the anodic sweep, two-electron transfer oxidation occurs on the Pt(II) square planar complex, followed by coordination of two acetonitrile molecules to make an octahedral Pt(IV) complex. In the cathodic sweep, two-electron transfer occurs on the Pt(IV) octahedral complex, followed by loss of two acetonitrile ligands to make the original square planar Pt(II) complex. The irreversible nature of the peak arises from the square planar vs

octahedral nature of the complex during the electron transfer process depending on the sweep direction. This mechanism is depicted graphically in **Figure 58**.

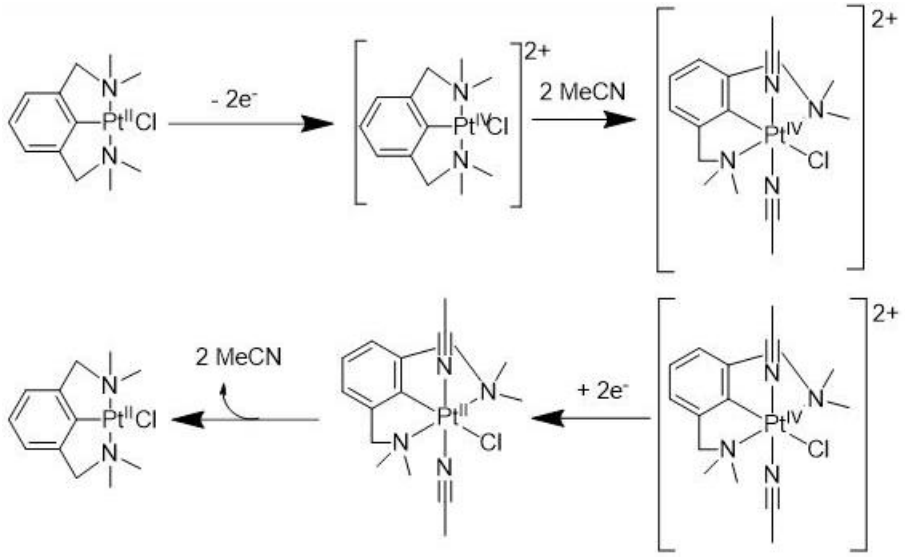

Figure 58: Proposed mechanism explaining the electrochemical behavior of Pt(NCN)Cl.

If the Cl^- ligand is replaced by an I^- ligand, the electrochemical behavior changes dramatically. Three separate one-electron transfer events occur at 0.22, 0.52, and 0.84 V vs SCE. The events at 0.22 and 0.84 V vs SCE are reversible but the event at 0.52 V vs SCE is not fully reversible. The proposed mechanism explaining this behavior is depicted in **Figure 59**, on the cathodic sweep, one electron-oxidation occurs at 0.22 V vs SCE at the iodide ligand with no change in complex geometry. At 0.52 V vs SCE, Pt(II) is oxidized to Pt(IV) with concurrent re-reduction of the iodide ligand for a net one-electron oxidation process. Two acetonitrile ligands coordinate to cause the complex to become octahedral. At 0.84 V vs SCE, the iodide ligand is oxidized again via one-electron transfer with no change in complex geometry. In the anodic sweep, the events at 0.22 and 0.84 V are reversed, however, the event at 0.52 V occurs differently. Electron transfer occurs while the complex is octahedral, instead of square planar, which is followed by loss of two acetonitrile ligands.

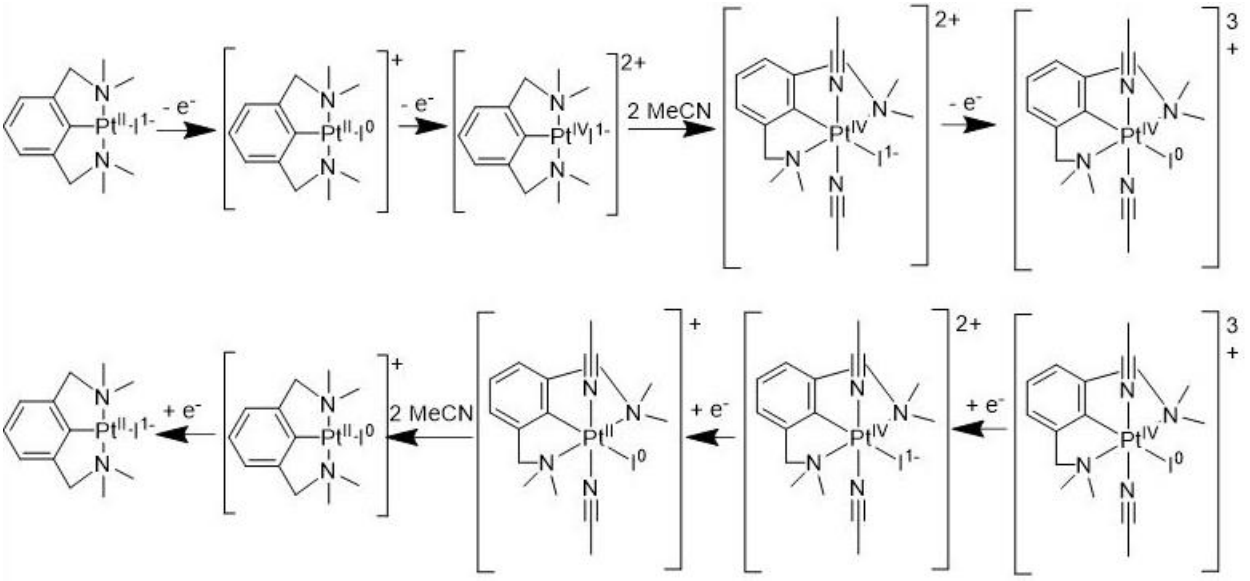

Figure 59: Proposed mechanism explaining the electrochemical behavior of Pt(NCN)I

Pt(NCN)I can be thrice oxidized by one-electron-transfer events and has sufficient potential in its twice oxidized state to oxidize I^- to I_3^-, features which satisfy some of the requirements of an I^-/I_3^- catalyst for use in DSSC. However, there are several features that prevent it from being a good catalyst. The second oxidation event could not be easily performed by an infrared absorbing dye, such as OsN3, Osppy, $OsCl_2$, or OsI_2 because their formal redox potentials are negative of 0.52 V vs SCE. The second oxidation event is also not reversible, which introduces a source of energy loss in the DSSC and should be avoided. Despite these drawbacks Pt(NCN)I demonstrated that oxidative equivalents can be stored the iodide ligand on complexes with metal-iodide bonds and that these oxidative equivalents can be accessed at potentials close to the desired potential range between the formal potential of I^-/I_3^- redox electrolyte and the ground state formal potential of infrared absorbing dyes.

Water-Oxidation-Catalyst-Inspired Osmium-Iodide Complexes

Charge accumulation from multiple ruthenium dyes to drive four-electron water oxidation catalysis has been successfully demonstrated.[113–122] **Figure 60** shows the structures of three water oxidation catalysts used for this purpose.

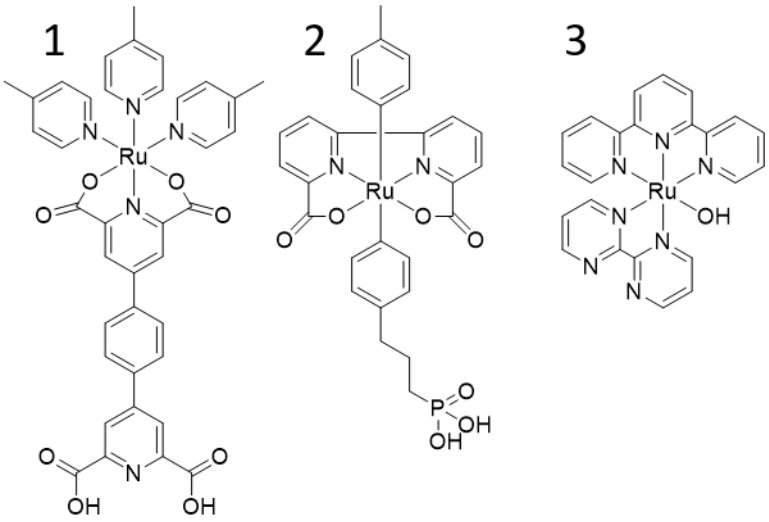

Figure 60: Structures of three example water catalysts.

Licheng Sun and coworkes successfully bound catalysts 1 and 2 of **Figure 60** to TiO_2 films dyed with ruthenium polypyridyl dyes and generated oxygen from water under normal sunlight illumination.[113,114,116,117] The exact mechanism of catalysts 1 and 2 was not determined, however it was proposed water coordinates catalyst 2 between the two carboxylate ligands to make a 7-coordinate compound. Catalyst 3 was used in solution, as it lacks an acidic surface-binding group, but the mechanism of an analogue is well described by Thummel and coworkers and is reproduced in **Figure 61**.[119] This mechanism prevents charge build up on the catalyst by addition of hydroxide or loss of a proton between oxidation steps to allow "redox potential leveling" which prevents subsequent redox events from increasing in potential.[123]

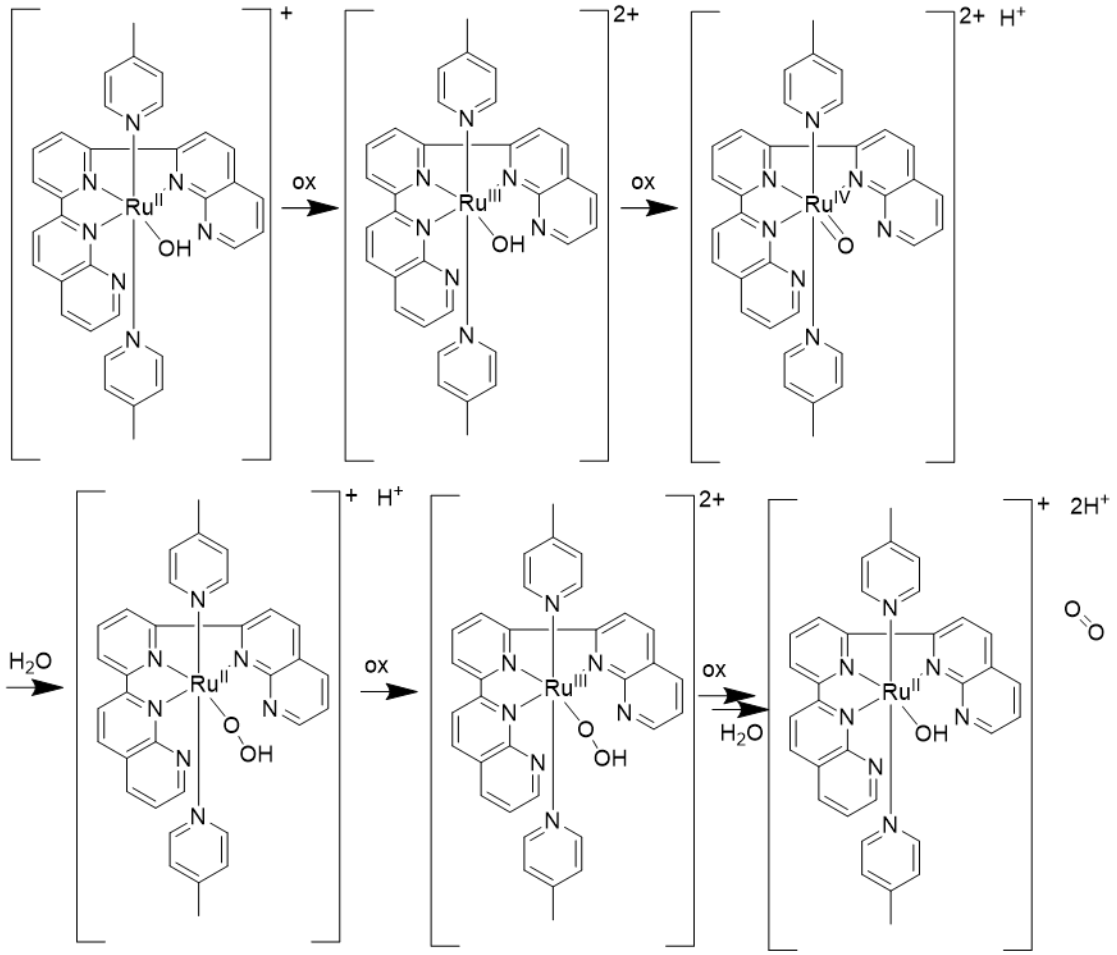

Figure 61: Mechanism of a water oxidation catalyst with a hydroxide ligand.

We considered using these structural motifs to perform two-electron I^- oxidation. To do this we would replace the ruthenium(II) metal centers with osmium(II) metal centers to take advantage of osmium's more negative reduction potential compared to ruthenium. This is similar to how we designed our infrared absorbing dyes. Also, any hydroxide ligands would be replaced with iodide to leverage the metal-iodide motif discussed in the previous section. I synthesized four potential iodide oxidation catalysts based on these design principles with the structures shown in **Figure 62**.

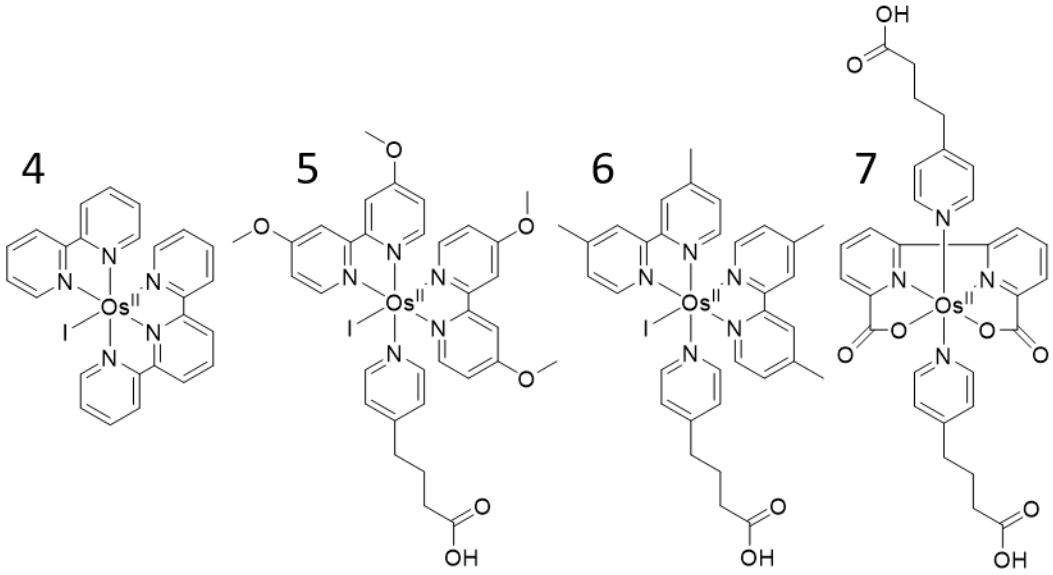

Figure 62: Structures of four potential iodide oxidation catalysts.

To determine if the osmium-iodide charge accumulation motif demonstrated by catalyst 4 (**Figure 62**) could indeed accumulate multiple charges, cyclic voltammetry was performed on 1 mM solutions of [Os(trpy)(bpy)Cl]Cl, [Os(trpy)(bpy)I]Cl, [Os(trpy)(bpy)I]I, (where trpy is 2,2':6',2''-terpyridine) and LiI using a platinum ultramicroelectrode (UME) (**Figure 63**).

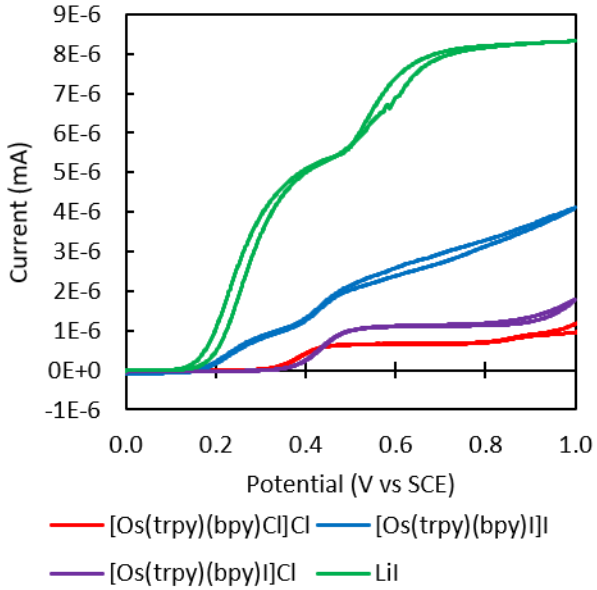

Figure 63: Cyclic voltammograms of 1 mM solutions of [Os(trpy)(bpy)Cl]Cl (red), [Os(trpy)(bpy)I]Cl (purple), [Os(trpy)(bpy)I]I (blue), and LiI (green) in 100 mM $LiClO_4$ in acetonitrile using a platinum ultramicroelectrode (UME).

All three [Os(trpy)(bpy)X]X species demonstrated a single-electron transfer event at ~0.4 V vs SCE which was assigned to oxidation of Os(II) to Os(III). [Os(trpy)(bpy)I]I demonstrated an additional one-electron oxidation event at ~2.3 V vs SCE. To determine if this event were due to oxidation of the I^- counter ion, the current due to this event was compared with the current from a LiI solution of equal concentration. In LiI solution, a two-electron oxidation occurs at ~0.23 V vs SCE, but the current passed is much larger than that seen in the presence of $[Os(trpy)(bpy)I]^+$. One possible rationale for this behavior is that I^- coordinates to $[Os(trpy)(bpy)I]^+$, either to osmium as a seven ligand coordination complex or to the iodide ligand similar to I^- coordination to I_2 in the I_3^- ion. To test this hypothesis, [Os(trpy)(bpy)I]I was crystallized (by me) and a crystal structure was determined by Joe Ziller at the UCI X-ray Crystallography Facility (Figure 64). The structure did not show coordination of I^- to either osmium or the iodide ligand, as so the origin of the lower-than-expected current in cyclic voltammetry remains undetermined.

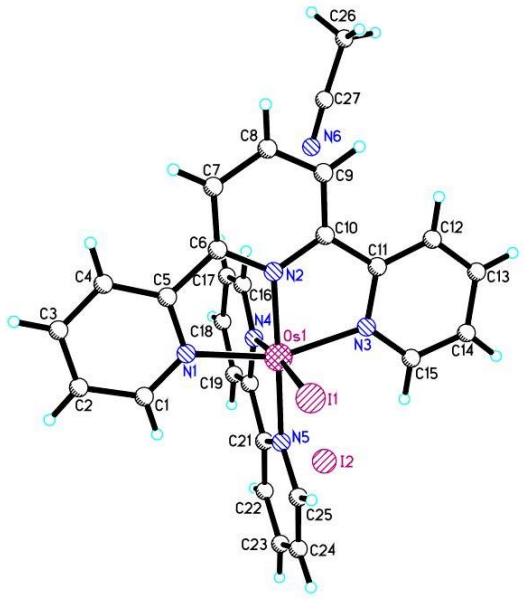

Figure 64: X-ray crystal structure of [Os(trpy)(bpy)I]I crystallized from of acetonitrile solution. I2 is behind the trpy ligand and is not coordinated to I1.

Some modifications were necessary to catalyst 4 before it could be used in a DSSC with an infrared-absorbing dye. The first oxidation potential at ~0.23 V vs SCE was fine, but the second at ~0.4 V vs SCE was too positive. An acidic group to bind the catalyst to the film was also necessary. Towards these goals, catalyst 5 (**Figure 62**) was synthesized. The rationale was that the methoxy groups on the 4,4'-dimethoxy-2,2'-bipyridine (dmobpy) ligands would be electron donating and make the compound easier to oxidize. The 4-(pyridine-4-yl)butanoic acid (pybu) ligand would act as a binding group. Unfortunately, cyclic voltammetry of catalyst 5 bound to a titanium dioxide film showed a higher than expected reduction potential of 0.75 V vs SCE. This is too positive to be used with an infrared absorbing dye in a DSSC.

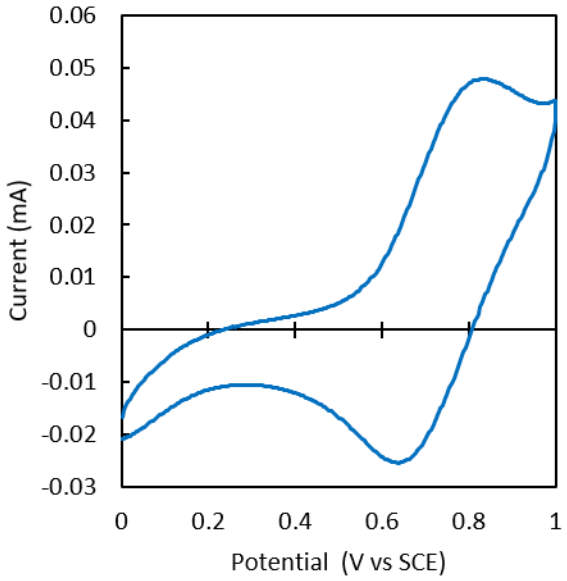

Figure 65: Cyclic voltammogram of $Os(dmobpy)_2(pybu)I$, catalyst 5, bound to a mesoporous TiO_2 thin film in 100 mM $LiClO_4$ acetonitrile solution at 100 mV s^{-1}.

One possible reason for this positive shift in potential could be that methoxy groups on pyridine ligands are electron donating through the pi-orbital system but electron withdrawing through the sigma-orbital system. If the dmobpy ligands have poor pi-orbital overlap with the d_{xy}, d_{xz}, and d_{yz} orbitals of osmium due to a non-ideal bite angle, then pi-effects would be small

relative to sigma affects and the reduction potential would demonstrate a positive shift compared to a system without methoxy groups. If this is cause of the positive potential shift, the shift could be reversed by replacing the methoxy groups with sigma donating groups, such as methyl groups. To test this, catalyst 6 (**Figure 62**) was synthesized.

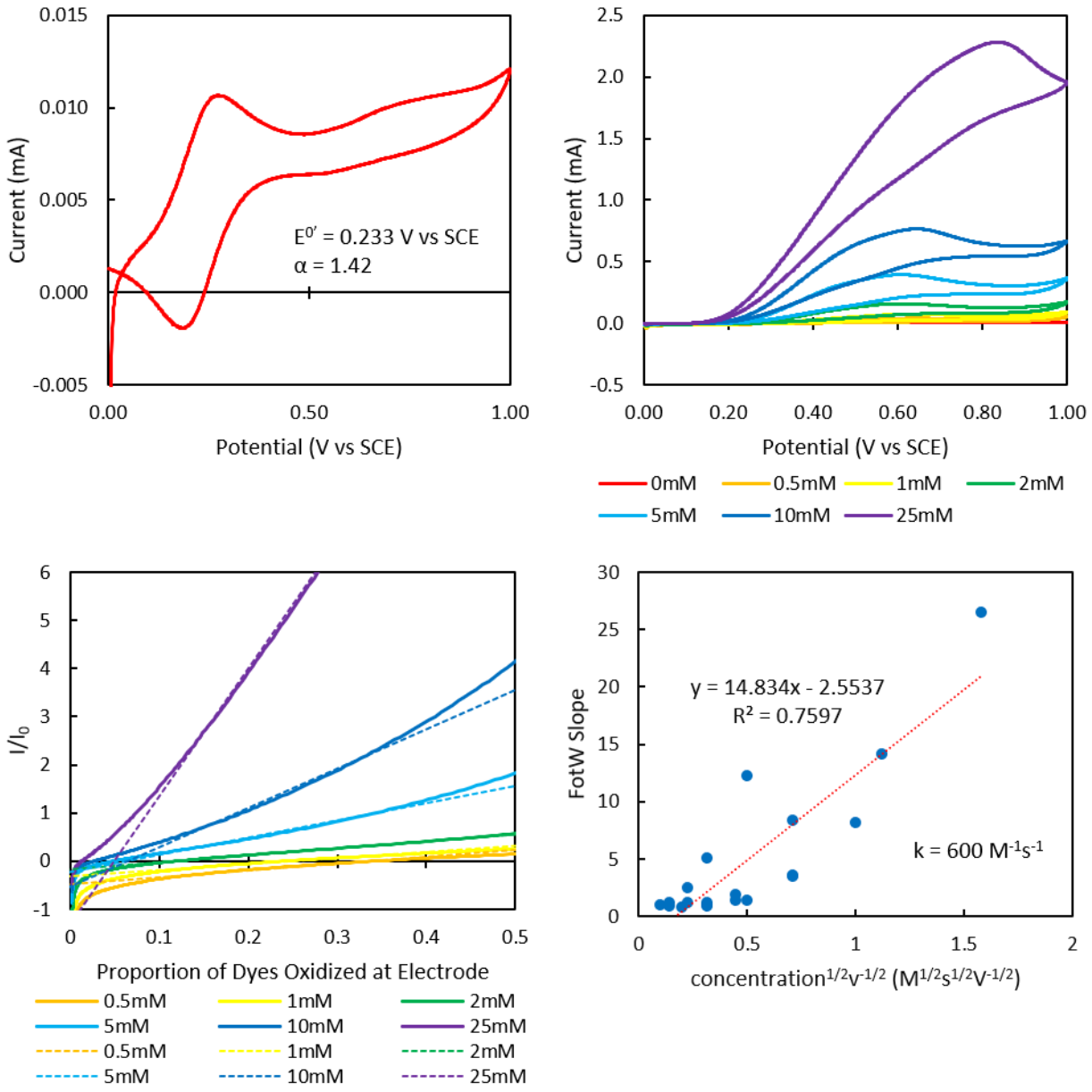

Figure 66: Upper left: cyclic voltammogram of a mesoporous titanium dioxide thin film dyed with $[Os(dmbpy)_2(pybu)I]^+$, catalyst 6, in 100 mM $LiClO_4$ solution in acetonitrile at 10 mV s^{-1} with calculated formal reduction potential and non-ideality factor, α, shown. Upper right: cyclic voltammograms of the same film with addition of LiI substrate. Lower left: foot-of-the-wave style graph of the data shown in the upper right. Lower right: plot of foot-of-the-wave slope as a function of the square root of concentration divided by the square root of scan rate with calculated second order rate constant, k, shown.

Cyclic voltammetry of $[Os(dmbpy)_2(pybu)I]^+$ (where dmbpy is 4,4-dimethyl-2,2'-bipyridine), or catalyst 6, bound to a mesoporous titanium dioxide thin film demonstrated a

formal redox potential of 0.233 V vs SCE (**Figure 66**). The Nernstian non-ideality factor, α, was estimated to be 1.42 based on peak-to-peak separation. This potential is in the correct range to be used as an iodide oxidation catalyst with OsN3 and Osppy dyes and supports the sigma-donation hypothesis.

Cyclic voltammetry of the same catalyst 6 dyed film with LiI substrate showed a catalytic current. At the time of this experiment, I did not yet understand FotW analysis and so the experimental conditions were not optimized for FotW. However, FotW analysis was able to be performed on the old data. FotW showed moderately linear fits over the first 40% of the wave and FotW slopes were able to be roughly fit to a line with respect to the square root of substrate concentration divided by the square root of scan rate. The calculated second order rate constant, k, was 600 $M^{-1}s^{-1}$, which is substantially faster than k for OsN3, 78 $M^{-1}{}_{s}{}^{-1}$ even though OsN3 has a larger driving force for oxidation, suggesting that Catalyst 6 is a moderate catalyst. k values in the range of 10^4 to 10^5 $M^{-1}s^{-1}$ are expected to be necessary for a good catalyst.

Os(6,6'-dcbpy)$(pybu)_2$ (where 6,6'-dcbpy is 6,6'-dicarboxy-2,2'-bipyridine) or catalyst 7 (**Figure 62**) was made as an osmium analogue of catalyst 2 (**Figure 60**) with the hope that it would be able to achieve a seven coordinate intermediate by I^- ligation similar to how catalyst 2 was hypothesized to achieve a seven coordinate intermediate by H_2O ligation. Cyclic voltammetry of catalyst 7 varying scan rate showed an anodic peak with a position that did not change with scan rate, but a cathodic peak with a potential that became more negative with increasing scan rate (**Figure 67**). This could be attributed to having two one-electron-transfer events at 0.18 and 0.31 V vs SCE or a single non-reversible electron transfer event with a slow EC mechanism that becomes reversible at faster scan rates, perhaps oxidation followed by ligation of an acetonitrile ligand. regardless of the mechanism, the cathodic sweep was mostly

not affected by scan rate compared to the anodic sweep. LiI substrate was added and catalytic current observed. Because FotW analysis only utilizes the most positive electron transfer event of the cathodic sweep, good linear fits were obtained from FotW style graphs by using the oxidation event at 0.31 V with an α value of 1.22.

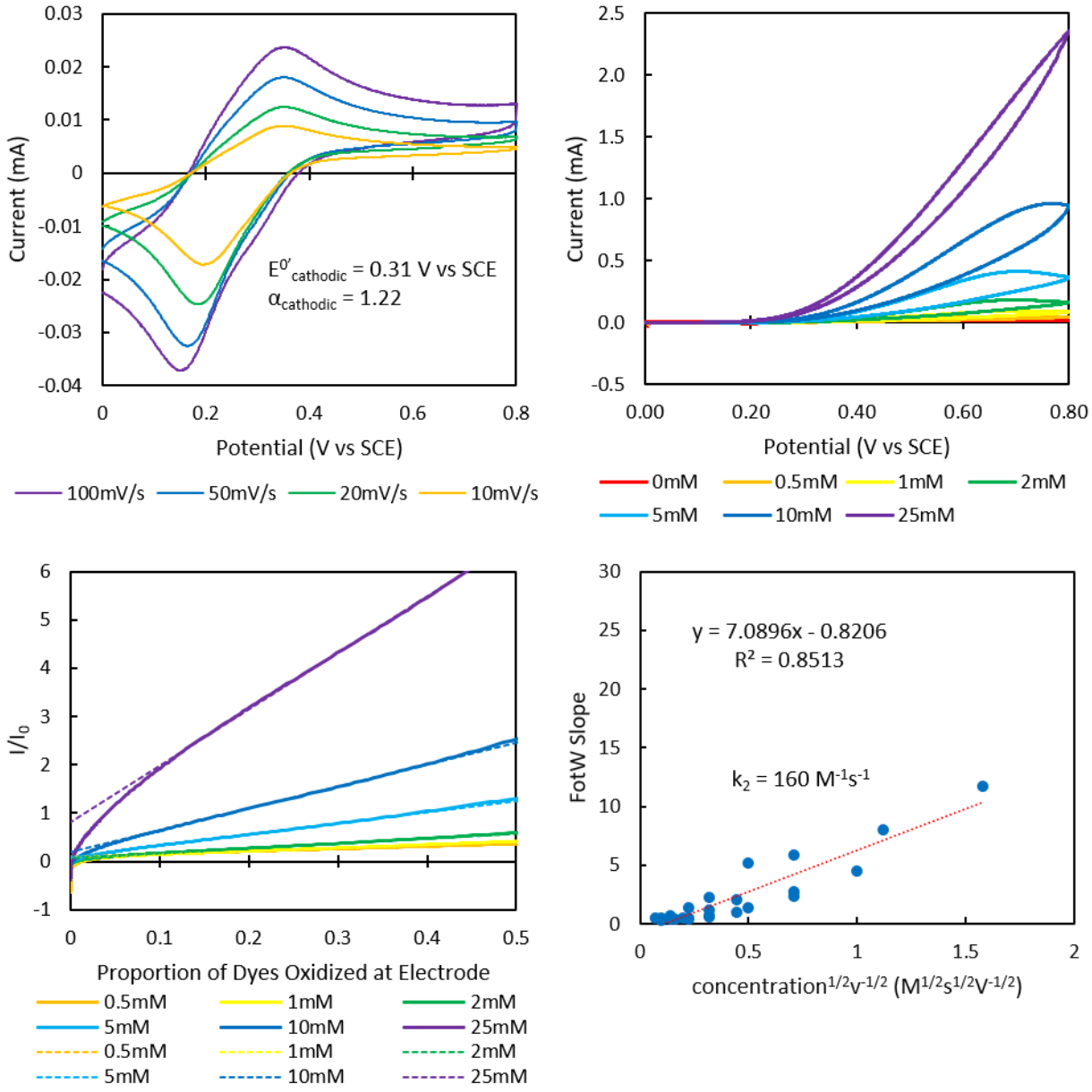

Figure 67: Upper left: cyclic voltammograms of a mesoporous titanium dioxide thin film dyed with Os(6,6'dcbpy)(pybu)$_2$, catalyst 7, in 100 mM $LiClO_4$ solution in acetonitrile at multiple scan rates with calculated formal cathodic reduction potential and non-ideality factor, α, shown. Upper right: cyclic voltammograms of the same film with addition of LiI substrate. Lower left: foot-of-the-wave style graph of the data shown in the upper right. Lower right: plot of foot-of-the-wave slope as a function of the square root of concentration divided by the square root of scan rate with calculated second order rate constant, k, shown.

At first glance, catalyst 7 appears to be a worse catalyst than catalyst 6 in all aspects. Its formal cathodic reduction potential of 0.31 V vs SCE provides less of a driving force for

regeneration of OsN3 and Osppy dyes. Also, its second order rate constant for electron transfer from I^- of 160 $M^{-1}s^{-1}$ is only a factor of two faster than that of OsN3. Closer inspection of the FotW slope as a function of concentration and scan rate reveals that FotW slope is more linear with respect to concentration than the square root of concentration (**Figure 68**).

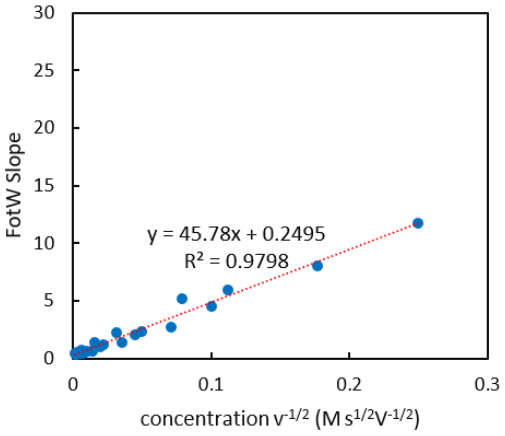

Figure 68: Foot-of-the-wave slope as a function of concentration divided by the square root of scan rate of a mesoporous titanium dioxide thin film dyed with Os(6,6'dcbpy)(pybu)$_2$, catalyst 7, in 100 mM $LiClO_4$ solution in acetonitrile with addition of LiI substrate. Notice the greater linearity and higher correlation constant, R^2, than in Figure 67.

Linear correlation of FotW slope with respect to substrate concentration, instead of the square root of substrate concentration as usual, indicates that the rate-limiting step of the reaction is second order with respect to substrate or a catalyst-substrate complex.[81,84] Because multiple mechanisms can generate this behavior, no further analysis could be performed without supporting measurements. However, it can be assumed that increasing the substrate concentration would increase the reaction rate, improving the catalytic behavior of catalyst 7 at high LiI concentration.

To test the performance of catalysts 6 and 7 in working conditions, DSSCs dyed with OsN3 or Osppy and/or a small amount of catalysts 6 or 7 were prepared using Lewis electrolyte and their performance compared, the results of which are shown in Table 9.

Table 9: DSSC performance parameters of cells using OsN3 and Osppy dyes with and without molecular catalysts under 100 mW cm^{-2} simulated solar illumination.

	n	E_{OC} (V)	J_{SC} (mA cm^{-2})	Fill Factor	η (%)
OsN3	3	0.22±0.02	0.5±0.1	0.43±0.01	0.05±0.01
OsN3 + Catalyst 7	3	0.23±0.04	0.5±0.1	0.46±0.04	0.05±0.02
Osppy	6	0.05±0.01	0.041±0.007	0.21±0.08	0.001±0.001
Osppy + Catalyst 6	3	0.036±0.006	0.04±0.02	0.242±0.003	0.0004±0.0002
Osppy + Catalyst 7	3	0.041±0.006	0.04±0.02	0.304±0.003	0.0005±0.0002
Catalyst 6	1	0.011	0.014	0.244	0.00003
Catalyst 7	3	0.020±0.002	0.024±0.007	0.256±0.002	0.00012±0.00002
TiO_2	3	0.05±0.05	0.004±0.001	0.254±0.007	0.00005±0.00004

Reported error values are one standard deviation.

Catalysts 6 and 7 in the absence of dyes produced cells with low J_{SC} and V_{OC} values, barely outperforming unsensitized cells. This was expected because the pybu ligand does not provide good electronic contact with the TiO_2 surface so injection is expected to be slow. Cells containing OsN3 dye and catalyst 7 performed within error of cells containing only OsN3 dye. Cells containing Osppy dye and either catalyst 6 or 7 performed more poorly than cells containing only Osppy dye. In short, catalyst 6 and 7 failed to perform under working DSSC conditions.

There are several possible reasons why catalysts 6 and 7 failed to work. It is possible that the catalysts did not turn over fast enough to prevent recombination, although catalyst turnover is expected to be faster than that of the dyes based on foot of the wave and electron in TiO_2 to oxidized catalyst recombination is expected to be slower based on the increased TiO_2 to complex distance induced by the pybu ligand. More likely is that charges from the dyes did not reach the catalysts fast enough for dye regeneration by catalyst to significantly compete with electron in TiO_2 to oxidized dye recombination. In Hsiang-Yun Chen and Shane Ardo's charge accumulation demonstration,[50] the dye used was $[Ru(dcbpy)(dmbpy)_2]^{2+}$ which is known to have

a faster D_{app} value than other similar ruthenium complexes,[63,124] slower recombination than OsN3 (25% recombination at 10 μs versus 80% recombination at 10 μs), and a greater driving force for regeneration by the catalyst (~0.5 and ~0.25 eV for RC-11^0 and RC-11^{1+} to $[Ru(dcbpy)(dmbpy)_2]^{2+}$ respectively versus 0.01 eV for Catalyst 7 to OsN3 and 0.15 and 0.06 eV for Catalysts 6 and 7 to Osppy respectively). Despite all these advantages, the quantum yield for charge collection was only 34% in Chen and Ardo's laser experiment that involved higher-than-solar light fluences. The decreased hopping speed, lifetime, regeneration driving force, and photon flux would all decrease expected quantum efficiency of my catalysts relative to Chen and Ardo's already non-ideal system. To successfully use an iodide oxidation catalyst, a dye with faster hole hopping and significantly longer lifetime will be required.

Conclusions

In an attempt to continue using the I^-/I_3^- redox shuttle which has the desirable characteristics of low cost, high solubility, high mobility, and slow electron in titanium dioxide to redox shuttle recombination several iodide oxidation catalysts were synthesized and tested. PEDOT, a conductive polymer demonstrated the ability to accumulate charge and drive iodide oxidation at very low overpotential. DSSCs were fabricated with a thin layer of PEDOT by photoelectropolymerization of EDOT monomer directly onto the dyed TiO_2 film. Unfortunately, PEDOT did not significantly enhance DSSC performance. Two molecular catalysts, inspired by water oxidation catalysts and utilizing a metal-iodide bond charge accumulation motif, were synthesized, $[Os(dmbpy)_2(pybu)I]^+$ and $Os(6,6'dcbpy)(pybu)_2$. Both molecular catalysts demonstrated formal reduction potentials that were sufficiently positive to oxidize iodide in the oxidized state, but sufficiently negative to reduce photo-oxidized OsN3 and Osppy dyes in the

reduced state. Both molecular catalysts also demonstrated faster iodide oxidation second order rate constants, determined by foot-of-the-wave analysis, than OsN3 dye. DSSCs fabricated with OsN3 and Osppy dyes with these two catalysts did not demonstrated similar or worse efficiencies than DSSCs fabricated with OsN3 and Osppy dyes without catalysts. This is probably due to poor regeneration speed of the dyes by the catalyst due to slow hole-hopping, low driving force for regeneration, and short electron in TiO_2 to oxidized dye lifetimes.

Experimental

Synthesis of Catalysts and Analogs

Pt(NCN)I and Pt(NCN)Cl were synthesized by Hsiang-Yun Chen.

Synthesis of 6,6'-dicarboxy-2,2'-bipyridine (6,6'-dcbpy)

Synthesis of 6,6'-dcbpy was carried out according to previously established procedures.[125] 6,6'-dimethyl-2.2'-bipyridine (0.5026 g, 2.7 mmol), $KMnO_4$ (2.9782 g, 18.8 mmol), and water (33 ml) were added to a round bottom flask, stirred, at heated at 90 °C under air for 14 hours. The purple solution turned brown during heating and formed a precipitate as it cooled to room temperature. The brown solid was removed by filtration and the aqueous solution was extracted with diethyl ether three ties, discarding the clear organic layer to yield a clear pink aqueous solution. HCl 12 N was added to the aqueous layer until the pH of the solution reached 2 causing the solution to turn blue and a white precipitate to form. The white precipitate was collected by filtration and dried under vacuum (0.1929 g, 0.79 mmol, 29% yield).

An NMR sample was prepared by dissolving 24 mg of the white solid in 1 ml DMSO-D_6 and filtering through glass wool. NMR (499 MHz DMSO-D_6) δ 8.76 (d, J = 22.9 Hz, 2H, position 5), δ 8.22 (dd, J = 5.3, 35.6 Hz, 2H, position 4), δ 8.22 (dd, J = 31.1, 47.0 Hz, 2H, position 3). ESI Mass Spectrometry: M/z 266.93 ($M + Na^+$)

Synthesis of 4-(pyridine-4-yl)butanoic acid (pybu)

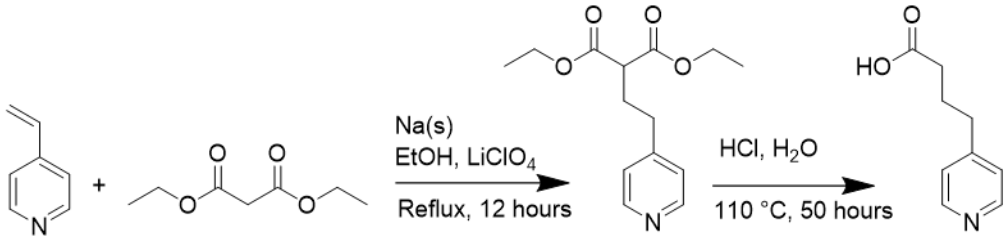

Figure 69: Reaction scheme for the synthesis of pybu ligand

Michael addition was heavily modified from literature procedures.[126] Hydroquinone was added to prevent polymerization of 4-vinyl pyridine. lithium perchlorate was added as a Lewis acid to activate the Michael addition.[127]

Lithium perchlorate (2.1973 g, 30 mmol), hydroquinone (0.0064 g, 0.058 mmol), diethylmalonate (4.6 ml, 4.83 g, 30.2 mmol), 4-vinylpyridine (2.2 ml, 2.15 g, 13.4 mmol), ethanol (38.5 ml), and sodium metal (0.79 g, 34.4 mmol) were added to a round bottom flask. As the sodium was added the solution bubbled and turned a cloudy orange. The solution was refluxed overnight and cooled to room temperature. Ethanol was removed by rotary evaporation to yield an orange solid which was acidified with HCl 2 N (50 ml, 100 mmol) to form a orange liquid, with evolution of bubbles as the solid dissolved. The solution was extracted 3 times with diethyl ether (30 ml each) and the orange organic layers were discarded. The solution was basified with NaOH 3 N (50 ml, 150 mmol). The solution fizzed, became cloudy, and a red oil formed on the surface. The solution was extracted 3 more times with diethyl ether (50 ml each) and the organic layer collected. Removal of diethyl ether by vacuum yielded an orange liquid which was determined to be the Michael adduct product by NMR of 2 drops of the liquid in 1 ml DMSO.

NMR (499 MHz DMSO-D_6) δ 8.49 (d, 2H), δ 7.29 (dd, 2H), δ 4.16 (m, 4H), δ 3.45 (m, 1H), δ 2.56 (m, 2H), δ 2.11 (m, 2H), δ 1.21 (dd, 6H). There is much diasteriotopicity in this molecule so the NMR shows non-standard splitting patterns.

The crude Michael adduct was added to aqueous HCl 6 N (50 ml) and heated at 110 °C for 50 hours, forming and orange liquid. The solvent was removed by rotary evaporation to yield an orange brown oil. The oil was refluxed in toluene (100 ml), and then cooled to 0 °C to form an oil. The toluene was decanted and the oil was dissolved in hot methanol. ethyl acetate was added to recover the oil and the methanol and ethyl acetate were decanted. 5 consecutive nitrogen-vacuum cycles were applied to the oil to form a light-brown, hydrophilic solid which was determined to be pybu (0.9825 g, 5.9 mmol, 30% yield over two steps).

NMR (499 MHz DMSO-D_6) δ 8.86 (d, 2H), δ 7.99 (d, 2H), δ 2.91 (t, 2H), δ 2.31 (dp, 2H), δ 1.96 (m, 2H). There is less diasteriotopicity in this molecule but it is still there.

Synthesis of [Os(trpy)(bpy)Cl] Cl

All osmium complexes in this chapter were synthesized using procedures modified from David A. Buckingham's graduate work at the Australian National University.[128,129]

2,2':6'-2"-terpyridine (0.0505 g, 0.22 mmol), $Na_2OsCl_6 \cdot 2H_2O$ (0.1105 g, 0.23 mmol), and ethylene glycol (2.5 ml) were added to a 50 ml round bottom flask fitted with a reflux condenser and a rubber septum. 3 vacuum-nitrogen cycles were applied and yellow-green bubbles evolved from the deep green solution. The solution was brought to reflux at 210 °C for 15 minutes and then allowed to cool to room temperature. 2,2'-bipyridine (0.0367 g, 0.23 mmol) was added and 3 vacuum-nitrogen cycles performed. The solution was brought to reflux for 1 hour and then allowed to cool to room temperature. Ethanol (5 ml) was added and the solution was stirred, and sonicated. Diethyl ether (40 ml) was added and the solution was stirred,

sonicated, and placed in the freezer for 1 hour. The solution was filtered with a glass frit filter, rinsed with cold diethyl ether, and dried under vacuum to yield [Os(trpy)(bpy)Cl] Cl as a powdery purple solid (0.1411 g, 0.22 mmol, 95% yield)

Synthesis of [Os(trpy)(bpy)I]I

[Os(trpy)(bpy)Cl]Cl (0.1467 g, 0.23 mmol), NaI (0.7530 g, 5.0 mmol), and ethylene glycol (7.5 ml) were added to a round bottom flask fitted with a condenser and a rubber septum. 3 vacuum-nitrogen cycles were performed. The solution was brought to reflux using a sand bath for 35 minutes and then allowed to cool to room temperature. NaI (9 g) was dissolved in water (30 ml) and the solution was added to the reaction mixture and stirred. Placing the mixture in the fridge overnight caused [Os(trpy)(bpy)I]I to precipitate as a black solid which was collected by filtration through a glass frit and dried under vacuum (0.0553 g, 0.066 mmol, 30% yield).

NMR was performed on a 6.6 mg sample of the solution in 1 ml of acetonitrile-D_3.

1H NMR (499 MHz CD_3CN) δ 10.61 (ddd, *J* = 5.7, 1.4, 0.7 Hz, 1H), δ 8.62 (ddd, *J* = 8.7, 1.7, 1.1 Hz, 1H), δ 8.50 (d, *J* = 8.0 Hz, 2H), δ 8.39 (dt, *J* = 7.7, 1.2 Hz, 2H), δ 8.27 (ddd, *J* = 7.8, 1.5, 0.9 Hz, 1H), δ 7.97 (ddd, *J* = 8.1, 1.4, 0.6 Hz, 1H), δ 7.83 (ddd, *J* = 7.5, 5.9, 1.4 Hz, 1H), δ 7.74 (tt, *J* = 7.8, 1.3 Hz, 4H), δ 7.55 (t, *J* = 8.1 Hz, 1H), δ 7.54 (ddd, *J* = 8.8, 7.5, 01.4 Hz, 1H), δ 7.23 (ddd, *J* = 7.7, 5.9, 1.5 Hz, 2H), δ 7.11 (ddd, *J* = 5.9, 1.2, 0.6 Hz, 1H), δ 6.88 (ddd, *J* = 7.4, 5.7, 1.3 Hz, 1H). Shifts were assigned by 2D NMR techniques.

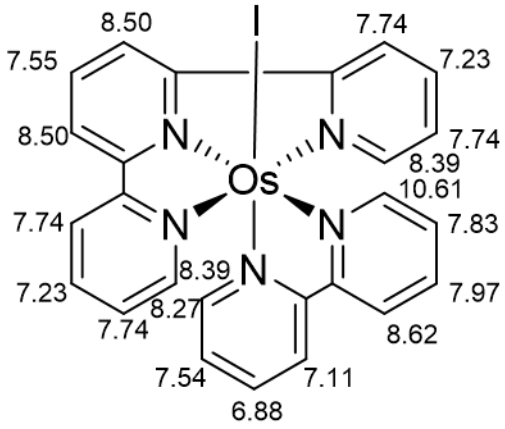

Figure 70: Structure of Os(trpy)(bpy)I labeled with 1H NMR chemical shifts.

Synthesis of [Os(trpy)(bpy)I]Cl

[Os(trpy)(bpy)I]I was synthesized as described beginning with 0.115 g $Na_2OsCl_6 \cdot 2H_2O$. [Os(trpy)(bpy)I]I was dissolved in water (12.5 ml) mixed with methanol (1 ml) and powedered AgCl (0.1 g) was added. The solution was shaken for 15 minutes and the solid removed by filtration through a syringe filter. The solvent was evaporated and the resulting solid suspended in water (5 ml). HCl 12 N (1 ml) was added and the solution was stirred and then frozen to yield [Os(trpy)(bpy)I]Cl as a black solid (0.0173 g, 0.023 mmol, 10% yield over 3 steps).

Synthesis of $Os(dmobpy)_2Cl_2$

A mixture of sodium hexachloroosmate dihydrate (0.2157 g, 0.44 mmol), 4,4'-dimethoxy-2,2'-bipyridine (dmobpy, 0.1919 g, 0.89 mmol), and ethylene glycol (5.4 ml) were added to a round bottom flask fitted with a reflux condenser. The osmium compound, which is initially a red solid, dissolves to form a green solution. The flask was evacuated, and the atmosphere replaced with nitrogen three times while stirring. The first evacuation was held until yellow-green bubbles were no longer observed. Under a blanket of nitrogen, the mixture was refluxed for 2 h. The solution changes color to a deep red-black color. After cooling to room temperature, sodium hydrosulfite (0.1 g) dissolved in water (25 ml) were added to reduce

osmium to Os^{II}. The mixture was placed in the fridge to precipitate the product as a red-brown solid which was collected by filtration, rinsed with cold water, and dried under vacuum (0.2372 g, 0.34 mmol, 77% yield).

Synthesis of [Os(dmobpy)$_2$(pybu)Cl](PF$_6$)

$Os(dmobpy)_2Cl_2$ (0.1879 g, 0.27 mmol), 4-(pyridine-4-yl)butanoic acid 9.1% wt in ethylene glycol (0.4920 g, 0.27 mmol), and ethylene glycol (6.77 ml) were added to a round bottom flask fitted with a reflux condenser. The flask was evacuated, and the atmosphere replaced with nitrogen three times while stirring. The mixture was heated to 100 °C for 2 hours while stirring and the solution turned a deep red color. Aqueous HPF_6 0.03 M (17 ml) was added and the solution was stored in a fridge overnight to precipitate the product as a brown solid which was collected by vacuum filtration and dried under vacuum (0.1487 g, 0.15 mmol, 57% yield). At this point the product was not significantly soluble in most solvents and so NMR was too difficult to reasonably obtain. The product identity was verified by MALDI mass spectra.

Synthesis of [Os(dmobpy)$_2$(pybu)I]I

[Os(dmobpy)2(pybu)Cl](PF6) (0.0401 g, 0.041 mmol), NaI, (0.1246 g, 0.83 mmol) and ethylene glycol (1.1213 g) were added to a round bottom flask fitted with a reflux condenser. The flask was evacuated, and the atmosphere replaced with nitrogen three times while stirring. The mixture was heated to reflux for 35 minutes while stirring and the solution turned a deep purple-black color. The mixture was allowed to cool to room temperature and NaI (1.2 g) and water (4 ml) were added. The solution was left in a fridge for several hours. More water was added and let freeze overnight in the freezer. DCM was added and a precipitate formed, between clear organic and aqueous layers. The brown precipitate was collected by filtration and dried under vacuum (0.0193 g, 0.019 mmol, 45% yield).

Synthesis of $Os(dmbpy)_2Cl_2$

A mixture of sodium hexachloroosmate dihydrate (0.1033 g, 0.21 mmol), 4,4'-dimethyl-2,2'-bipyridine (dmbpy, 0.0755 g, 0.41 mmol), and ethylene glycol (2.5 ml) were added to a round bottom flask fitted with a reflux condenser. The osmium compound, which is initially a red solid, dissolves to form a green solution. The flask was evacuated, and the atmosphere replaced with nitrogen three times while stirring. The first evacuation was held until yellow-green bubbles were no longer observed. Under a blanket of nitrogen, the mixture was refluxed for 2 h. The solution changes color to a red-brown color. After cooling to room temperature, water (12 ml) were added. The mixture was placed in the fridge to precipitate the product as a red-black solid which was collected by filtration, rinsed with cold water, and dried under vacuum (0.0476 g, 0.076 mmol, 35% yield).

Synthesis of $Os(dmbpy)_2I_2$

$Os(dmbpy)_2Cl_2$ (0.0418 g 0.066 mmol), NaI (0.20 g, 1.3 mmol) and ethylene glycol (1.82 g) were added to a round bottom flask fitted with a reflux condenser. The flask was evacuated, and the atmosphere replaced with nitrogen three times while stirring. Under a blanket of nitrogen, the mixture was refluxed for 2 h. The solution changes color to a purple-black color and purple black precipitate formed. After cooling to room temperature, sodium hydrosulfite (0.032 g) dissolved in water (8 ml) were added to reduce osmium to Os^{II}. The precipitate was collected by vacuum filtration and dried under vacuum (0.0299 g, .037 mmol, 55% yield). The identity was verified by MALDI.

Synthesis of $[Os(dmbpy)_2(pybu)I]I$

$Os(dmbpy)_2I_2$ (0.0262 g, 0.032 mmol), 4-(pyridine-4-yl)butanoic acid 9.1% wt in ethylene glycol (0.0676 g, 0.037 mmol), and ethylene glycol (6.77 ml) were added to a round bottom flask fitted with a reflux condenser. The flask was evacuated, and the atmosphere

replaced with nitrogen three times while stirring. Under a blanket of nitrogen, the mixture was refluxed for 2 h and then cooled to room temperature. Water (3.1498 g) and NaI (1.0379) were added and an oily red-purple "wine colored" precipitate formed which was collected by vacuum filtration and dried under vacuum (0.0312 g, 0.032 mmol, 99% crude yield). The product may have been contaminated with starting material and ethylene glycol, however, neither of these materials can bind to a film so the material bound to the film should be pure.

Synthesis of $Na_2[Os(6,6'\text{-dcbpy})Cl_2]$

6,6'-dicarboxy-2,2'-bipyridine (0.0977 g, 0.40 mmol), K_2CO_3 (0.0425 g, 0.40 mmol), and ethylene glycol (4 ml) were added to a 100 ml round bottom flask and stirred under vacuum. Bubbles formed and the solids dissolved to form a pale pink solution. sodium hexachloroosmate dihydrate (0.1948 g, 0.40 mmol) was added and washed in with ethylene glycol (2 ml). The flask was evacuated, and the atmosphere replaced with nitrogen four times while stirring. The first evacuation was held until yellow-green bubbles were no longer observed. Under a blanket of nitrogen, the mixture was refluxed for 3 h and allowed to return to room temperature. The solution turned a deep red-purple. Ethanol (15 ml) was added and the solution stirred and sonicated. Diethyl ether (80 ml) was added and the solution stirred, sonicated, and placed in the freezer overnight. The resulting precipitate was collected by filtration and dried under vacuum (0.0470 g, 0.093 mmol, 23% yield).

Synthesis of $Os(6,6'\text{-dcbpy})(pybu)_2$

$Na_2[Os(6,6'\text{-dcbpy})Cl_2]$ (0.0431 g, 0.086 mmol), 4-(pyridine-4-yl)butanoic acid 9.1% wt in ethylene glycol (0.3148 g, 0.17 mmol), and ethylene glycol (2 ml) were added to a round bottom flask fitted with a reflux condenser. The flask was evacuated, and the atmosphere replaced with nitrogen three times while stirring. Under a blanket of nitrogen, the mixture was refluxed for 5 h and then cooled to room temperature. Water (19 ml) and HCl 1 N solution (1 ml)

was added and the solution placed in a freezer overnight to separate the product as a red black oil which was collected by decanting the aqueous layer and drying under vacuum (0.0181 g, 0.024 mmol, 28% yield).

1H NMR (499 MHz DMSO-D_6) δ 8.95 (d, 2H), δ 8.80 (d, 2H), δ 7.82 (d, 2H), δ 8.70 (t, 2H), δ 7.50 (t, 2H), δ 7.23 (d, 2H), δ 4.83 (t, 2H), δ 4.05 (broad s, 2H), δ 3.55 (p, 2H), δ 2.56 (t, 2H).

PEDOT electropolymerization

Seven consecutive cyclic voltammograms of 0.05 M EDOT and 0.1 M tetra-n-butyl ammonium perchlorate ($TBAClO_4$) solutions in tetrahydrofuran (THF) were performed, cycling between 0 and +2 V versus reference at 50 mV s^{-1} with a plain FTO glass working electrode (WE), Ag/AgCl pseudo-reference electrode (RE) and platinum wire counter electrode (CE).

PEDOT Photoelectropolymerization

Dyed DSSC type electrodes were prepared according the procedures outlined in chapter 2. The dyed slides were used as the working electrode, the reference was a Ag/AgCl pseudo-reference electrode, the counter electrode was platinum mesh, and the solution was 0.05 M EDOT solution in 100 mM $LiClO_4$ in acetonitrile. A 60 second open circuit voltage was performed to determine if the electrodes were attached correctly. Chronoamperometry was performed at +0.2 V vs reference for 30 minutes while under illumination by an ELH projector lamp bulb passed through a 3” water filter. These results were compared with measurements without EDOT and without light to determine that current increased due to photoelectropolymerization when both EDOT and light were present. The films also visibly darkened due to the presence of PEDOT polymer which is dark blue. Solar cells were then prepared and tested according to the procedures outlined in chapter 2.

Cyclic Voltammetry and PEIS of PEDOT and Platinum coated FTO Electrodes

FTO glass slides (TEC15) were cut to 0.5 cm × 4 cm dimensions. The slides to be coated with PEDOT had chemical resistant epoxy (Hysol 1C) was applied from 1 cm to 3.5 cm down the slides and cured at 70 °C overnight. The slides were cleaned by sonication in aqueous alconox solution for 15 minutes, rinsed with water and ethanol, sonicated in ethanol for 15 minutes, and rinsed with ethanol. The slides to be coated with PEDOT were placed in a 0.05 M EDOT solution in 100 mM $LiClO_4$ in acetonitrile as a working electrode. The counter electrode was platinum mesh and the reference electrode was an Ag/AgCl wire pseudo-reference. Chronoamperometry was used to apply 1.2 V vs Ag/AgCl until 6 mC of charge had passed, producing slides that were faintly blue. To slides to be platinized were cleaned by sonication while still free of chemical resistant epoxy. 1 drop of hexachloroplatinic acid 2 mg ml^{-1} in methanol was applied to each slide and allowed to dry. The slides were then calcined at 300 °C for 15 minutes. The chemical resistant epoxy was then applied over the same area as the PEDOT slides and cured overnight at 70 °C.

Slides were placed in a Lewis electrolyte solution as a working electrode with a pt mesh counter electrode and Ag/AgCl quasi-reference electrode. The Ag/AgCl quasi-reference electrode decomposed in the solution such that it produced a potential equal to the solution potential. Cyclic voltammetry was performed from -1 V to +1 V versus the solution potential at a scan rate of 100 mV s^{-1}. PEIS was performed according to the default Biologic settings.

Cyclic Voltammetry of Pt(NCN)I

0.05 mM solutions of Pt(NCN)I and Pt(NCN)Cl were prepared in 100 mM $LiClO_4$ in acetonitrile solution. A freshly polished 2 mm diameter Pt button was used at the working electrode, an SCE was used as reference electrode, and a piece of platinum mesh as counter

electrode. The counter electrode was freshly cleaned before the measurement by immersion in HNO_3 (conc.). A 30 second open circuit voltage measurement was performed to determine if the electrodes were attached correctly. Cyclic voltammetry was obtained from 0 to 1 V vs SCE at a scan rate of 10 mV s^{-1}. A PEIS measurement was then performed to determine the solution resistance, however the displayed data is not corrected for solution resistance.

Cyclic Voltammetry of [Os(trpy)(bpy)X]X

A 0.5 mM solution of the redox active substrate, LiI or [Os(trpy)(bpy)X]X, in 100 mM $LiClO_4$ in acetonitrile was prepared. A freshly polished 10 μm diameter platinum ultimicroelectrode was used as the working electrode, an SCE was used as reference electrode, and a piece of platinum mesh as counter electrode. A 30 second open circuit voltage measurement was performed to determine if the electrodes were attached correctly. Cyclic voltammetry was obtained from 0 to 1 V vs SCE at a scan rate of 1 mV s^{-1}.

Cylic Voltammetry of $[Os(dmbpy)_2(pybu)I]I$ and $Os(6,6'\text{-}dcbpy)(pybu)_2$

TiO_2 films on FTO glass substrates with dimension 0.7 cm × 7.0 cm were prepared as described in chapter 2. Films were dyed overnight in solutions containing 2 mM $[Os(dmbpy)_2(pybu)I]I$ or $Os(6,6'\text{-}dcbpy)(pybu)_2$ in 50:50 v/v methanol:acetonitrile. The working electrode was the dyed slide, the counter electrode was platinum mesh, the reference electrode was an SCE, and the supporting solution was 100 mM $LiClO_4$ in acetonitrile. A 30 second open circuit voltage measurement was performed to determine if the electrodes were attached correctly. Cyclic voltammetry was obtained over the displayed range at scan rates of 100, 50, 20, and 10 mV s^{-1}, performing three sweeps at each scan rate. PEIS was also performed using the default settings. After each set of cyclic voltammograms was performed, LiI 100 mM in acetonitrile was injected such that the solution concentration of LiI was 0.5, 1, 2, 5, 10, and 25

mM after injections 1, 2, 3, 4, 5, and 6 respectively. After each injection the open circuit, cyclic voltammetry, and PEIS measurements were performed again.

Preparation of Solar Cells with [Os(dmbpy)$_2$(pybu)I]I and Os(6,6'-dcbpy)(pybu)$_2$

Dyed TiO_2 films on FTO were prepared according to the methods outlined in chapter 2 but skipping the $TiCl_4$ deposition step. For cells dyes with only [Os(dmbpy)$_2$(pybu)I]I or Os(6,6'-dcbpy)(pybu)$_2$ the films were allowed to dye overnight similar other dyes. For cells dyed with [Os(dmbpy)$_2$(pybu)I]I or Os(6,6'-dcbpy)(pybu)$_2$ and Osppy or OsN3, the films were immersed in the [Os(dmbpy)$_2$(pybu)I]I or Os(6,6'-dcbpy)(pybu)$_2$ dyeing solution for only 1 minute to produce only palely colored films. UV-vis measurements of these films suggest that catalyst surface coverage is about 10%, much higher than the desired coverage of 1%. Films were washed by being immersed twice in acetonitrile, and then immersed in Osppy or OsN3 dye solutions overnight. Cell fabrication and testing from this point onwards was the same as the methods outlined in chapter 2.

Additional Figures

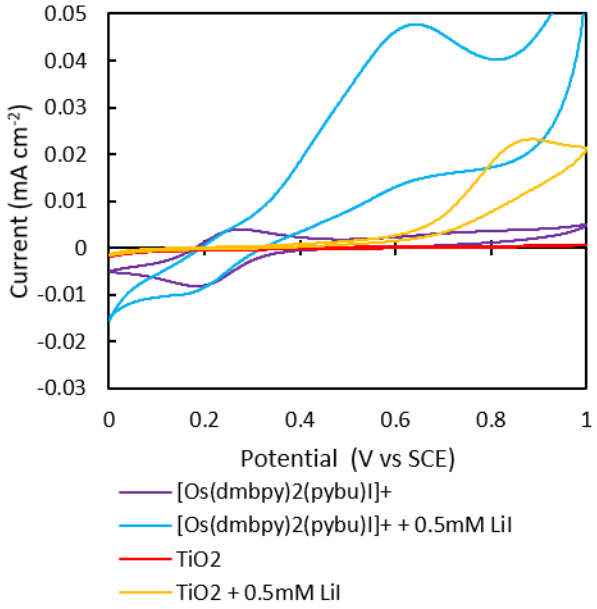

Figure 71: Cyclic voltammograms of mesoporous TiO_2 films with and without $[Os(dmbpy)_2(pybu)I]^+$ in 100 mM $LiClO_4$ solution in acetonitrile with and without the addition of 0.5 mM LiI. Notice that in the absence of $[Os(dmbpy)_2(pybu)I]^+$, the oxidation of LiI onsets at a higher potential than in the presence of $[Os(dmbpy)_2(pybu)I]^+$.

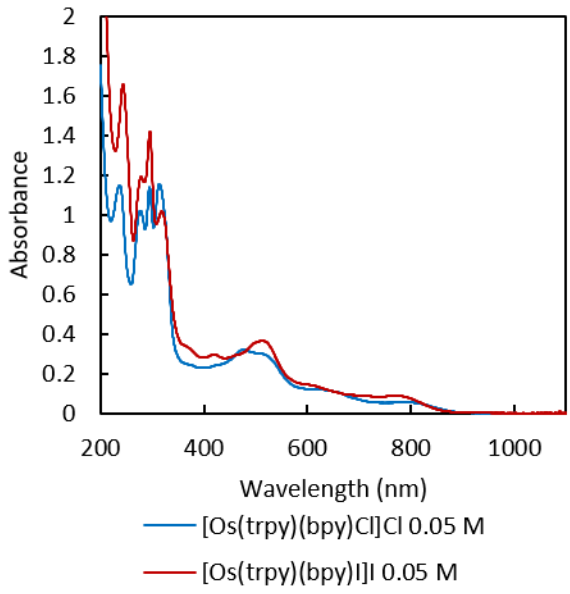

Figure 72: UV-vis electronic absorption spectra of 0.05 M solutions of [Os(trpy)(bpy)Cl]Cl and [Os(trpy)(bpy)I]I in acetonitrile.

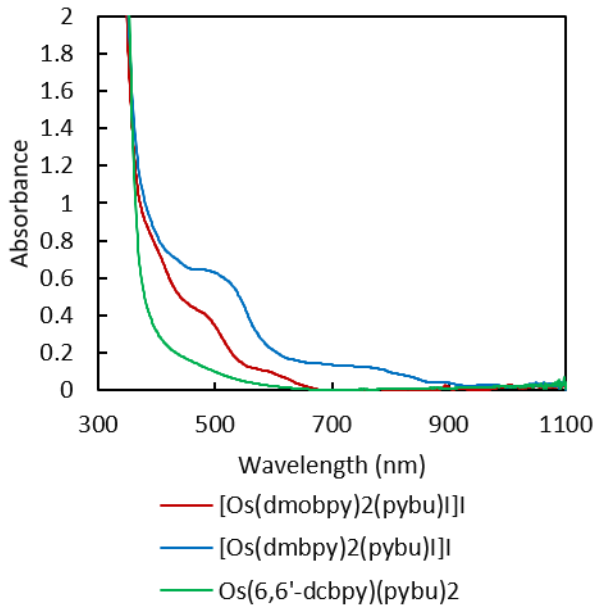

Figure 73: UV-vis electronic absorption spectra of mesoporous TiO_2 films dyed with osmium polypyridyl iodide oxidation catalysts.

My Contribution to Science and Future Outlook

My Contribution to Science

I synthesized and characterized four infrared-absorbing osmium polypyridyl dyes for use in dye sensitized solar cells, abbreviated as OsN3, Osppy, OsI_2, and $OsCl_2$. OsN3 and $OsCl_2$ were previously reported by Nate Lewis's group and Osppy was originally synthesized by Hsiang-Yun Chen but not publicly reported. To the best of my knowledge I am the first to synthesize OsI_2 and the first to use $OsCl_2$ and OsI_2 in DSSCs. To the best of my knowledge $OsCl_2$, with an optical pseudo-bandgap of 1.06, is the dye that absorbs farthest into the infrared of any reported DSSC dye.

I was able to justify and harmonize the differences in apparent diffusion coefficients measured for self-exchange electron transfer of dyes bound to TiO_2 films using potentials step chronoamperometry, potential step chronoabsorptometry, and cyclic voltammetry methods. This required modification of the Nernst equation with a non-ideality factor which can be measured by steady state stepwise potential step chronoabsorptometry or by cyclic voltammetry. It also required correct use of dying density determination techniques to only account for electroactive dyes.

I applied foot-of-the-wave analysis to dyes bound to mesoporous TiO_2 films with substrate in solution. This required use of the same Nernstian non-ideality factor used to justify differences in apparent diffusion coefficient measurements. This allowed determination of second-order electron-tranfer rate constants for 1,1'-dimethyl ferrocene and lithium iodide to oxidized OsN3, $OsCl_2$, and OsI_2 dyes. To the best of my knowledge I am the first to apply this

technique to molecules bound to a mesoporous semiconducting film and to apply this technique to readily oxidized species such as ferrocenes and iodide.

I used nanosecond transient absorption and nanosecond microwave conductivity to determine that the reason my infrared-absorbing do not produce highly efficient cells is that dyes are not quickly regenerated by I^-. This conclusion was expected and is not particularly exciting. However, to the best of my knowledge, I am the second to report microwave conductivity measurements of systems with a semiconducting solid to liquid electrolyte interface and the first to do this measurement using X band microwaves inside a resonant cavity.

Future Outlook

As silicon solar cells continue to improve in efficiency and price, dye-sensitized solar cells become less and less of a commercial possibility and more and more of an academic curiosity. Building a highly efficient DSSC with an infrared absorbing dye would be a great way to publish papers and train students, but not a great way to get funding or save the world. That being said, if your aim is to publish papers and train students then the osmium polypyridyl dyes in this thesis are a good starting point. The primary challenge to these dyes is to find a redox electrolyte that regenerates dyes quickly at low overpotential but does not cause shunting. Even though I attempted to make a catalyst to oxidize I^- at low overpotential, I no longer believe that this is the right approach. A better approach would be to use a one-electron transfer reversible redox shuttle, which implies fast electron transfer rates and low regeneration overpotential, and then to rigorously protect the TiO_2 surface from the redox shuttle by post-modification. A possible intermediate step would be to use a copper or cobalt redox shuttle that is intermediate in

speed, reversibility, and required protection compared to a fully reversible shuttle and a the I^-/I_3^- redox shuttle.

The diffusion coefficient project is done. It should mostly serve as a technical reference for future work.

Foot-of-the-wave analysis of molecules bound to a semiconducting or resistive film is a powerful technique. It allows quantitative analysis and mechanistic elucidation of interactions between bound catalysts and substrates in solution. Because it is selective to bound catalysts, substrates can be used which are electroactive at most other materials, such as ferrocenes, metal-polypyridyl complexes, halides, and other fast or one-electron transfer substrates. It does not apply only to DSSC research, but could also be used with solar fuels type research, or almost any molecular electrocatalyst research. A good DSSC study would be to use a variety of redox shuttles with a variety of infrared absorbing dyes and determine which redox shuttles are kinetically compatible with which dyes. A good solar fuels study would be to take surface bound catalysts and sensitizers in particle reactor schemes and test their selectivity to water oxidation and reduction compared to electrolyte oxidation and reduction. I really hope to see this take off and be used to learn interesting things in a variety of fields.

Microwave conductivity measurements of semiconductor-liquid electrolyte interfaces is more limited in scope but could be used to perform some impactful studies. It seems like it would be useful mostly to the DSSC and solar fuels communities. For DSSCs a good future experiment would be to measure injected electron lifetimes in TiO_2 with different types of protecting layers to see what protection methods are best for a given redox shuttle-dye pairing. For solar fuels it could be used to measure the excited electron lifetimes in semiconductors such as bismuth vanadate or doped titanium dioxide under different conditions.

In conclusion, this work was focused on dye-sensitized solar cells and provides plenty of avenues for future DSSC papers, however, the techniques discuessed here could be applied to solar fuels research, or any sort of electrocatalysis research and will hopefully outlive the DSSC research bubble.

References

(1) Kalyanasundaram, K.; Hagfeldt, A.; Boschloo, G.; Sun, L.; Kloo, L.; Pettersson, H. *Dye-Sensitized Solar Cells*; EPFL Press, 2010; Vol. 110.

(2) Lee, H. M.; Yoon, J. H. Power Performance Analysis of a Transparent DSSC BIPV Window Based on 2 Year Measurement Data in a Full-Scale Mock-Up. *Appl. Energy* **2018**, *225* (April), 1013–1021.

(3) Gong, J.; Sumathy, K.; Qiao, Q.; Zhou, Z. Review on Dye-Sensitized Solar Cells (DSSCs): Advanced Techniques and Research Trends. *Renew. Sustain. Energy Rev.* **2017**, *68* (December 2015), 234–246.

(4) Jacoby, M. The Future of Low-Cost Solar Cells. *Chemical & Engineering News*. 2016, pp 30–35.

(5) Hao, Y.; Yang, W.; Zhang, L.; Jiang, R.; Mijangos, E.; Saygili, Y.; Hammarström, L.; Hagfeldt, A.; Boschloo, G. A Small Electron Donor in Cobalt Complex Electrolyte Significantly Improves Efficiency in Dye-Sensitized Solar Cells. *Nat. Commun.* **2016**, *7*, 1–8.

(6) Zhang, L.; Cole, J. M. Anchoring Groups for Dye-Sensitized Solar Cells. *ACS Appl. Mater. Interfaces* **2015**, *7* (6), 3427–3455.

(7) Gibson, E. A.; Smeigh, A. L.; Pleux, L. Le; Hammarstr, L.; Odobel, F.; Boschloo, G.; Hagfeldt, A. Cobalt Polypyridyl-Based Electrolytes for p-Type Dye-Sensitized Solar Cells. *J. Phys. Chem. C* **2011**, *115*, 9772–9779.

(8) Ayalew, W. A.; Ayele, D. W. Dye-Sensitized Solar Cells Using Natural Dye as Light-Harvesting Materials Extracted from Acanthus Sennii Chiovenda Flower and Euphorbia Cotinifolia Leaf. *J. Sci. Adv. Mater. Devices* **2016**, *1* (4), 488–494.

(9) Gibson, E. A.; Le Pleux, L.; Fortage, J.; Pellegrin, Y.; Blart, E.; Odobel, F.; Hagfeldt, A.; Boschloo, G. Role of the Triiodide/Iodide Redox Couple in Dye Regeneration in p-Type Dye-Sensitized Solar Cells. *Langmuir* **2012**, *28* (15), 6485–6493.

(10) Inganäs, O. Organic Photovoltaics over Three Decades. *Adv. Mater.* **2018**, *30* (35), 1–26.

(11) Ren, W.; Zhuang, H.; Bao, Q.; Miao, S.; Li, H.; Lu, J.; Wang, L. Enhancing the Coplanarity of the Donor Moiety in a Donor-Acceptor Molecule to Improve the Efficiency of Switching Phenomenon for Flash Memory Devices. *Dye. Pigment.* **2014**, *100* (1), 127–134.

(12) Mathew, S.; Yella, A.; Gao, P.; Humphry-Baker, R.; Curchod, B. F. E.; Ashari-Astani, N.; Tavernelli, I.; Rothlisberger, U.; Nazeeruddin, M. K.; Grätzel, M. Dye-Sensitized Solar Cells with 13% Efficiency Achieved through the Molecular Engineering of Porphyrin Sensitizers. *Nat. Chem.* **2014**, *6* (3), 242–247.

(13) Clifford, J. N.; Yahioglu, G.; Milgrom, L. R.; Durrant, J. R. Molecular Control of Recombination Dynamics in Dye Sensitised Nanocrystalline TiO_2 Films. *Chem. Commun.* **2002**, No. 12, 1260–1261.

(14) Haque, S. A.; Tachibana, Y.; Klug, D. R.; Durrant, J. R. Charge Recombination Kinetics in Dye-Sensitized Nanocrystalline Titanium Dioxide Films under Externally Applied Bias. *J. Phys. Chem. B* **1998**, *102* (10), 1745–1749.

(15) Daeneke, T.; Kwon, T.-H.; Holmes, A. B.; Duffy, N. W.; Bach, U.; Spiccia, L. High-Efficiency Dye-Sensitized Solar Cells with Ferrocene-Based Electrolytes. *Nat. Chem.* **2011**, *3* (3), 213–217.

(16) Choi, H.; Nahm, C.; Kim, J.; Moon, J.; Nam, S.; Jung, D.-R.; Park, B. The Effect of TiCl4-Treated TiO2 Compact Layer on the Performance of Dye-Sensitized Solar Cell. *Curr. Appl. Phys.* **2012**, *12* (3), 737–741.

(17) Rowley, J. G.; Farnum, B. H.; Ardo, S.; Meyer, G. J. Iodide Chemistry in Dye-Sensitized Solar Cells: Making and Breaking I-I Bonds for Solar Energy Conversion. *J. Phys. Chem. Lett.* **2010**, *1* (20), 3132–3140.

(18) Daeneke, T.; Mozer, A. J.; Kwon, T.-H.; Duffy, N. W.; Holmes, A. B.; Bach, U.; Spiccia, L. Dye Regeneration and Charge Recombination in Dye-Sensitized Solar Cells with Ferrocene Derivatives as Redox Mediators. *Energy Environ. Sci.* **2012**, *5* (5), 7090.

(19) Nazeeruddin, M. K.; Kay, A.; Miiller, E.; Liska, P.; Vlachopoulos, N.; Gratzel, M. Conversion of Light to Electricity by Cis-X,$_2$(2,2'-Bipyridyl-4-4'-Dicarboxylate)Ruthenium(II) Charge-Transfer Sensitizers (X = Cl^-, Br^-, I^-, CN^-, and SCN^-) on Nanocrystalline Ti0<sub>2</Sub. *J. Am. Chem. Soc.* **1993**, *115* (14), 6382–6390.

(20) Boschloo, G.; Hagfeldt, A. Characteristics of the Iodide / Triiodide Redox Mediator in Dye-Sensitized Solar Cells. *Acc. Chem. Res.* **2009**, *42* (11), 1819–1826.

(21) Richards, C. E.; Anderson, A. Y.; Martiniani, S.; Law, C.; O'Regan, B. C. The Mechanism of Iodine Reduction by TiO Electrons and the Kinetics of Recombination in Dye-Sensitized Solar Cells. *J. Phys. Chem. Lett.* **2012**, *3* (15), 1980–1984.

(22) Donnan, F. G. Theorie Der Membrangleichgewichte Und Membranpotentiale Bei Vorhandensein von Nicht Dialyseirenden Elektrolyten. Ein Beitrag Zur Physikalisch-Chemichen Physiologie. *Berichte der Bunsengesellschaft fur Phys. Chemie* **1911**.

(23) Kakiage, K.; Aoyama, Y.; Yano, T.; Oya, K.; Fujisawa, J.; Hanaya, M. Highly-Efficient Dye-Sensitized Solar Cells with Collaborative Sensitization by Silyl-Anchor and Carboxy-Anchor Dyes. *Chem. Commun.* **2015**, *51* (88), 15894–15897.

(24) Safdari, M.; Lohse, P. W.; Häggman, L.; Frykstrand, S.; Högberg, D.; Rutland, M.; Asencio, R. A.; Gardner, J.; Kloo, L.; Hagfeldt, A.; et al. Investigation of Cobalt Redox Mediators and Effects of TiO2 Film Topology in Dye-Sensitized Solar Cells. *RSC Adv.* **2016**, *6* (61), 56580–56588.

(25) Saygili, Y.; Stojanovic, M.; Flores-Díaz, N.; Zakeeruddin, S. M.; Vlachopoulos, N.; Grätzel, M.; Hagfeldt, A. *Metal Coordination Complexes as Redox Mediators in Regenerative Dye-Sensitized Solar Cells*; 2019; Vol. 7.

(26) Shockley, W.; Queisser, H. J. Detailed Balance Limit of Efficiency of P-n Junction Solar Cells. *J. Appl. Phys.* **1961**, *32* (3), 510–519.

(27) Rühle, S. Tabulated Values of the Shockley-Queisser Limit for Single Junction Solar Cells. *Sol. Energy* **2016**, *130*, 139–147.

(28) Green, M. A. The Path to 25% Silicon Solar Cell Efficiency: History of Silicon Cell Evolution. *Prog. Photovoltaics* **2009**, *17*, 183–189.

(29) Solbrand, A.; Henningsson, A.; Södergren, S.; Lindström, H.; Hagfeldt, A.; Lindquist, S. Charge Transport Properties in Dye-Sensitized Nanostructured TiO_2 Thin Film Electrodes Studied by Photoinduced Current Transients. *J. Phys. Chem. B* **1999**, *103* (7), 1078–1083.

(30) Gierszewski, M.; Glinka, A.; Gradzka, I.; Jancelewicz, M.; Ziółek, M. Effects of Post-Assembly Molecular and Atomic Passivation of Sensitized Titania Surface: Dynamics of

Electron Transfer Measured from Femtoseconds to Seconds. *ACS Appl. Mater. Interfaces* **2017**, *9* (20), 17102–17114.

(31) Kavan, L. Nanocrystalline TiO_2 (Anatase) Electrodes: Surface Morphology, Adsorption, and Electrochemical Properties. *J. Electrochem. Soc.* **1996**, *143* (2), 394.

(32) Gregg, B. A. Interfacial Processes in the Dye-Sensitized Solar Cell. *Coord. Chem. Rev.* **2004**, *248* (13–14), 1215–1224.

(33) Nazeeruddin, M. K.; Baranoff, E.; Grätzel, M. Dye-Sensitized Solar Cells: A Brief Overview. *Sol. Energy* **2011**, *85* (6), 1172–1178.

(34) Park, J.; Viscardi, G.; Barolo, C.; Barbero, N. Near-Infrared Sensitization in Dye-Sensitized Solar Cells. *Chim. Int. J. Chem.* **2013**, *67* (3), 129–135.

(35) Ito, S.; Murakami, T. N.; Comte, P.; Liska, P.; Grätzel, C.; Nazeeruddin, M. K.; Grätzel, M. Fabrication of Thin Film Dye Sensitized Solar Cells with Solar to Electric Power Conversion Efficiency over 10%. *Thin Solid Films* **2008**, *516* (14), 4613–4619.

(36) Nazeeruddin, M. K.; Zakeeruddin, S. M.; R., H.-B.; Jirousek, M.; Liska, P.; Vlachopoulos, N.; Shklover, V.; Fischer, C.-H.; Gratzel, M. Acid-Base Equilibria of (2,2'-Bipyridyl-4,4'-Dicarboxylic Acid)Ruthenium(II) Complexes and the Effect of Protonation on Charge-Transfer Sensitization of Nanocrystalline Titania. *Inorg. Chem.* **1999**, *38* (26), 6298–6305.

(37) Sauvé, G.; Cass, M. E.; Coia, G.; Doig, S. J.; Lauermann, I.; Pomykal, K. E.; Lewis, N. S. Dye Sensitization of Nanocrystalline Titanium Dioxide with Osmium and Ruthenium Polypyridyl Complexes. *J. Phys. Chem. B* **2000**, *104*, 6821–6836.

(38) Bomben, P. G.; Robson, K. C. D.; Koivisto, B. D.; Berlinguette, C. P. Cyclometalated Ruthenium Chromophores for the Dye-Sensitized Solar Cell. *Coord. Chem. Rev.* **2012**, *256*, 1438–1450.

(39) Bomben, P. G.; Robson, K. C. D.; Sedach, P. A.; Berlinguette, C. P. On the Viability of Cyclometalated Ru(II) Complexes for Light-Harvesting Applications. *Inorg. Chem.* **2009**, *48* (20), 9631–9643.

(40) Nazeeruddin, M. K.; Kay, A.; Miiller, E.; Liska, P.; Vlachopoulos, N.; Gratzel, M.; Lausanne, C.-; April, R. Conversion of Light to Electricity by Cis-X2Bis(2,2'-Bipyridyl-4,4'dicarboxylate)Ruthenium(II) Charge-Transfer Sensitizers (X = Cl^-, Br^-, I^-, CN^-, and SCN^-) on Nanocrystalline TiO_2 Electrod. *J. Am. Chem. Soc.* **1993**, *115* (4), 6382–6390.

(41) Kuciauskas, D.; Monat, J. E.; Villahermosa, R.; Gray, H. B.; Lewis, N. S.; Mccusker, J. K. Transient Absorption Spectroscopy of Ruthenium and Osmium Polypyridyl Complexes Adsorbed onto Nanocrystalline TiO2 Photoelectrodes. *J. Phys. Chem. B* **2002**, *106*, 9347–9358.

(42) Lumpkin, R. S.; Kober, E. M.; Worl, L. A.; Murtaza, Z.; Meyer, T. J. Metal-to-Ligand Charge-Transfer (MLCT) Photochemistry. Experimental Evidence for the Participation of a Higher Lying MLCT State in Polypyridyl Complexes of Ruthenium(II) and Osmium(II). *J. Phys. Chem.* **1990**, *94* (1), 239–243.

(43) Shaw, G. B.; Styers-Barnett, D. J.; Gannon, E. Z.; Granger, J. C.; Papanikolas, J. M. Interligand Electron Transfer Dynamics in $[Os(Bpy)_3]^{2+}$: Exploring the Excited State Potential Surfaces with Femtosecond Spectroscopy. *J. Phys. Chem. A* **2004**, *108* (23), 4998–5006.

(44) Tauc, J.; Grigorovici, R.; Vancu, A. Optical Properties and Electronic Structure of Amorphous Germanium. *Phys. Status Solidi* **1966**, *15*, 627–637.

(45) Dongol, M.; El-Nahass, M. M.; El-Denglawey, A.; Elhady, A. F.; Abuelwafa, A. A.

Optical Properties of Nano 5,10,15,20-Tetraphenyl-21H,23H-Prophyrin Nickel (II) Thin Films. *Curr. Appl. Phys.* **2012**, *12* (4), 1178–1184.

(46) Elgrishi, N.; Rountree, K. J.; McCarthy, B. D.; Rountree, E. S.; Eisenhart, T. T.; Dempsey, J. L. A Practical Beginner's Guide to Cyclic Voltammetry. *J. Chem. Educ.* **2018**, *95* (2), 197–206.

(47) Rahimi, N.; Pax, R. A.; Gray, E. M. A. Review of Functional Titanium Oxides. I: TiO2and Its Modifications. *Prog. Solid State Chem.* **2016**, *44* (3), 86–105.

(48) Brogdon, P.; Cheema, H.; Delcamp, J. H. Near-Infrared-Absorbing Metal-Free Organic, Porphyrin, and Phthalocyanine Sensitizers for Panchromatic Dye-Sensitized Solar Cells. *ChemSusChem* **2018**, *11* (1), 86–103.

(49) Li, J. Y.; Chen, C. Y.; Ho, W. C.; Chen, S. H.; Wu, C. G. Unsymmetrical Squaraines Incorporating Quinoline for near Infrared Responsive Dye-Sensitized Solar Cells. *Org. Lett.* **2012**, *14* (21), 5420–5423.

(50) Chen, H. Y.; Ardo, S. Direct Observation of Sequential Oxidations of a Titania-Bound Molecular Proxy Catalyst Generated through Illumination of Molecular Sensitizers. *Nat. Chem.* **2018**, *10* (1), 17–23.

(51) Brennaman, M. K.; Dillon, R. J.; Alibabaei, L.; Gish, M. K.; Dares, C. J.; Ashford, D. L.; House, R. L.; Meyer, G. J.; Papanikolas, J. M.; Meyer, T. J. Finding the Way to Solar Fuels with Dye-Sensitized Photoelectrosynthesis Cells. *J. Am. Chem. Soc.* **2016**, *138*, 13085–13102.

(52) Cannavale, A.; Cossari, P.; Eperon, G. E.; Colella, S.; Fiorito, F.; Gigli, G.; Snaith, H. J.; Listorti, A. Forthcoming Perspectives of Photoelectrochromic Devices: A Critical Review. *Energy Environ. Sci.* **2016**, *9*, 2682–2719.

(53) Hu, K.; Robson, K. C. D.; Beauvilliers, E. E.; Schott, E.; Zarate, X.; Arratia-perez, R.; Berlinguette, C. P.; Meyer, G. J. Intramolecular and Lateral Intermolecular Hole Transfer at the Sensitized TiO_2 Interface. *J. Am. Chem. Soc.* **2014**, *136*, 1034–1046.

(54) Bisquert, J.; Fabregat-Santiago, F.; Mora-Sero, I.; Garcia-Belmonte, G.; Barea, E. M.; Palomares, E. A Review of Recent Results on Electrochemical Determination of the Density of Electronic States of Nanostructured Metal-Oxide Semiconductors and Organic Hole Conductors. *Inorganica Chim. Acta* **2008**, *361*, 684–698.

(55) Bisquert, J.; Barcia-Belmonte, G.; Garcia-Canadas, J. Effects of the Gaussian Energy Dispersion on the Statistics of Polarons and Bipolarons in Conducting Polymers. *J. Chem. Phys.* **2004**, *120*, 6726–6733.

(56) Ardo, S.; Achey, D.; Morris, A. J.; Abrahamsson, M.; Meyer, G. J. Non-Nernstian Two-Electron Transfer Photocatalysis at Metalloporphyrin–TiO_2 Interfaces. *J. Am. Chem. Soc.* **2011**, *133* (41), 16572–16580.

(57) Albery, W. J.; Boutelle, M. G.; Colby, P. J.; Hillman, A. R. The Kinetics of Electron Transfer in the Thionine-Coated Electrode. *J. Electroanal. Chem.* **1982**, *133*, 135–145.

(58) Smith, D. F.; Willman, K.; Kuo, K.; Murray, R. W. Chemically Modified Electrodes IV. Electrochemistry and Waveshape Analysis of Aminophenylferrocene Bonded to Acid Chloride Functionalized Ruthenium, Platinum, and Tin Oxide Electrodes. *J. Electroanal. Chem.* **1979**, *95*, 217–227.

(59) Bonhôte, P.; Gogniat, E.; Tingry, S.; Barbé, C.; Vlachopoulos, N.; Lenzmann, F.; Comte, P.; Grätzel, M. Efficient Lateral Electron Transport inside a Monolayer of Aromatic Amines Anchored on Nanocrystalline Metal Oxide Films. *J. Phys. Chem. B* **1998**, *102* (9),

1498–1507.

(60) Trammell, S. A.; Meyer, T. J. Diffusional Mediation of Surface Electron Transfer on TiO_2. *J. Phys. Chem. B* **1999**, *103*, 104–107.

(61) Papageorgiou, N.; Gratzel, M.; Enger, O.; Bonifazi, D.; Diederich, F. Lateral Electron Transport inside a Monolayer of Derivatized Fullerenes Anchored on Nanocrystalline Metal Oxide Films. *J. Phys. Chem. B* **2002**, *106*, 3813–3822.

(62) Moia, D.; Cappel, U. B.; Leijtens, T.; Li, X.; Telford, A. M.; Snaith, H. J.; Regan, B. C. O.; Nelson, J.; Barnes, P. R. F. The Role of Hole Transport between Dyes in Solid-State Dye- Sensitized Solar Cells. *J. Phys. Chem. C* **2015**, *119*, 18975–18985.

(63) Hu, K.; Meyer, G. J. Lateral Intermolecular Self-Exchange Reactions for Hole and Energy Transport on Mesoporous Metal Oxide Thin Films. *Langmuir* **2015**, *31* (41), 11164–11178.

(64) Ardo, S.; Meyer, G. J. Direct Observation of Photodriven Intermolecular Hole Transfer across TiO_2 Nanocrystallites: Lateral Self-Exchange Reactions and Catalyst Oxidation. *J. Am. Chem. Soc.* **2010**, *132* (27), 9283–9285.

(65) Ardo, S.; Meyer, G. J. Characterization of Photoinduced Self-Exchange Reactions at Molecule-Semiconductor Interfaces by Transient Polarization Spectroscopy: Lateral Intermolecular Energy and Hole Transfer Across Sensitized TiO_2 Thin Films. *J. Am. Chem. Soc.* **2011**, *133* (39), 15384–15396.

(66) Penner, R. M.; Gogotsi, Y. The Rising and Receding Fortunes of Electrochemists. *ACS Nano* **2016**, *10* (4), 3875–3876.

(67) Argazzi, R.; Murakami Iha, N. Y.; Zabri, H.; Odobel, F.; Bignozzi, C. A. Design of Molecular Dyes for Application in Photoelectrochemical and Electrochromic Devices Based on Nanocrystalline Metal Oxide Semiconductors. *Coord. Chem. Rev.* **2004**, *248*, 1299–1316.

(68) Moia, D.; Szumska, A.; Vaissier, V.; Planells, M.; Robertson, N.; O'Regan, B. C.; Nelson, J.; Barnes, P. R. F. Interdye Hole Transport Accelerates Recombination in Dye Sensitized Mesoporous Films. *J. Am. Chem. Soc.* **2016**, *138* (40), 13197–13206.

(69) Sampaio, R. N.; Mu, A. V; Polo, A. S.; Meyer, G. J. Correlation Between Charge Recombination and Lateral Hole-Hopping Kinetics in a Series of Cis-$Ru(Phen')(Dcb)(NCS)_2$ Dye- Sensitized Solar Cells. *ACS Appl. Mater. Interfaces* **2017**, *9*, 33446–33454.

(70) Sampaio, R. N.; DiMarco, B. N.; Meyer, G. J. Activation Energies for Electron Transfer from TiO_2 to Oxidized Dyes: A Surface Coverage Dependence Correlated with Lateral Hole Hopping. *ACS Energy Lett.* **2017**, *2*, 2402–2407.

(71) Wang, Q.; Zakeeruddin, S. M.; Cremer, J.; Bauerle, P.; Humphry-Baker, R.; Gratzel, M. Cross Surface Ambipolar Charge Percolation in Molecular Triads on Mesoscopic Oxide Films. *J. Am. Chem. Soc.* **2005**, *127*, 5706–5713.

(72) Galoppini, E.; Guo, W.; Zhang, W.; Hoertz, P. G.; Qu, P.; Meyer, G. J. Long-Range Electron Transfer across Molecule-Nanocrystalline Semiconductor Interfaces Using Tripodal Sensitizers. *J. Am. Chem. Soc.* **2002**, *124*, 7801–7811.

(73) Hoertz, P. G.; Staniszewski, A.; Marton, A.; Higgins, G. T.; Incarvito, C. D.; Rheingold, A. L.; Meyer, G. J. Toward Exceeding the Shockley-Queisser Limit: Photoinduced Interfacial Charge Transfer Processes That Store Energy in Excess of the Equilibrated Excited State. *J. Am. Chem. Soc.* **2006**, *128*, 8234–8245.

(74) Staniszewski, A.; Morris, A. J.; Ito, T.; Meyer, G. J. Conduction Band Mediated Electron Transfer Across Nanocrystalline TiO_2 Surfaces. *J. Phys. Chem. B* **2007**, *111*, 6822–6828.

(75) Li, X.; Nazeeruddin, M. K.; Thelakkat, M.; Barnes, P. R. F.; Vilar, R.; Durrant, J. R. Spectroelectrochemical Studies of Hole Percolation on Functionalised Nanocrystalline TiO_2 Films: A Comparison of Two Different Ruthenium Complexes. *Phys. Chem. Chem. Phys.* **2011**, *13* (4), 1575–1584.

(76) Wang, Q.; Zakeeruddin, S. M.; Nazeeruddin, M. K.; Humphry-baker, R.; Gratzel, M.; Nazeeruddin, K.; Humphry-baker, R. Molecular Wiring of Nanocrystals: NCS-Enhanced Cross-Surface Charge Transfer in Self-Assembled Ru-Complex Monolayer on Mesoscopic Oxide Films. *J. Am. Chem. Soc.* **2006**, *128*, 4446–4452.

(77) Moia, D.; Vaissier, V.; Lopez-Duarte, I.; Torres, T.; Nazeeruddin, M. K.; O'Regan, B. C.; Nelson, J.; Barnes, P. R. F. The Reorganization Energy of Intermolecular Hole Hopping between Dyes Anchored to Surfaces. *Chem. Sci.* **2014**, *5*, 281–290.

(78) Grätzel, M.; Kohle, O.; Meyer, A.; Meyer, T. The Photovoltaic Stability of Bis(Isothiocyanato)Ruthenium(11)-Bis-2,2'-Bipyridine-4,4-Dicarboxylic Acid and Related Sensitizers. *J. Nanosci. Nanotechnol.* **2009**, *9* (1), 221–229.

(79) Ardo, S.; Meyer, G. J. Photodriven Heterogeneous Charge Transfer with Transition-Metal Compounds Anchored to TiO_2 Semiconductor Surfaces. *Chem. Soc. Rev.* **2009**, *38* (1), 115–164.

(80) Nicholson, R. S.; Shain, I. Theory of Stationary Electrode Polarography: Single Scan and Cyclic Methods Applied to Reversible, Irreversible, and Kinetic Systems. *Anal. Chem.* **1964**, *36* (4), 706–723.

(81) Costentin, C.; Drouet, S.; Robert, M.; Sav?ant, J. M.; Savéant, J. M. Turnover Numbers, Turnover Frequencies, and Overpotential in Molecular Catalysis of Electrochemical Reactions. Cyclic Voltammetry and Preparative-Scale Electrolysis. *J. Am. Chem. Soc.* **2012**, *134* (27), 11235–11242.

(82) Savini, A.; Bucci, A.; Bellachioma, G.; Giancola, S.; Palomba, F.; Rocchigiani, L.; Rossi, A.; Suriani, M.; Zuccaccia, C.; MacChioni, A. New Iridium(III) Organometallic Complexes Bearing Strong Electron Donating Bidentate Ligands as Catalysts for Water Oxidation. *J. Organomet. Chem.* **2014**, *771*, 24–32.

(83) Elgrishi, N.; Chambers, M. B.; Fontecave, M. Turning It off! Disfavouring Hydrogen Evolution to Enhance Selectivity for CO Production during Homogeneous CO2reduction by Cobalt-Terpyridine Complexes. *Chem. Sci.* **2015**, *6* (4), 2522–2531.

(84) Matheu, R.; Neudeck, S.; Meyer, F.; Sala, X.; Llobet, A. Foot of the Wave Analysis for Mechanistic Elucidation and Benchmarking Applications in Molecular Water Oxidation Catalysis. *ChemSusChem* **2016**, *9* (23), 3361–3369.

(85) Costentin, C.; Robert, M.; Savéant, J. M. Catalysis of the Electrochemical Reduction of Carbon Dioxide. *Chem. Soc. Rev.* **2013**, *42* (6), 2423–2436.

(86) Yi, Y.; Weinberg, G.; Prenzel, M.; Greiner, M.; Heumann, S.; Becker, S.; Schlögl, R. Electrochemical Corrosion of a Glassy Carbon Electrode. *Catal. Today* **2017**, *295* (February), 32–40.

(87) Nazeeruddin, M. K.; Zakeeruddin, S. M.; R., H.-B.; Jirousek, M.; Liska, P.; Vlachopoulos, N.; Shklover, V.; Fischer, C.-H.; Gratzel, M.; Humphry-Baker, R.; et al. Acid−Base Equilibria of (2,2'-Bipyridyl-4,4'-Dicarboxylic Acid)Ruthenium(II) Complexes and the Effect of Protonation on Charge-Transfer Sensitization of Nanocrystalline Titania. *Inorg.*

Chem. **1999**, *38* (26), 6298–6305.
(88) Stroppolo, M. E.; Falconi, M.; Caccuri, A. M.; Desideri, A. Superefficient Enzymes. *Cell. Mol. Life Sci.* **2001**, *58* (10), 1451–1460.
(89) Frank, A. J.; Kopidakis, N.; Lagemaat, J. Van De. Electrons in Nanostructured TiO_2 Solar Cells: Transport, Recombination and Photovoltaic Properties. *Coord. Chem. Rev.* **2004**, *248* (13–14), 1165–1179.
(90) Daeneke, T.; Mozer, A. J.; Uemura, Y.; Makuta, S.; Fekete, M.; Tachibana, Y.; Koumura, N.; Bach, U.; Spiccia, L. Dye Regeneration Kinetics in Dye-Sensitized Solar Cells. *J. Am. Chem. Soc.* **2012**, *134* (41), 16925–16928.
(91) Zhao, D.; Rumbles, G.; Reid, O. G.; Li, Z.; Zhu, K.; Yan, Y.; Moore, D. T. Quantitative Analysis of Time-Resolved Microwave Conductivity Data. *J. Phys. D. Appl. Phys.* **2017**, *50* (49), 493002.
(92) Friedrich, D.; Valldecabres, L.; Kunst, M.; Moehl, T.; Zakeeruddin, S. M.; Grätzel, M. Dye Regeneration Dynamics by Electron Donors on Mesoscopic TiO2 Films. *J. Phys. Chem. C* **2014**, *118* (7), 3420–3425.
(93) Friedrich, D.; Kunst, M. Influence of Dye-Adsorption on Charge Carrier Kinetics in TiO 2 Colloidal Systems. *Nano Energy* **2012**, *1* (2), 303–308.
(94) Nakade, S.; Makimoto, Y.; Kubo, W.; Kitamura, T.; Wada, Y.; Yanagida, S. Roles of Electrolytes on Charge Recombination in Dye-Sensitized TiO_2 Solar Cells (2): The Case of Solar Cells Using Cobalt Complex Redox Couples. *J. Phys. Chem. B* **2005**, *109* (8), 3488–3493.
(95) Kelly, C. A.; Farzad, F.; Thompson, D. W.; Stipkala, J. M.; Meyer, G. J. Cation-Controlled Interfacial Charge Injection in Sensitized Nanocrystalline TiO_2. *Langmuir* **1999**, *15* (20), 7047–7054.
(96) Kuciauskas, D.; Freund, M. S.; Gray, H. B.; Winkler, J. R.; Lewis, N. S. Electron Transfer Dynamics in Nanocrystalline Titanium Dioxide Solar Cells Sensitized with Ruthenium or Osmium Polypyridyl Complexes. *J. Phys. Chem. B* **2001**, *105*, 392–403.
(97) Ardo, S.; Sun, Y.; Staniszewski, A.; Castellano, F. N.; Meyer, G. J. Stark Effects after Excited-State Interfacial Electron Transfer at Sensitized TiO2 Nanocrystallites. *J. Am. Chem. Soc.* **2010**, *132* (19), 6696–6709.
(98) Cappel, U. B.; Feldt, S. M.; Schöneboom, J.; Hagfeldt, A.; Boschloo, G. The Influence of Local Electric Fields on Photoinduced Absorption in Dye-Sensitized Solar Cells. *J. Am. Chem. Soc.* **2010**, *132* (26), 9096–9101.
(99) Ardo, S.; Sun, Y.; Castellano, F. N.; Meyer, G. J. Excited State Electron Transfer from Ruthenium-Polypyridyl Compounds to Anatase TiO_2 Nanocrystallites: Evidence for a Stark Effect. *J. Phys. Chem. B* **2010**, *114* (45), 14596–14604.
(100) van de Krol, R.; Goossens, A.; Meulenkamp, E. A. Electrical and Optical Properties of TiO_2 in Accumulation and of Lithium Titanate $Li_{0.5}TiO_2$. *J. Appl. Phys.* **2001**, *90* (5), 2235–2242.
(101) Gardner, J. M.; Abrahamsson, M.; Farnum, B. H.; Meyer, G. J. Visible Light Generation of Iodine Atoms and I-I Bonds: Sensitized I^- Oxidation and I_3^- Photodissociation. *J. Am. Chem. Soc.* **2009**, *131* (44), 16206–16214.
(102) Sarker, S.; Seo, H. W.; Kim, D. M. Calculating Current Density - Voltage Curves of Dye-Sensitized Solar Cells : A Straight-Forward Approach. *J. Power Sources* **2014**, *248*, 739–744.

(103) Dokić, M.; Soo, H. Sen. Artificial Photosynthesis by Light Absorption, Charge Separation, and Multielectron Catalysis. *Chem. Commun.* **2018**, *54* (50), 6554–6572.
(104) Kim, Y.; Sung, Y. E.; Xia, J. Bin; Lira-Cantu, M.; Masaki, N.; Yanagida, S. Solid-State Dye-Sensitized TiO2 Solar Cells Using Poly(3,4-Ethylenedioxythiophene) as Substitutes of Iodine/Iodide Electrolytes and Noble Metal Catalysts on FTO Counter Electrodes. *J. Photochem. Photobiol. A Chem.* **2008**, *193* (2–3), 77–80.
(105) Johansson, E. M. J.; Boschloo, G.; Hagfeldt, A.; Vlachopoulos, N.; Snedden, A.; Kloo, L.; Jarboui, A.; Chams, A.; Perruchot, C.; Jouini, M. New Approach for Preparation of Efficient Solid-State Dye-Sensitized Solar Cells by Photoelectrochemical Polymerization in Aqueous Micellar Solution. *J. Phys. Chem. Lett.* **2013**, *4*, 4026–4031.
(106) Fukuri, N.; Masaki, N.; Kitamura, T.; Wada, Y.; Yanagida, S. Electron Transport Analysis for Improvement of Solid-State Dye-Sensitized Solar Cells. *J. Phys. Chem. B* **2006**, *110*, 25251–25258.
(107) Kubo, W.; Murakoshi, K.; Kitamura, T.; Yoshida, S.; Haruki, M.; Hanabusa, K.; Shirai, H.; Wada, Y.; Yanagida, S. Quasi-Solid-State Dye-Sensitized TiO 2 Solar Cells : Effective Charge Transport in Mesoporous Space Filled with Gel Electrolytes Containing Iodide and Iodine. *J. Phys. Chem. B* **2001**, *105*, 12809–12815.
(108) Wei, W.; Wang, H.; Hu, Y. H. A Review on PEDOT-Based Counter Electrodes for Dye-Sensitized Solar Cells. *Int. J. Energy Res.* **2014**, *38*, 1099–1111.
(109) Poverenov, E.; Li, M.; Bitler, A.; Bendikov, M. Major Effect of Electropolymerization Solvent on Morphology and Electrochromic Properties of PEDOT Films. *Chem. Mater.* **2010**, *22* (13), 4019–4025.
(110) Sakai, N.; Prasad, G. K.; Ebina, Y.; Takada, K.; Sasaki, T.; March, R. V. Layer-by-Layer Assembled TiO 2 Nanoparticle / PEDOT-PSS Composite Films for Switching of Electric Conductivity in Response to Ultraviolet and Visible Light Re V Ised Manuscript Recei V Ed May 31 , 2006 The Sequential Layer-by-Layer Adsorption of Oppositel. *Chem. Mater.* **2006**, *18*, 3596–3598.
(111) Rogachev, A. Y.; Hoffmann, R. Iodine (I2) as a Janus-Faced Ligand in Organometallics. *J. Am. Chem. Soc.* **2013**, *135* (8), 3262–3275.
(112) Jude, H.; Krause Bauer, J. a.; Connick, W. B. Synthesis, Structures, and Emissive Properties of Platinum(II) Complexes with a Cyclometallating Aryldiamine Ligand. *Inorg. Chem.* **2002**, *41* (8), 2275–2281.
(113) Gao, Y.; Zhang, L.; Ding, X.; Sun, L. Artificial Photosynthesis--Functional Devices for Light Driven Water Splitting with Photoactive Anodes Based on Molecular Catalysts. *Phys. Chem. Chem. Phys.* **2014**, *16* (24), 12008–12013.
(114) Li, F.; Fan, K.; Xu, B.; Gabrielsson, E.; Daniel, Q.; Li, L.; Sun, L. Organic Dye-Sensitized Tandem Photoelectrochemical Cell for Light Driven Total Water Splitting. *J. Am. Chem. Soc.* **2015**, *137* (28), 9153–9159.
(115) Duan, L.; Xu, Y.; Tong, L.; Sun, L. CeIV- and Light-Driven Water Oxidation by [Ru(Terpy)(Pic) 3]2+ Analogues: Catalytic and Mechanistic Studies. *ChemSusChem* **2011**, *4* (2), 238–244.
(116) Li, L.; Duan, L.; Xu, Y.; Gorlov, M.; Hagfeldt, A.; Sun, L. A Photoelectrochemical Device for Visible Light Driven Water Splitting by a Molecular Ruthenium Catalyst Assembled on Dye-Sensitized Nanostructured TiO2. *Chem. Commun. (Camb).* **2010**, *46* (39), 7307–7309.

(117) Gao, Y.; Ding, X.; Liu, J.; Wang, L.; Lu, Z.; Li, L.; Sun, L. Visible Light Driven Water Splitting in a Molecular Device with Unprecedentedly High Photocurrent Density. *J. Am. Chem. Soc.* **2013**, *135* (11), 4219–4222.
(118) Zhang, L.; Gao, Y.; Ding, X.; Yu, Z.; Sun, L. High-Performance Photoelectrochemical Cells Based on a Binuclear Ruthenium Catalyst for Visible-Light-Driven Water Oxidation. *ChemSusChem* **2014**, *7* (10), 2801–2804.
(119) Badiei, Y. M.; Polyansky, D. E.; Muckerman, J. T.; Szalda, D. J.; Haberdar, R.; Zong, R.; Thummel, R. P.; Fujita, E. Water Oxidation with Mononuclear Ruthenium(II) Polypyridine Complexes Involving a Direct Ru(IV)=O Pathway in Neutral and Alkaline Media. *Inorg. Chem.* **2013**, *52*, 8845–8850.
(120) Concepcion, J. J.; Jurss, J. W.; Templeton, J. L.; Meyer, T. J. One Site Is Enough. Catalytic Water Oxidation by [Ru(Tpy)(Bpm)(OH2)]2+ and [Ru(Tpy)(Bpz)(OH2)]2+. *J. Am. Chem. Soc.* **2008**, *130* (49), 16462–16463.
(121) Concepcion, J. J.; Jurss, J. W.; Norris, M. R.; Chen, Z.; Templeton, J. L.; Meyer, T. J. Catalytic Water Oxidation by Single-Site Ruthenium Catalysts. *Inorg. Chem.* **2010**, *49* (4), 1277–1279.
(122) Kärkäs, M. D.; Åkermark, T.; Johnston, E. V.; Karim, S. R.; Laine, T. M.; Lee, B. L.; Åkermark, T.; Privalov, T.; Åkermark, B. Water Oxidation by Single-Site Ruthenium Complexes: Using Ligands as Redox and Proton Transfer Mediators. *Angew. Chemie - Int. Ed.* **2012**, *51* (46), 11589–11593.
(123) Huynh, M. H. V; Meyer, T. J. Proton-Coupled Electron Transfer. *Chem. Rev.* **2007**, *107*, 5004–5064.
(124) Purnama, I.; Salmahaminati; Abe, M.; Hada, M.; Kubo, Y.; Mulyana, J. Y. Factors Influencing the Photoelectrochemical Device Performance Sensitized by Ruthenium Polypyridyl Dyes. *Dalt. Trans.* **2019**, *48* (2), 688–695.
(125) Qi, H.; Teesdale, J. J.; Pupillo, R. C.; Rosenthal, J.; Bard, A. J. Synthesis, Electrochemistry, and Electrogenerated Chemiluminescence of Two BODIPY-Appended Bipyridine Homologues. *J. Am. Chem. Soc.* **2013**, *135* (36), 13558–13566.
(126) Groppi, J.; Bartlett, P. N.; Kilburn, J. D. Toward the Control of the Creation of Mixed Monolayers on Glassy Carbon Surfaces by Amine Oxidation. *Chem. - A Eur. J.* **2016**, *22* (3), 1030–1036.
(127) Node, M.; Kumar, K.; Nishide, K.; Ohsugi, S. I.; Miyamoto, T. Odorless Substitutes for Foul-Smelling Thiols: Syntheses and Applications. *Tetrahedron Lett.* **2001**, *42* (52), 9207–9210.
(128) Buckingham, D. A.; Dwyer, F. P.; Sargeson, A. M. Osmium(III)-Osmium(II) Electrode Potentials. The Effects of Charge, Conjugation, Coordinated Halide, and Substitution in the Ligand. *Inorg. Chem.* **1966**, *5* (7), 1243–1249.
(129) Buckingham, D. A. Preparations and Oxidation-Reduction Potentials of Some Osmium Complexes, Australian National University, 1961.